ACS MATERIALS Au
AN OPEN ACCESS JOURNAL OF THE AMERICAN CHEMICAL SOCIETY

pubs.acs.org/materialsau

Review

Transition Metal Chalcogenides as a Versatile and Tunable Platform for Catalytic CO_2 and N_2 Electroreduction

Giorgio Giuffredi, Tristan Asset, Yuanchao Liu, Plamen Atanassov, and Fabio Di Fonzo*

Cite This: *ACS Mater. Au* 2021, 1, 6–36

Read Online

ACCESS | Metrics & More | Article Recommendations

ABSTRACT: Group VI transition metal chalcogenides are the subject of increasing research interest for various electrochemical applications such as low-temperature water electrolysis, batteries, and supercapacitors due to their high activity, chemical stability, and the strong correlation between structure and electrochemical properties. Particularly appealing is their utilization as electrocatalysts for the synthesis of energy vectors and value-added chemicals such as C-based chemicals from the CO_2 reduction reaction (CO_2R) or ammonia from the nitrogen fixation reaction (NRR). This review discusses the role of structural and electronic properties of transition metal chalcogenides in enhancing selectivity and activity toward these two key reduction reactions. First, we discuss the morphological and electronic structure of these compounds, outlining design strategies to control and fine-tune them. Then, we discuss the role of the active sites and the strategies developed to enhance the activity of transition metal chalcogenide-based catalysts in the framework of CO_2R and NRR against the parasitic hydrogen evolution reaction (HER); leveraging on the design rules applied for HER applications, we discuss their future perspective for the applications in CO_2R and NRR. For these two reactions, we comprehensively review recent progress in unveiling reaction mechanisms at different sites and the most effective strategies for fabricating catalysts that, by exploiting the structural and electronic peculiarities of transition metal chalcogenides, can outperform many metallic compounds. Transition metal chalcogenides outperform state-of-the-art catalysts for CO_2 to CO reduction in ionic liquids due to the favorable CO_2 adsorption on the metal edge sites, whereas the basal sites, due to their conformation, represent an appealing design space for reduction of CO_2 to complex carbon products. For the NRR instead, the resemblance of transition metal chalcogenides to the active centers of nitrogenase enzymes represents a powerful nature-mimicking approach for the design of catalysts with enhanced performance, although strategies to hinder the HER must be integrated in the catalytic architecture.

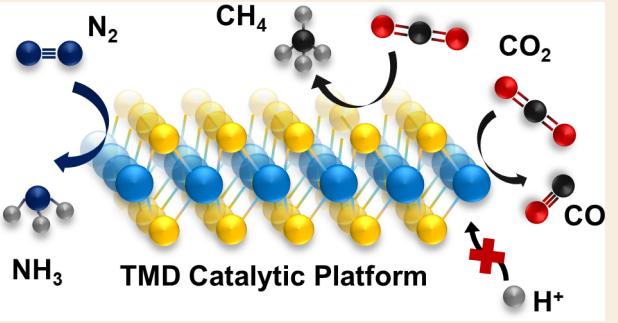

1. INTRODUCTION

The awareness and necessity of utilizing carbon-neutral fuels and energy vectors (i.e., chemicals that allow the transfer and storage of electrical energy), fostered by environmental, economic, and political motivations,[1,2] has increased in recent years the industrial importance of electrocatalysis for the synthesis of value-added chemicals and the research interest in this topic. Indeed, synthesis of energy vectors through electrochemical technologies represents an appealing and cost-effective method to convert the nonprogrammable and intermittent electrical energy generated by renewable sources into the chemical energy of fuels and chemicals (the energy vectors) to be utilized in another moment, allowing for an efficient long-term energy storage mechanism[3] or the utilization of carbon-neutral fuels and chemical feedstock. Along the lines of clean generation of hydrogen from water electrolysis through the hydrogen evolution reaction (HER), the more renowned electrochemical reaction in this framework,[4] extensive studies are being carried out on the electrochemical reduction of carbon dioxide (CO_2R) and the electrochemical fixation of nitrogen to produce ammonia (NRR). The former reaction allows the production of various HC-based chemicals to be employed as synfuels (e.g., CO, CH_4)[5,6] or as commodity for the chemical industry (e.g., HCOOH, C_2H_4),[7,8] whereas the latter is envisioned as an alternative to the industrial, energy-intensive Haber-Bosch process.[9] The three reduction reactions occur on the surface of appropriate catalysts in an electrolytic device, with the electrochemical circuit being typically closed by the oxygen evolution reaction (OER), taking place at the anodic catalyst.

Even if these three electrochemical processes are characterized by different TRLs (technology readiness levels),

Received: March 24, 2021
Published: May 24, 2021

https://doi.org/10.1021/acsmaterialsau.1c00006
ACS Mater. Au 2021, 1, 6–36

meaning that different scientific and technological objectives are being pursued for these technologies, still a common research thread can be found in the cathodic electrocatalyst. The current state-of-the-art catalyst for the HER, employed also in commercial polymer electrolyte membrane (PEM)-based electrolyzers, is platinum, due to its remarkable electrocatalytic activity and good stability.[10] However, its high cost and scarcity limit its widespread application. Consequently, efforts are devoted to substituting it with an alternative nonprecious, earth-abundant catalyst that still exhibits a comparable catalytic activity.[11] Different classes of materials have proven to be efficient HER electrocatalysts: compounds of transition metals from the first row, e.g., Ni-, Co-, and Fe-based catalysts, have been extensively studied.[12,13] Transition metal nitrides and carbides,[14−17] phosphides,[18] and chalcogenides[19,20] have demonstrated outstanding HER activity in a variety of conditions; additionally carbon-based compounds, through doping the C backbone of the catalyst with different heteroatoms showed their remarkable catalytic efficiency for the HER.[21,22] In the field of CO_2R, the main concern is finding an electrocatalyst that meets the criteria of high activity and product yield at low applied overpotential, maximum selectivity toward value-added C products, negligible parasitic reactions, and long-term stability under continuous operation.[8,23] In the past years, copper-based electrocatalysts have emerged as the most promising candidates for CO_2R in commercial devices due to their ability to reduce CO_2 to a variety of hydrocarbons with good efficiency, producing a mix of products according to the applied potential and the local chemical environment (e.g., local pH, employed electrolyte), although they still suffer from low selectivity for a given carbon-based product.[24−26] Lastly, regarding the electrochemical fixation of nitrogen into ammonia, basic challenges regarding the activity and selectivity of catalysts are being addressed, due to the early development stages of the technology.[9] By mimicking the metallic active sites of nitrogenase enzymes (which catalyze N_2 fixation in living beings), transition metals such as Fe, W, Mo, or Ru have been proposed to efficiently catalyze the electrochemical NRR,[27,28] although experimental works are limited in number and the best-performing catalysts are still characterized by low selectivity that hinders any practical applicability as of today.[29]

Among the many nonprecious families of materials that are being studied, group VI transition metal chalcogenides, i.e., based on Mo and W, are particularly attractive because of their low cost, high abundance,[30] and good electrochemical stability.[31] Additionally, their nanoscale structure in terms of morphology, composition, and electronic structure can be easily fine-tuned and tailored to the catalytic application of interest, making them a flexible class of materials for the design of electrocatalysts. Crystalline group VI transition metal dichalcogenides (c-TMDs) are historically renowned as efficient HER electrocatalysts, as it has been shown that their active sites, the metal atoms on the edges of the material, have an optimal binding energy for hydrogen, very close to the value of Pt.[32,33] This remarkable characteristic motivated extensive research on every aspect of these material, with innumerable works studying their electronic structure, their synthesis techniques, and their catalytic performance for HER and water splitting, as visualized in Figure 1. The vast literature on this application has been critically analyzed in several reviews, some of the most recent of which are here reported as a reference to the reader.[34−37] In addition to their well-known

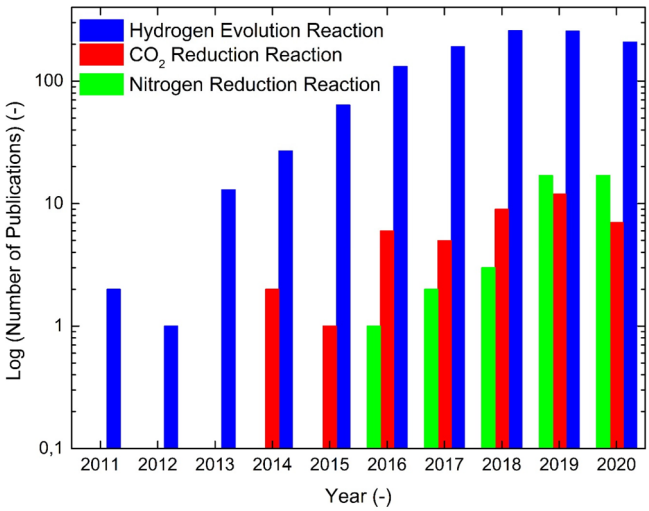

Figure 1. Number of indexed publications on Web of Science on transition metal chalcogenide-based systems as electrocatalysts for different reduction reactions, namely, hydrogen evolution reaction (HER), CO_2 reduction reaction (CO_2R), and nitrogen reduction reaction (NRR), per year. The number of publications on HER outweighs by 1 order of magnitude that of CO_2R and NRR, with an approximate 200 publications per year from 2016 for the first application against ≈30 for the other two reactions combined.

activity toward the HER, this class of materials can also catalyze CO_2R with high efficiency, overcoming the scaling relations between reaction intermediates that limit the activity and selectivity of transition metal catalysts.[38] Indeed, it was shown that the energy profile of the CO_2R intermediates is more favorable on the edge sites of c-TMDs than on transition metals.[38−40] Additionally, the same edge atoms can catalyze the NRR, due to their chemical similarity to the Mo-containing active sites of the nitrogenase enzyme.[41] Consequently, the application of c-TMDs for these reactions has been subject of increasing research interest in recent years (Figure 1). Despite their high intrinsic activity for CO_2R and NRR, the flexible nature of the active sites at the edges and the predominance of the HER over the other reactions in aqueous electrolytes represent a major hurdle in the efficient implementation of group VI transition metal chalcogenide electrocatalysts for these applications. Indeed, the design of CO_2R and NRR catalytic systems that can efficiently suppress the HER is becoming a topic of the utmost importance in the framework of a widespread diffusion of these electrocatalytic technologies, as highlighted by a recent work on catalytic systems for nitrogen reduction.[42]

Considering the high activity of group VI transition metal chalcogenides for the three previously mentioned reactions, it is important to understand how the physical/chemical characteristics of their active site affect the macroscale efficiency of the resulting material, with the aim of tailoring the catalytic architecture to the specific reaction of interest (CO_2R or NRR) and hindering the competing HER as much as possible. In this review, we take inspiration from HER, the application for which both the intrinsic per-site activity and the overall efficiency of group VI transition metal chalcogenides have been optimized through precise synthesis techniques and propose the systematic implementation of this family of compounds as efficient electrocatalysts for CO_2R and NRR. Ranging from the nanoscale level to the mesoscale architecture

https://doi.org/10.1021/acsmaterialsau.1c00006
ACS Mater. Au 2021, 1, 6−36

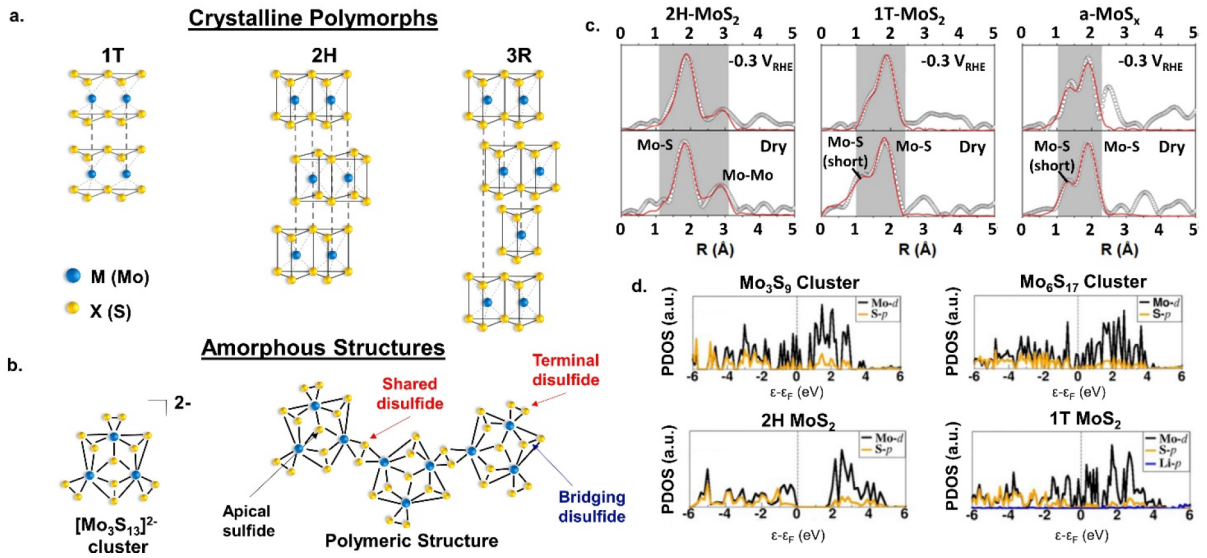

Figure 2. (a) Structural organization of the different crystalline group VI TMDs polymorphs, employing molybdenum sulfide as representative of the family of compounds. According to the metal coordination, different stacking sequences can be obtained. Adapted from ref 44. Copyright 2015 American Chemical Society. (b) $[Mo_3S_{13}]^{2-}$ cluster building block of amorphous molybdenum sulfide, along with the polymeric structure of the material that is obtained when the clusters are connected by sharing their disulfide ligands, according to the scheme proposed by ref 76. (c) In-operando Mo K-edge Fourier transform EXAFS for 2H-MoS_2, 1T-MoS_2, and a-MoS_x during H_2 turnover. Both 1T polymorph and a-MoS_x exhibit a Mo−S ligand (highlighted in the gray area) that is absent in 2H-MoS_2. (d) Partial density of states for 2H-MoS_2, 1T-MoS_2, and two different MoS-based clusters utilized as representative of the $[Mo_3S_{13}]^{2-}$ building blocks of a-MoS_x. Panels (c) and (d) are adapted with permission from ref 82. Copyright 2019 The Authors. Published by Wiley-VCH Verlag GmbH & Co. KGaA.

characteristic length, we discuss the molecular organization and electronic structure of both the crystalline and amorphous form, along with their relationship with the per-site catalytic activity. Then, we thoroughly review the available literature for these two applications to outline the strategies that should be exploited to synthesize transition metal chalcogenide-based catalysts with enhanced electrocatalytic efficiency for the application of interest.

2. STRUCTURE OF GROUP VI TRANSITION METAL CHALCOGENIDES

2.1. Crystalline Transition Metal Dichalcogenides: Structural and Electronic Properties

Crystalline transition metal dichalcogenides (c-TMDs) are characterized by the chemical composition MX_2, where M is the transition metal (Mo, W for group VI transition metal chalcogenides) and X is the chalcogen (e.g., S, Se, Te), and exhibit a layered structure similar to that of graphite, with each single layer composed of stacked X−M−X sheets and the sequential stacking of layers forming the material. Interlayer bonding occurs through weak van der Waals forces, whereas the metal−chalcogen bond is covalent in nature where the metal contributes to the bonding states with four electrons, resulting in an oxidation state of +4 for the metal and −2 for the chalcogen. According to the nature of the metal and chalcogen atoms, the stacking of the various X−M−X layers and the metal coordination in each layer may vary, giving rise to different polymorphs. A more detailed discussion on the polymorphism in transition metal chalcogenides can be found in other works[31,43,44] and is summarized in Figure 2a. Briefly, the three most common polymorphs are the 1T, 2H, and 3R. In this notation, the digit identifies the number of X−M−X layers in the crystalline unit cell, and the letter denotes the symmetry of the material: T refers to a tetragonal symmetry, H to hexagonal symmetry, and R for rhombohedral symmetry. The stacking sequence of the layers along the axis perpendicular to the planes is denoted by a sequence of three letters, each identifying the relative position between metal and chalcogen atoms. Therefore, the atoms in the 1T polymorph are stacked with an AbC sequence, with an AbA BaB sequence in the 2H organization, and finally with the AbA CaC BcB sequence in the 3R polymorph. The nature of the metallic atom defines the thermodynamically stable phase of the material and its electronic nature. For group VI transition metal chalcogenides, the stable polymorph is the 2H, and the material is semiconducting in nature, as the d-orbitals of the metal are fully occupied;[31] nonetheless, transition metal chalcogenides with transition metals from other groups exhibit different stable polymorphs and electronic character; e.g., group IV and group V transition metal chalcogenides are metallic in nature. Even if the thermodynamically stable polymorph in group VI transition metal chalcogenides is the 2H one, according to the formation history[45] or synthesis route,[46−48] different phases can coexist in the same compound and the 2H → 1T transition can drastically alter the electronic structure of the material and, consequently, its electrocatalytic properties. The 2H → 1T transition is usually triggered through methods based on the intercalation of alkali metal compounds, where the most employed is *n*-butyllithium. The formation of the 1T phase occurs through a destabilization of the semiconducting 2H phase, caused by an increase in d-orbital electron density in the transition metal upon an electron transfer from the intercalated compound. Differently from the metal atom, the chalcogen has a small effect on the structure, but it influences the band gap of the material: an increase in chalcogen atomic number diminishes the band gap of the material, e.g., ranging from 2H-MoS_2 to 2H-$MoSe_2$ and 2H-$MoTe_2$, and the band gap decreases from 1.3 to 1.0 eV.[45]

https://doi.org/10.1021/acsmaterialsau.1c00006
ACS Mater. Au 2021, 1, 6−36

Early works on c-TMDs showed how the anisotropic structure of the material translates into an anisotropy in the electrical properties of the basal and edge planes with an in-plane electrical conductivity that is roughly 2000 times higher than the out-of-plane conductivity.[49] In the case of bulk MoS_2, a marked difference is registered in electron mobility according to the chosen orientation: the out-of-plane to in-plane mobility ratio is roughly 10^{-3}, caused by the interlayer van der Waals gaps that act as tunneling barriers.[50] As reported in a number of previous works,[51−53] carrier transport and scattering are in-plane confined, and the scattering occurs mainly through mechanisms that are usually seen in semiconductors and other 2D materials such as graphene, e.g., phonon scattering or roughness scattering.[51] This anisotropy in electrical properties affects also the electrocatalytic properties of c-TMDs: for example, the sluggish out-of-plane electron mobility in crystalline MoS_2 (c-MoS_2) negatively influences its HER performance as, by increasing the number of layers in the catalyst, the exchange current density decreases 4.47 times per layer due to the inefficient electron hopping between adjacent layers.[54] Additionally, the morphological anisotropy determines different electronic structures for the basal and edge planes. Previous theoretical works[55] calculated the p-projected densities of states (p-DOS) of the basal chalcogen atoms for different c-TMDs in a single-layer configuration, showing that, for group VI transition metal chalcogenides, the nature of the basal plane depends on the considered polymorph: the basal planes of the 2H phase are semiconducting with a band gap, while in the case of 1T polymorph, the basal planes exhibit a metallic character. On the other hand, the edge planes for both polymorphs have metallic character, with an effect that is more evident when the material is reduced to nanometer size and exfoliated to few layers. In this case, the missing coordination at the metal edges caused by the small size of the material generates metallic edge states where an adsorbate (e.g., H_{ads}) can easily coordinate to, influencing the final catalytic activity of the material because the metallic edge atoms can act as catalytically active sites for specific reactions.[31] Considering that the metallic edge states in c-TMDs consist of transition metals (Mo, W), the adsorption energy of reactants that can correlate to these sites is related to the density of the metal d states at the Fermi level: the magnitude of the adsorption energy is dependent on the difference between the Fermi level energy and the d-band center energy of the metal site.[56,57] This dependency opens up the possibility to modify the electronic structure of these sites (e.g., through doping or nanosizing effects) to tune and optimize the interaction energy with the reaction substrate.[35,58] In fact, according to the Sabatier principle, optimizing the interaction energy between the active site and the reaction substrate is the most efficient way to enhance the activity of a catalyst.[59] As a consequence, the presence of the metallic edge states in nanosized c-TMDs confers them peculiar properties, absent in their bulk counterparts, that affect not only their catalytic activity but also their optical and electrical characteristics: the changes in electronic structure prompted by the nanosizing and the few-layering of c-TMDs also affect their band gap, an effect that is particularly pronounced for group VI 2H c-TMDs. When the layer number is small enough, the interlayer orbital interaction changes with respect from the bulk multilayered material, widening the band gap and transitioning it from indirect to direct.[60,61] Due to this peculiarity, few-layered c-TMDs have found a number of applications in the optoelectronic field with remarkable results.[62,63]

2.2. Amorphous Transition Metal Chalcogenides: Structural and Electronic Properties

Amorphous transition metal chalcogenides (a-TMCs) attracted particular attention for electrocatalytic applications in recent years, with emphasis placed on amorphous molybdenum sulfide (a-MoS_x) as hydrogen evolution catalyst as it showed a catalytic activity for the reaction higher than that of its crystalline counterpart.[64] Despite the increasing interest in a-MoS_x, reports on the other a-TMCs, i.e., a-$MoSe_x$, a-WSe_x, and a-WS_x, are far more limited: the electrical and catalytic characteristics of these three compounds are usually inferred by analogy with amorphous molybdenum sulfide, due to the similar metal/chalcogen molar ratio and the similar Raman fingerprint that suggests the same coordination structure between metal and chalcogen.[65−68] Amorphous molybdenum sulfides, discussed here as a representative of the whole a-TMC family, can be considered a class of a-MoS_x compounds with different sulfur stoichiometry, with x ranging from 2[69,70] to 6[71] according to the synthesis route, that lacks a long-range order but exhibits a short-range organization depending on the Mo/S atomic ratio. Different models have been proposed to resolve the structure of amorphous molybdenum sulfides; e.g., for a-$MoS_{4.7}$, a linear model has been proposed based on Mo_3S_{14} building blocks, connected through bridging (S−S) bonds.[72] Similar chain models, based on the repetition of building blocks with different stoichiometry, have been suggested for amorphous WS_5 and WSe_5, based on EXAFS (extended X-ray absorption fine structure) studies,[73] and for amorphous MoS_5. For the latter case, the suggested building blocks have $[Mo_2S_8]^{2+}$ stoichiometry and are connected through bridging S_2^{2} ligands, forming linear structures that can arrange in globular morphologies.[74]

In addition to these polychalcogenide compounds, a-MoS_x (with x ranging from 3 to 4) has been extensively researched in recent years, due to its high HER activity and its facile synthesis route by electrochemical or mild wet-chemical techniques, and thus will be the focus of a more detailed discussion.

The as-fabricated, pristine a-MoS_x material is characterized by a Mo/S ratio ranging from 1/2[75] to ≈1/4,[76] with a marked dependency on the synthesis procedure. As shown by Artero and collaborators,[76] the pristine a-MoS_x exhibits a molecular-based polymeric structure, based on $[Mo_3S_{13}]^{2-}$ building units arranged in 1D or 2D networks through shared disulfide ligands, as depicted in Figure 2b. Additionally, the disordered structure of the material is characterized by the presence of defective Mo^{V}=O sites. Notably, the a-MoS_x building blocks have similar XPS signature, Raman signature, and Mo−Mo bond length to crystalline thiomolybdate $[Mo_3S_{13}]^{2-}$ nanoclusters.[77] This pristine a-MoS_x is, however, a precatalytic phase of the actual noncrystalline catalyst which is formed in situ through the interaction of the pristine material with the electrolyte[70,78] upon applied potential in a so-called electrochemical "activation" process. The dynamics of this process are still investigated, as the full extent of the modifications depends on many experimental parameters like electrolyte pH, applied potential cycling during activation, and catalytic preparation method, and the reader is referred to other more detailed analyses of this process[64,69,79] while here an overview is presented.

https://doi.org/10.1021/acsmaterialsau.1c00006
ACS Mater. Au 2021, 1, 6−36

The main structural and chemical modifications affecting the precatalytic phase are a cleaving of excess sulfur from the surface, through interaction of the material with protons from the electrolyte at cathodic potential,[80] and a subsequent structural reorganization affecting the Mo atoms, with the proposed formation of molybdenum oxide species, whose precise stoichiometry depends on the pH of the surrounding electrolyte. When this process occurs in acidic electrolyte (usually a 0.5 M H_2SO_4 aqueous solution), the actual catalyst presents the same stoichiometry of c-MoS_2 but has different structure, metal coordination environment,[75] and active site distribution.[78] By analogy with a-MoS_x, the same activation process has been observed and studied for a-$MoSe_x$.[67]

The higher catalytic activity than c-MoS_2[81] and the different Mo−S coordination of a-MoS_x arise from a different electronic structure between the two phases, as shown by a combined experimental/theoretical work by Hofmann and co-workers.[82] The amorphous phase shared similarities with the 1T polymorph in terms of electronic structure and Mo−Mo and Mo−S bond lengths, as revealed by in operando EXAFS analysis (Figure 2c). Indeed, the p-DOS of the Mo atoms in Mo_3S_9 or Mo_6S_{17} clusters (employed as model monomers for a-MoS_x) showed a metallic character due to the Fermi level crossing their 3d-orbitals, as shown in Figure 2d, similarly to the Mo atoms in 1T c-MoS_2. Additionally, the density functional theory (DFT)-calculated adsorption energy for the H_{ads} HER intermediate on a-MoS_x was closer to the thermoneutral value than 2H c-MoS_2, providing a ground for the higher activity of amorphous molybdenum sulfide when compared to the semiconducting 2H polymorph. Despite the intense research activity on a-MoS_x, the amorphous nature and nondefined atomic arrangement of amorphous group VI transition metal chalcogenides, along with the radical changes they are subjected during electrocatalytic activity, still represent a practical drawback that limits the number of reports focused on the electronic structure of this class of materials.

3. GROUP VI TRANSITION METAL CHALCOGENIDE-BASED CATALYSTS: BALANCING ACTIVITY AND SELECTIVITY

Transition metal chalcogenides have found their main application as HER electrocatalysts, due to the optimal energy profile for H_2 evolution on their edge sites, to the structure-dependent electronic and electrochemical properties, and to the possibility of obtaining a wide variety of materials by coupling chalcogen atoms with transition metal from different groups. Consequently, extensive study was focused on the HER application of various transition metal chalcogenide families and on the engineering and fine-tuning of their structural and electronic characteristics for this reaction. Along with group VI (Mo and W) transition metal chalcogenides,[34−37] group IV (Ti, Zr, Hf),[83,84] group V (V, Nb, Ta),[85−87] and group VII (e.g., Re) transition metal chalcogenides[88] showed remarkable HER activity. Group V transition metal chalcogenides exhibited improved catalytic activity and fast reaction kinetics, due to the metallic conductivity of their stable polymorphs, to the presence of active sites in the basal plane and to the low energy of their lowest unoccupied state which favors hydrogen adsorption.[89] Zhang and collaborators[90] synthesized metallic TaS_2 thin films which performed the HER at an optimal rate, with a 33 mV dec^{-1} Tafel slope (very similar to Pt) and an η_{10} value (the overpotential required to reach a geometric current density of -10 mA cm^{-2}) of 65 mV, whereas Yuan et al.[91] fabricated metallic VS_2 single crystal nanosheets which efficiently catalyzed the HER with fast reaction kinetics (Tafel slope of 36 mV dec^{-1}) and small overpotentials (68 mV at -10 mA cm^{-2}). Najafi et al.[87] further demonstrated the high per-site activity of group V transition metal chalcogenides by fabricating a single-walled carbon-nanotube-supported TaS_2/$TaSe_2$ hybrid catalyst which achieved a -10 mA cm^{-2} overpotential as small as 120 mV in acidic media and 230 mV in alkaline environment, due to the optimal ΔG_H value arising from the hybridized structure. Due to their impressive performance, transition metal chalcogenide-based catalysts have been considered as alternative HER catalysts to the state-of-the-art Pt in PEM electrolyzers.[92−94] In the framework of their large-scale, commercial implementation, however, adopting standardized and widely accepted experimental protocols and benchmarking tests to evaluate the HER catalytic activity becomes paramount. In addition to various performance descriptors and experimental evaluations for HER catalysts in solar-driven water splitting devices,[95] where current densities are much smaller than those of PEM electrolyzers, the reader is referred to more recent works that outlined a series of activity descriptors for high-current density application assessment, as overpotential at fixed current densities, Tafel slope, turnover frequency, and Faradaic efficiency,[96] and pointed out the importance of rigorous experimental setup and a series of benchmark tests for alternative catalysts against Pt in a half-cell environment.[97]

In this section, focusing on group VI transition metal chalcogenides, we outline the most widespread design techniques for these materials which, by modifying the structural and electronic properties at different length scales (from the nano- to the mesoscale), aim at optimizing their HER catalytic performance. As discussed in a recent review,[96] these techniques are aimed at increasing the number of active sites or at enhancing the intrinsic per-site activity. Usually employed strategies consist of creating new surface active sites by nanoscale engineering or by introducing defective sites in different regions of the catalyst, doping the catalyst with metallic or nonmetallic heteroatoms to promote the per-site activity by altering the electronic structure of the sites, synthesizing the metallic polymorph to improve the reaction kinetics and the electron transfer, or assembling heterostructures to fine-tune the elementary steps of the HER, to enhance the electron transfer rate, or to increase the exposure of active sites.

Group VI transition metal chalcogenides can coordinate different adsorbates on their active sites: consequently, they are highly active not only for HER but also for CO_2R and NRR, as it will be detailed in the next sections. Therefore, the techniques that are here discussed play a two-fold role in determining the overall catalytic efficiency for the desired application. On the one hand, if interaction with hydrogen is not hindered, it will lead to a remarkable HER activity at the expense of CO_2R and NRR, due to the more favorable adsorption energy of hydrogen and the easier kinetics of hydrogen evolution. On the other hand, if the HER is effectively suppressed and the adsorption of protons hindered, the same techniques can facilitate the adsorption of CO_2 and N_2 (for CO_2R and NRR applications, respectively) and improve the catalytic efficiency of their reduction.

https://doi.org/10.1021/acsmaterialsau.1c00006
ACS Mater. Au 2021, 1, 6−36

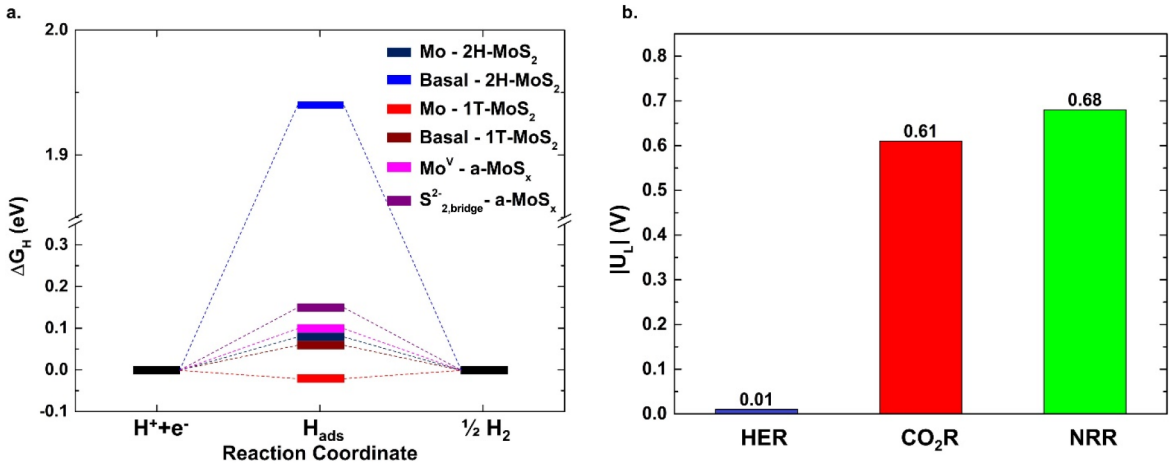

Figure 3. (a) Overview of the Gibbs free energy variation for the HER (ΔG_H) for the different active sites of crystalline and amorphous polymorphs of group VI TMDs, represented by molybdenum sulfide. The values for 2H-MoS_2 have been calculated by refs 55 and 98 and the ones for 1T-MoS_2 by ref 260. The value for the Mo^V sites in a-MoS_x have been calculated by ref 76 and that for the bridging disulfide ligands sites by ref 103. (b) Limiting potential U_L magnitude comparison for the three reduction reactions at the Mo-edge sites in crystalline 2H-MoS_2: HER, CO_2 to CO reduction (CO_2R), and NRR. The limiting potential is defined as the applied potential at which all the reaction steps become exergonic. While the Mo-edge sites can catalyze with good U_L the three reactions, the interaction with protons is more energetically favorable for HER than for the other two reductions: consequently, the HER occurs more easily at the edge sites. The U_L values for HER and CO_2R are calculated by ref 38 and the one for NRR by ref 239.

3.1. Intrinsic Activity of Group VI Transition Metal Chalcogenides

First evidence of HER activity of c-TMDs was shown by Hinnemann et al.,[32] whose DFT calculations showed that the ΔG_H (that is, the Gibbs free energy variation for the reaction) on the Mo-edge sites of c-MoS_2 is close to the optimal thermoneutral value, suggesting the high HER activity of the material. In general, the edges of all c-TMDs exhibit good activity and comparable electronic structure, since for all the edge sites the calculated ΔG_H values are close to the thermoneutral value, although the specific activity of each edge site depends on the specific material considered.[55] Based on the ΔG_H values at the edge sites, the most active catalyst was determined to be c-$MoSe_2$, followed by c-WS_2, c-MoS_2, and c-WSe_2.[98] The high predicted activity of the c-MoS_2 Mo-edges was confirmed experimentally by Jaramillo et al.,[99] who correlated the number of active edge sites to the HER rate. More recently, Mitterreiter et al.[100] exploited the same approach to experimentally correlate the activity of c-$MoSe_2$ to the density of edge sites. As for the basal planes, DFT studies on group VI c-TMDs[55,98] showed that the basal planes of c-MoS_2, c-$MoSe_2$, c-WSe_2, and c-WS_2 have poor catalytic activity. Basal planes of 2H polymorphs are inert since adsorption of protons is hindered due to the high ΔG_H (~2 eV) irrespective of the compound. On the other hand, the poor activity of 1T basal planes arises from the instability of the adsorbed proton on the chalcogen basal atom. An overview of the calculated ΔG_H values for the different HER sites of c-MoS_2, reported as representative of the whole group VI transition metal chalcogenides, is shown in Figure 3a. Despite being inactive for the HER in its pristine form, the basal planes can be activated through the introduction of chalcogen vacancies, mechanical strains, or through substitutional doping: these methods modify the electronic structure of the basal plane by introducing new gap states near the Fermi level that allow for a facile adsorption of the reactant at the newly formed active sites.

a-TMCs also exhibit remarkable per-site HER activity. However, the nature of their active sites is still debated because of the complex chemical and structural modifications that these materials undergo during the activation process. While many works have studied the HER active sites in a-MoS_x, for which the calculated ΔG_H is very similar to that of the crystalline counterpart (Figure 3a), almost no reports are found for the other a-TMCs, for which the active site distribution is inferred by analogy with a-MoS_x. For a-MoS_x, two active site models have been proposed. The first one, proposed by Artero and collaborators[76] suggested that the HER active sites derive from Mo^{IV} atoms, formed upon the electrochemical activation. The process, performed in a pH 7 phosphate buffer electrolyte, reduced the bridging S_2^{2-} ligands and eliminated the terminal S_2^{2-} groups, transforming the $[Mo_3S_{13}]^{2-}$ clusters of the pristine material into $[Mo_3]$ defective units characterized by Mo^{IV} sites. In turnover conditions, the Mo^{IV} sites undergo a proton-coupled electron transfer forming the active site, where hydrogen is produced in a homolytic way or by protonation, yielding in the latter case Mo^V=O species, which was registered by Raman spectroscopy. The thermodynamic feasibility of this reaction mechanism was supported by DFT analysis, with a calculated ΔG_H through the formation of the Mo^V=O compound of 0.108 eV, close to the value of c-MoS_2 Mo-edge sites. The second model instead proposed the sulfur groups as HER active sites, although the nature of the active sulfur ligands is still debated. Lassalle-Kaiser et al.,[101] by in situ XANES (X-ray absorption near-edge structure) and EXAFS analysis of the activation and HER mechanism of an a-MoS_x catalyst in pH 2 electrolyte, proposed as active sulfur groups the terminal S_2^{2-} from $Mo^{III}(S_2)$ units, formed at the catalyst/electrolyte interface through reduction of Mo centers and oxidation of S ligands. Yeo's group showed in situ Raman spectroscopic evidence of H binding on sulfur atoms in a-MoS_x prepared by different electrodeposition routes and operating in strongly acidic electrolyte[102] and showed a strong correlation between per-site turnover frequency (TOF) and percentage of apical/bridging S_2^{2-} ligands.[103] Experimental data ruled out

https://doi.org/10.1021/acsmaterialsau.1c00006
ACS Mater. Au 2021, 1, 6−36

the involvement of Mo^{IV} sites in the reaction, as no Mo−H Raman vibrational bands were registered and no TOF/Mo^{IV} relationship was found, while DFT calculations allowed one to identify bridging S_2^{2-} groups as HER active. Indeed, while terminal disulfide ligands bind H too strongly undergoing a passivation and apical disulfide groups bind H too weakly, being thus inactive, the calculated ΔG_H is close to 0 eV on the bridging S_2^{2-} ligands, which are consequently the active sites. A recent work by Escalera-López et al.[79] reported, through a comprehensive electrochemical study, the dependency of the HER active sites of a-MoS_x on the electrolyte pH. According to the operating conditions, three different active sites are formed during the electrochemical activation: in acidic media (pH <4), the activation cleaves the bridging disulfide ligands, generating unsaturated S^{2-} sites which are the predominant HER active sites. In mildly acidic to neutral pH (4 < pH < 7), instead, the cleaving of the bridging disulfide ligands fosters the creation of unsaturated Mo^{V+} species, which would undergo dissolution in acidic pH, forming in the neutral electrolyte $Mo^{V+}O_xS_y$ HER active species. In alkaline media, finally, both species are unstable and molybdenum oxide phases are formed, with sluggish HER kinetics and reduced stability.

3.2. Multiscale Design Strategies for Group VI Transition Metal Chalcogenide-Based Catalysts

Starting from the high per-site activity, different techniques have been developed to engineer group VI transition metal chalcogenides at different length scales to either improve the intrinsic activity or to increase the total number of active sites of the material. The historically predominant interest in HER applications was the major driver in the development of these techniques, whose main goal was optimizing the interaction between active site and HER intermediates. Nevertheless, the active sites in group VI transition metal chalcogenides exhibit an optimal energy profile not only for HER but also for CO_2R and NRR. Considering this flexibility of the active sites, which can coordinate the three different adsorbates (i.e., H* for HER, CO_2* for CO_2R, N_2* for NRR), these same techniques can be exploited for the design of efficient group VI transition metal chalcogenide catalysts for CO_2R or NRR, as will be discussed in the following sections. Nevertheless, the energetically easier interaction with protons over CO_2 and N_2 in protic environments, represented in Figure 3b, represents a major hurdle to be addressed for CO_2R and NRR applications to avoid the predominance of the parasitic HER and a low selectivity toward the desired reactions.

3.2.1. Synthesis of the Metallic Polymorph. As introduced in section 2, the synthesis of metallic 1T c-TMDs is related to a radically different electronic structure with respect to the 2H polymorph because the crystalline organization changes radically with the phase transition. The metal−metal bond distance and the coordination number for the metallic site change and the crystalline cells undergo a structural distortion, resulting in a higher d-orbital electron density for the metal atoms and a consequent change in electronic structure of the active sites.[104,105] Since the 1T polymorph is metastable and slowly tends to revert to the 2H phase, the long-term stability of the material is a key issue, and techniques have been developed to avoid this phase reversion.[106] Synthesis strategies to obtain high-purity 1T c-TMDs and their application and performance for HER have been thoroughly detailed in previous review works, to which the reader may refer.[105,107,108] More recently, Luo et al.[109] fabricated a 1T c-MoS_2 HER catalyst through an interfacial redox technique involving Pd incorporation: the metallic catalyst exhibited improved hydrogen adsorption, activation of the basal plane, and an improved conductivity, leading to an η_{10} of 78 mV, along with an impressive stability. Zhang and collaborators developed a general and facile method for the synthesis of high-purity 1T c-TMDs with impressive HER performance (approximately −600 mA cm^{-2} at −0.4 V_{RHE} for 1T c-MoS_2 nanocrystals).[110] The method can be extended to any other c-TMD structures, as demonstrated by the fabrication of 1T c-MoSeS nanodots with η_{10} of 140 mV, Tafel slope of 40 mV dec^{-1}, and excellent durability due to the higher conductivity and improved ΔG_H.[111] Interestingly, while the metallic electronic character can be directly correlated to an HER performance enhancement, this relation is not straightforward for the other reductions, where it actually can further steer the selectivity away from the desired reaction toward the competing HER. Indeed, CO_2R and NRR are characterized by more complex multistep mechanisms where the rate-determining step may not be related to electron transfer but to an adsorption or desorption process. MacFarlane and collaborators[41] observed a decreased NRR efficiency for a Ru/1T c-MoS_2 catalyst with respect to Ru/2H c-MoS_2 because, when the TMD was transitioned to the metallic polymorph, the position of its conduction band shifted below the H^+/H_2 redox potential, allowing for HER to occur, whereas the different conduction band of the 2H polymorphs inhibited the parasitic HER. In the framework of the competition between CO_2R and HER, the improved electron conductivity of the metallic polymorph further improves the fast kinetics of the latter and represents an additional drawback for reducing CO_2, as it can shift the selectivity of the catalyst toward the HER.

3.2.2. Chevrel Phase Transition Metal Chalcogenides. The synthesis of Chevrel phase (CP) transition metal chalcogenides materials represents an appealing and powerful strategy to fine-tune the electronic structure and catalytic properties of these materials. CP transition metal chalcogenides are characterized by the $M_yMo_6X_8$ stoichiometry (X is the chalcogen atom, and M is a metal, e.g., Fe, Ni, Cu, etc., with y ranging from 0 to 4) and by a three-dimensional structure formed by different Mo_6X_8 clusters connected by disulfide ligands, with each cluster being composed of an Mo_6 octahedron surrounded by an X_8 cube.[112] Because of the drastically different structure and different Mo/S ratio from c-TMDs and a-TMCs, CP transition metal chalcogenides exhibit peculiar catalytic properties. In particular, the chalcogen centers are active for H adsorption, forming a X−H bond stronger than that of c-TMDs, due to the S p-band center being closer to the Fermi energy level. On the other hand, the Mo d-band center position shifts away from the Fermi energy level, thus realizing a weaker interaction with H.[113] The insertion of transition metals in the structure, where they occupy the cluster "cavity", represents an additional degree of freedom to fine-tune the electronic structure and catalytic activity of the material. CP transition metal chalcogenides showed a remarkable HER efficiency, where their activity surpassed that of 2H c-MoS_2 due to the higher density of active sites, both Mo and S, and to the improved charge transfer properties which resulted in faster HER kinetics.[114,115] The presence in the structure of transition metal atoms was exploited to fine-tune the interaction energy of the chalcogen centers with the HER intermediate and improve the reaction

https://doi.org/10.1021/acsmaterialsau.1c00006
ACS Mater. Au 2021, 1, 6−36

kinetics, as shown by Yan and collaborators through the synthesis of a Ni-containing Mo_3S_4 nanosized catalyst with hollow morphology,[116] or can decrease the energy barrier for electron transfer by creating efficient transfer pathways, as observed by Bae et al. for a Cu-containing Mo_6S_8 heterostructure.[117] As highlighted by Ortiz-Rodriguez et al.,[113] the electronegativity of the chalcogen atom in the CP structure is a critical parameter to optimize the HER performance. Indeed, as the electronegativity of the chalcogen atom increases (from Te to Se and S), so does its charge density, leading to a stronger X−H bond and to an easier HER energy profile.

The direct participation of the X atoms in the reactions through the formation of the X−H bond is extremely appealing toward the utilization of CP transition metal chalcogenides for CO_2R and NRR electrocatalysis, where the chalcogen centers can act as a proton donor to the adsorbed CO_2 or N_2. For the former reaction, this mechanism can shift the selectivity of catalyst toward value-added hydrogenated compounds like methanol by hydrogenating adsorbed *CO,[118] while for the NRR, this mechanism, similarly to what occurs on nitrogenase enzymes, improves the reaction energy profile by decreasing the energy barrier of the potential determining step (the first protonation of N_2) and by stabilizing the protonated reaction intermediates.[119]

3.2.3. Nanoscale Engineering and Nanosizing Effects. Since the electronic structure of the catalyst can be deeply modified by acting on the atomic and molecular organization, extensive effort has been devoted to fine-tune the nanoscale structure of group VI transition metal chalcogenides, and a number of reviews have detailed the modifications induced on the electronic structure and, consequently, the positive effects of this technique on HER activity as well as CO_2R performance.[20,35,120−124] The nanoscale engineering approach improves both the electrochemical surface area (ECSA) by maximizing the surface area to volume ratio and the intrinsic activity of the material because nanoscale effects like quantum confinement or plasmonic resonance modify the electronic structure at this length scale.[125] These modifications are particularly evident when few-layered c-TMDs or 0D quantum dot (QD) c-TMDs with minimal lateral dimension (<20 nm) are synthesized. For few-layered c-TMDs, the interlayer distance is a critical nanoscale structure parameter that influences the electronic structure and thus the catalytic activity. By changing this distance, the orbital interaction between two adjacent layers can be modified, as it increasingly weakens as the interlayer distance increases. In this way, the electronic structure of the layers is progressively modified until each layer can be considered isolated and with a different band structure from the multilayered material. A similar effect can be obtained by reducing the number of layers of the nanostructured material until a one-layered, 1D c-TMD is obtained.[126−128] In the case of HER, decreasing the number of layers of a c-MoS_2 catalyst maximizes the ECSA and, at the same time, modifies the electronic structure, improving the per-site TOF for hydrogen production.[129] On the other hand, in c-TMDs QDs quantum confinement and edge effects enhance the specific activity of the metallic sites by modifying their charge distribution, thus affecting the interaction with the adsorbates.[130,131] Additionally, the extremely high surface to volume ratio and the maximized exposure of active sites make QDs particularly appealing for electrocatalytic applications.[130] For the HER, the improved electron transfer of QDs markedly enhances the reaction kinetics, as demonstrated by the small Tafel slopes of 51 mV dec^{-1} obtained for WS_2 QDs synthesized by liquid exfoliation,[132] 1T MoS_2 QDs fabricated by electrochemically assisted Li intercalation (44 mV dec^{-1}),[133] and 1T-MoSeS QDs synthesized by Li intercalation (40 mV dec^{-1}).[111] Interestingly, the remarkable HER performance of these 1T-MoSeS QDs is related to structural distortions in the lattice due to the presence of Se vacancies of unsaturated metallic sites and of alloying effects between S and Se.

For a-TMC-based HER electrocatalysts, instead, the nanoscale engineering approach leverages the identification of the disulfide groups as active sites to tune the molybdenum and sulfur content in the material to maximize the HER activity. Indeed, maximization of the bridging disulfide groups and optimization of the Mo/S ratio in a-MoS_x-based materials were identified as effective engineering approaches to markedly improve the HER activity of these electrocatalysts, in terms of improved η_{10} values,[71,134] faster reaction kinetics as highlighted by the optimized Tafel slope values,[135] and higher per-site TOF for hydrogen production.[136,137]

The enhancements in electrochemical surface area and exposure of active sites granted by a precise structural engineering of the catalyst at the nanoscale are beneficial also on the CO_2R and NRR activity of TMD-based catalysts. Nevertheless, for these applications, it is critical to assess the effects of the nanoscale structural modifications on the electronic structure of the material to fabricate a selective catalyst because of the competition of the HER in aqueous electrolytes. For CO_2R, Li et al.[138] observed a remarkable catalytic performance, in terms of small overpotential and high selectivity for the reaction, for an edge-exposed c-MoS_2 catalyst with porous hierarchical nanostructure. For this catalytic architecture, the competing HER was suppressed by employing an ionic liquid-based electrolyte which hindered adsorption of protons and increased the solubility of CO_2. Control on the porosity of the catalyst is particularly appealing in the framework of CO_2R because porous architectures affect CO_2 permeability and electrolyte diffusion, thus influencing the selectivity of the catalyst toward different C products, similarly to what observed for copper-based porous nanostructured catalysts.[25] The positive correlation between active site exposure and improvement in catalytic activity was demonstrated also for NRR, where a boosted N_2 reduction performance was registered for a few-layered c-MoS_2 nanoflower catalyst with enlarged interlayer spacing.[139] Here, the improved NRR performance was strictly related to modifications in the electronic structured triggered by the presence of defects, which allowed the easier activation of the N_2 molecule (i.e., weakening the triple N≡N bond, allowing for reduction of the intermediate) and decreased the energy barrier of the potential determining step of the reaction. Indeed, when the defects in the catalyst were repaired, the selectivity toward the parasitic HER increased at the expense of that toward NH_3. A similar NRR performance enhancement was also observed for c-TMDs QDs, which exhibited a stronger binding with N_2 and an easier NRR energy profile due to the presence of many edge sites with unsaturated coordination and the abundance of chalcogen defects that altered the electronic structure of the catalyst.[131]

3.2.4. Doping. Previous works[140−142] demonstrated how the electronic structure of the active sites can be tailored to a specific catalytic application by inserting doping elements, both

https://doi.org/10.1021/acsmaterialsau.1c00006
ACS Mater. Au 2021, 1, 6−36

metallic and nonmetallic. This process modifies the electronic structure of the material, thus altering the interaction strength between reactants and active site[143] and influencing the electronic transport near the active sites, with a beneficial effect on the catalytic activity.[142]

The beneficial effect of this technique on the energy profile of the reaction was recently shown for the HER by Zang et al.,[144] who introduced C dopant into a c-MoS_2 catalyst, and by Huang et al.,[145] who incorporated Ni and O into a 1T c-MoS_2 material. In both cases, the activity of the catalyst was drastically improved, with 5-fold improvement in −10 mA cm^{-2} overpotential (η_{10}), faster kinetics, and enhanced charge transfer properties. The same effect was exploited for the HER application of a-TMCs, where the incorporation of nonmetallic elements such as O or N proved its effectiveness in enhancing the electrical conductivity of the material and thus the reaction kinetics. O incorporation in a supported a-MoS_x material formed a molybdenum oxysulfide catalytic phase with improved conductivity, which achieved an η_{10} of 164 mV and a Tafel slope of 43 mV dec^{-1}.[146] Similarly, in our group, we recently exploited the incorporation of O during the activation process of a hierarchical, nanostructured a-MoS_x catalyst to form reduced molybdenum oxide/oxysulfide phases with high conductivity, which markedly improved the HER kinetics, with a Tafel slope as small as 35 mV dec^{-1}, and a high per-site H_2 TOF up to 3.5 H_2 s^{-1} at −0.15 V_{RHE}.[147] Similarly, Ding et al.[148] observed an activity enhancement and a faster HER kinetics for a supported a-MoS_x HER catalyst with the introduction of a N dopant. Improved charge transfer properties and electrical conductivity were observed by Zheng et al. by incorporating nickel sulfide (Ni_3S_2) nanoflakes on a supported a-MoS_x HER electrocatalyst.[149]

Tuning the energy profile of the reaction through doping can facilitate the application of group VI transition metal chalcogenides for non-HER reduction reactions, as this strategy is an efficient way to optimize the interaction energy with critical reaction intermediates, as CO* for CO_2R or NH_3* for NRR. Introduction of a Nb dopant[150] or N atoms[151] in c-MoS_2 catalysts improved the CO_2R efficiency of the material, due to a more efficient charge transfer near the active sites and due to an energetically easier desorption of the *CO intermediate. Furthermore, DFT studies suggested that the introduction of Ni at the S-edge sites of c-MoS_2 can decrease the binding energy of CO* to enable CO_2 transformation to more complex products than CO.

The modifications in electronic structure triggered by the doping process can be fine-tuned to control the selectivity of the material for the desired electrocatalytic application against the competitive HER, a particularly appealing topic for nitrogen reduction in protic solvents. For this reaction, introducing dopant elements in the basal plane makes this region of the material catalytically active by creating new gap states that favor adsorption of reactants on the basal sites and by modifying the charge distribution in the basal plane.[140,152,153] This process not only facilitates the adsorption and activation of the N_2 molecule to improve the energy profile of the NRR but also affects the energy profile of the HER, making the adsorption of protons and their interaction with the active dopant site less energetically favored than the interaction with N_2*, as proposed by DFT calculations.[154]

3.2.5. Defect Engineering. Previous theoretical and experimental works demonstrated the possibility to modify the electronic structure by introducing defects (i.e., chalcogen vacancies) or distortion in the lattice of the material. The introduction of defects and distortion is the main technique employed to activate the otherwise inert basal plane. The activity of the vacancy sites has been extensively studied in the literature:[47,155−159] the missing chalcogen atom exposes the underlying metal site, whose dangling bonds states of the d-orbital are responsible for the formation of the gap states near the Fermi level, with an energy reaching that of the Fermi level as the chalcogen vacancy percentage increases. These gap states can hybridize with the orbitals of the reactant, thus favoring their adsorption and improving the catalytic activity of the material. For example, when the reactant is H, this leads to stronger H* adsorption. For c-MoS_2, a sulfur vacancy percentage ranging from 7 to 13%[155,157] maximized the activity of the exposed Mo atoms, while above this percentage the catalyst surface is unstable. Voiry and collaborators[160] showed that the higher activity and TOF in a defect-dense c-MoS_2 with respect to the "pure" material were related to the formation of both point defect sites and broader regions stripped with S and characterized by many undercoordinated Mo sites. The same effect can be achieved by applying compressive or tensile strains to the basal plane.[152,155] Indeed, DFT simulations revealed that inducing a strain in the basal planes of different c-TMDs, e.g., c-MoS_2[152] or c-WS_2,[161] influences the adsorption energy of reactants by increasing the density of states near the Fermi level.

These changes in electronic structure affect not only the HER but also the NRR activity of c-TMDs. For the latter application, the additional gap states created by the vacancies are critical to activate the N_2 molecule. Indeed, the metal centers exposed by the chalcogen vacancies have d-orbitals that hybridize with the N p-orbitals, thus facilitating the electron transfer to the adsorbate.[162] Additionally, on defective sites, the NRR intermediates have a different coordination than the edge sites, improving the energy profile of the reaction.[139] Lastly, for CO_2R, the changes in electronic structure and the nanoscale distortions in the lattice induced by the chalcogen vacancies at the basal plane can favor specific CO_2 reduction pathways, like ones where protonation steps involve different atoms of the adsorbate[163] or where non-electron-coupled transfers occur,[164] which are unfeasible on edge sites. As different CO_2R mechanisms lead to distinct reaction products,[165] the possibility to control the quantity of edge sites and defective chalcogen sites represents, in principle, a powerful tool to control the mix of reduction products evolved.

3.2.6. Support Coupling. The deposition of a thin, nanometer layer of group VI transition metal chalcogenide catalyst on top of a support material with well-defined morphological and electrical properties makes possible the optimization of the exposure of the active sites and the maximization of the electrochemical surface area of the resulting catalytic architecture. This technique found widespread application for HER electrocatalysis and was discussed in detail in comprehensive review works.[19,166−168] Coupling the catalyst layer with a conductive support with controlled mesoscale morphology is particularly effective for a-TMCs. Indeed, despite their high intrinsic activity, these materials are usually synthesized by low-temperature routes to obtain mesoporous structures with suboptimal exposure of active sites. On the other hand, the coupling with conductive supports, usually carbon-based, drastically improves the electrochemical surface area as well as the conductivity of the architecture. In this regard, Ye et al.[169] synthesized

https://doi.org/10.1021/acsmaterialsau.1c00006
ACS Mater. Au 2021, 1, 6−36

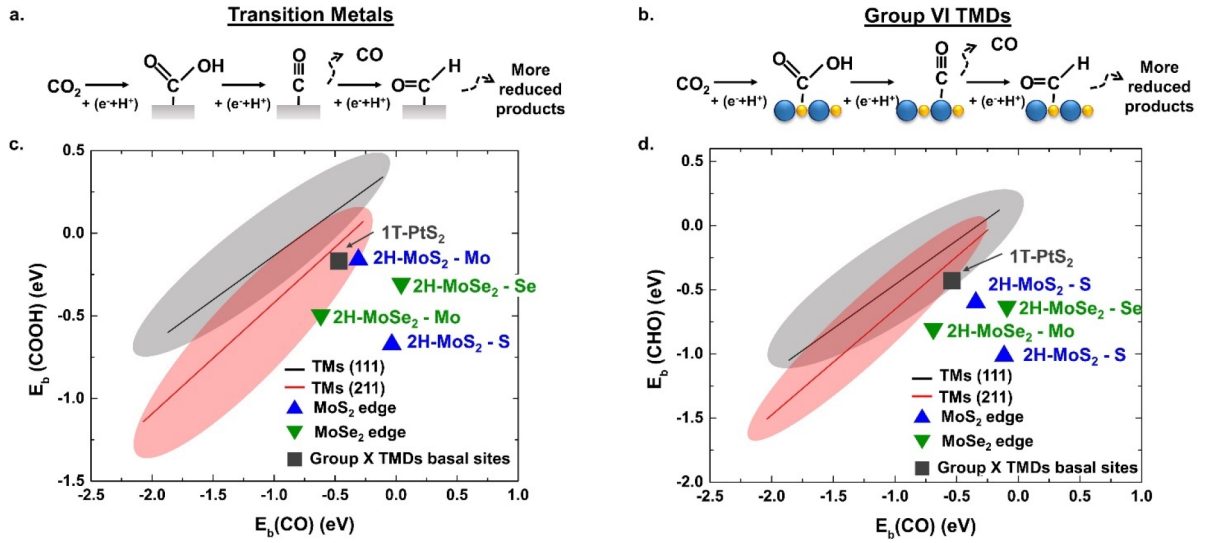

Figure 4. (a) CO_2 reduction schematics for the first reaction steps, showing the initial PCET that activates CO_2 and leads to the formation of CO*, on transition metal catalysts. (b) Schematic representation of the CO_2 to CO reduction mechanism, proposed by ref 38, on group VI TMD edge sites. The blue ball represents the metal atom, whereas the yellow ball represents the chalcogen atom. The successive reaction intermediates are bound at two different sites, thus overcoming the energetically unfavorable scaling relations. (c) Overview of CO* binding energy, E_B(CO), versus COOH* binding energy, E_B(COOH), and (d) CO* binding energy, E_B(CO), versus CHO* binding energy, E_B(CHO), for the active sites of group VI molybdenum-based TMDs and group X TMDs (represented by crystalline 1T-PtS_2). The red and black lines show the linear energy scaling relations on (211) and (111) transition metal sites, respectively. The red and gray shaded areas represent the regions in which the DFT-calculated binding energies for COOH*, CO*, and CHO* for (211) and (111) transition metal sites, respectively, fall. The binding energies for transition metals and group VI TMD sites have been calculated by ref 38. The binding energy for group X TMDs has been calculated by ref 196.

nanospheres comprising a carbon-nanotube-supported a-MoS_x catalyst, achieving an η_{10} value of 168 mV and a remarkable Tafel slope value of 36 mV dec^{-1} due to the efficient electron transfer and exposure of active sites granted by the carbon nanotubes. The support/catalyst interaction can also enhance the catalyst stability: Li and collaborators[170] synthesized an acetylene-black-reduced graphene-oxide-supported a-MoS_x catalyst that exhibited an η_{10} value of 142 mV, a Tafel slope of 62 mV dec^{-1}, and a 30 h stability upon continuous operation at a current density of roughly −70 mA cm^{-2}. Moreover, Lu et al.[171] showed the high activity of an a-MoS_x catalyst confined inside a porous, honeycomb-like N-doped carbon material. The interaction between nitrogen and a-MoS_x, along with the high conductivity of the N-doped CMK-3, resulted in a high efficiency with an η_{10} of 184 mV and a reduced Tafel slope of 32 mV dec^{-1}. Lastly, by depositing an a-MoS_x catalyst on a gold-coated carbon cloth support with improved electrical conductivity, Wang et al.[172] achieved a good catalytic performance with an η_{10} of 180 mV and a Tafel slope of 48 mV dec^{-1}. In the framework of non-HER reduction reactions, the support coupling strategy is an appealing concept to steer the selectivity of the active sites toward the desired product. Indeed, at the catalyst/support interface, the strong interaction between the two phases alters the electronic structure of the active material, which can in turn modify the adsorption character of the catalytic sites as was shown for a CO_2R application by Yu et al.:[173] the electronic structure modifications at the interface between a c-MoS_2 catalyst and its TiO_2 3D scaffold drastically enhanced the adsorption energy for CO_2, improving the selectivity for this reaction at the expense of HER.

4. CO_2 REDUCTION REACTION

4.1. Reaction Mechanism and Scaling Relations on Transition Metals

The electrochemical reduction of carbon dioxide can be visualized as a multiple proton-coupled electron transfer (PCET) reaction that leads to different reduction products and water. The distribution of products depends on a variety of factors like catalyst material, nature of the active sites, applied potential, and local pH, which influence the reaction pathway to the formation of up to 16 products.[174] A straightforward figure of catalytic performance that is always reported for CO_2R catalysts is the Faradaic efficiency (FE) toward a specific reduction product, which describes the percentage of the total charge passed through the electrode that is transferred to the specific product, thus quantifying the selectivity of the catalytic material for the conversion of CO_2 to the desired species. The partial current density for a certain product, that is, the product of the total current density and of the Faradaic efficiency toward that reaction product, is another important figure of merit that translates the overall activity of the catalytic surface because it takes into account the yield of the specific reaction product. A complete discussion on the CO_2R figures of performance to be reported for catalysts for this application, along with a series of standardized methods and setups to measure, reports the experimental data and compare them to state-of-the-art CO_2R catalysts can be found in another work,[175] to which the reader may refer.

When performed in aqueous electrolytes, the CO_2R suffers from the competition of the HER, which takes place in the same potential range of the CO_2R with smaller thermodynamic barriers, due to the energetically easier proton adsorption and reduction than CO_2 activation. Indeed, the high stability of the CO_2 molecule requires high overpotentials to be applied in order for the reactant to be adsorbed and activated at the

https://doi.org/10.1021/acsmaterialsau.1c00006
ACS Mater. Au 2021, 1, 6−36

active site. However, at high overpotentials, the HER is more favorable than the CO_2R due to a faster kinetics, resulting in high FE for hydrogen at the expense of the selectivity for CO_2 reduction products. Consequently, particular attention should be placed on the design of catalytic systems that maximize product selectivity for CO_2R and suppress proton reduction as much as possible. CO_2R catalysts can be divided in four broad categories according to their main reaction products: the first one is composed of metals as Pd, Pt, and Ni, which are selective for the competing reaction, i.e., the HER; the second one includes Au, Ag, and Zn that mainly produce CO.[6,176,177] The third one comprises Cd, Pb, and Sn, whose main reduction product is formate,[178,179] whereas the last group is represented by Cu, which can reduce CO further to more complex C_2,[180] C_3,[25] and oxygenated species,[181] making it the most studied and interesting catalyst for a commercial application of the technology. This classification can be further addressed by analyzing the different groups in the frame of their CO* and H* binding energy. Weak CO* and H* binding lead to a favored HER versus CO_2R, whereas stronger H* bonding ($\Delta E_{H^*} > 0.3$ eV) and stronger CO* bonding ($\Delta E_{CO^*} \approx -0.2$ eV) lead to either CO or HCOOH products[182] (the differentiation between the latter also arises from the CO_2 binding conformation on the metal surface). Finally, Cu illustrates itself by being an "intermediate" binder, i.e., on Cu, $\Delta E_{H^*} \approx 0$ eV and $\Delta E_{CO^*} \approx -0.5$ eV.[178,182] Differently from the HER, in the CO_2R, up to 12 electrons can be transferred in a series of irreversible elementary steps, whose sequencing is still debated in the community.[24,26,183−185] In the reaction mechanism, gaseous CO_2 is adsorbed on the active site, with the adsorption conformation being critical in the CO_2R pathway. An adsorption through one of the oxygen atoms leads to the formation of formate, whereas an adsorption through the carbon results in the CO_2 undergoing two PCET steps forming the CO* intermediate[186] that can either be released from the catalyst surface as gaseous CO or undergo further reduction, as visualized in Figure 4a. At this point in the reaction, different products can be obtained according to a series of thermodynamics (i.e., binding strength of various intermediates), kinetics, and experimental parameters like type of active site, applied potential, or local pH. It is worth noting that the synthesis of complex C_n products ($n > 2$) on copper takes place by a Langmuir−Hinshelwood mechanism, where adsorbates on neighboring sites interact to form other intermediates that push the selectivity of the reaction to specific products. On transition metal catalysts, it has been established that the key potential-dependent elementary steps are the following (eqs 1−3):[38,187]

$$CO_2(g) + (H^+ + e^-) \rightarrow COOH^* \quad (1)$$

$$COOH^* + (H^+ + e^-) \rightarrow CO^* + H_2O(l) \quad (2)$$

$$CO^* + (H^+ + e^-) \rightarrow CHO^* \quad (3)$$

where the asterisk indicates an adsorbed species. To efficiently reduce CO_2 to CO, a good catalyst should be thus characterized by a strong adsorption energy for the COOH* intermediate and by a low binding energy for CO*, so that the first intermediate is strongly stabilized on the surface for its protonation and the as-formed product can leave the active site. To further reduce CO*, the first limiting step is the proton-coupled electron transfer to form the CHO* intermediate, whose adsorption energy should be strong enough to guarantee further reductions. However, thermodynamic studies by DFT calculations have shown that the adsorption energies of the COOH* and CHO* intermediates, E_B(COOH*) and E_B(CHO*), linearly scale with the binding energy of CO*, limiting the activity of these catalysts. Highly active CO_2R catalysts like gold or copper manage to stabilize the COOH* or CHO* intermediates more than CO*, breaking these scaling relations.[187,188]

4.2. Transition Metal Chalcogenides as CO_2 Reduction Catalysts

Considering that the scaling relations limit the activity of transition metal catalysts, transition metal chalcogenides gained research interest as possible CO_2 reduction catalysts due to the similarity of their active sites to that of Fe_xNi_yS cubanes,[189] where the binding of the three CO_2R intermediates shown in eqs 1−3 occurs on different atoms, thus overcoming the limiting scaling relations. Focus has been placed mainly on group VI transition metal chalcogenides, as by thermodynamic criteria they can outperform the state-of-the-art transition metal catalysts for CO_2 reduction,[38] while research interest in transition metal chalcogenides with metals from different group than VI is more recent. Regarding nonlayered transition metal chalcogenides, Fe- and Ni-based sulfides, whose structure is very similar to the active sites of dehydrogenase enzymes, showed good CO_2 reduction activity, with a $Fe_{4.5}Ni_{4.5}S_8$ catalyst achieving a maximum 87% FE_{CO} at −1.8 V_{NHE} in an aprotic, acetonitrile-based $TBAPF_6$ (tetrabutylammonium hexafluorophosphate) electrolyte,[190] and an FeS_2/NiS composite showing a 64% FE for methanol at −0.6 V_{RHE} in an aqueous $KHCO_3$ electrolyte.[191] Furthermore, Gao et al. synthesized CdS nanoneedles which, due to the curved morphology that enhanced the local electric field, achieved a maximum 95.5% FE for CO at −1.2 V_{RHE} in an aqueous $KHCO_3$ electrolyte. Lastly, copper-based chalcogenides showed high CO_2 reduction activity,[192,193] but the actual catalytic phase in these materials is metallic Cu, derived from the in situ reduction of the chalcogenide phase at cathodic potentials.[194] Regarding layered, nongroup VI chalcogenides, titanium disulfide was proposed as CO_2R electrocatalysis: as shown by Aljabour et al.,[195] TiS_2 thin films have semimetallic nature and exhibit sulfur active sites at their basal plane, allowing them to efficiently reduce CO_2 to CO with an 83% FE −0.5 V_{RHE} in an acetonitrile-based $TBAPF_6$ electrolyte.

Nørskov and colleagues,[38] employing the binding energy of CO_2 intermediates as activity descriptors, showed that the S and Se chalcogen edge sites from c-MoS_2 and c-$MoSe_2$ selectively bind the COOH* and CHO* intermediates over CO*, which instead is bound to the metal edge atom, as shown in Figure 4b. The intermediates adsorption on two different sites leads to a deviation from the limiting scaling relations, which is visualized in Figure 4c,d. This binding configuration allows the COOH* and CHO* intermediates to be stabilized more than CO* and represents a thermodynamic condition for an improved CO_2R activity with respect to transition metals. Additionally, it improves the energy profile of the reaction minimizing the CO_2R limiting potential U_L (that is, the potential at which all reaction steps become exergonic). In this way, all c-TMD edge sites, with the exception of the c-MoS_2 S-edges, are characterized by U_L smaller than that of Au(211), the most active facet for CO_2 to CO reduction on this metal, and are thus more active than gold. The $MoSe_2$ Se-edge

https://doi.org/10.1021/acsmaterialsau.1c00006
ACS Mater. Au 2021, 1, 6−36

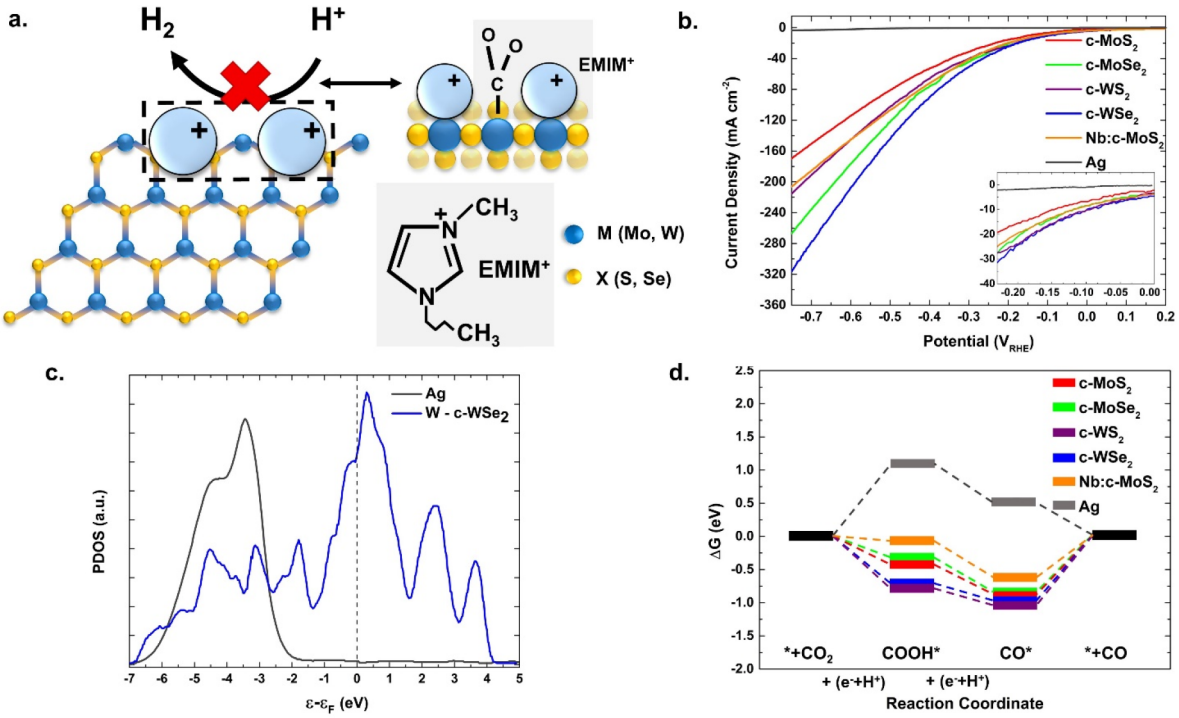

Figure 5. Overview of the CO_2 reduction activity of group VI TMDs in ionic liquid (e.g., EMIM-BF_4) electrolytes. (a) Cartoon representation of the interaction between edge metal site and EMIM+ additive to facilitate the adsorption of CO_2 at the active site, through the formation of the EMIM-CO_2 complex. (b) LSV curves for the different TMDs[39] and for a Nb-doped c-MoS_2 (Nb:c-MoS_2 in the figure) catalyst[150] in EMIM-BF_4 electrolyte. The performance trend of WSe_2 > $MoSe_2$ > WS_2 > MoS_2 can be observed from the voltammograms, while Ag nanoparticles (gray trace) are reported as reference. The insertion of a Nb dopant element near the edge sites influences the productivity of the active sites by changing the electronic structure of the material. (c) DFT-calculated projected density of states (PDOS)[39] for the W metal edge site in c-WSe_2, compared to that of surface Ag atoms in a nanoparticle conformation (gray trace). The d-band center of the W metal edge site is closer to the Fermi energy level; therefore, a binding with CO_2 stronger than that with Ag is realized on the TMDs active sites. (d) Free energy variation for the intermediates in CO_2 reduction to CO on group VI TMDs and on Nb-doped c-MoS_2 in EMIM-BF_4 electrolyte, derived from the calculations shown in refs 39 and 150. respectively. All TMDs are characterized by activity better than that of the Ag nanoparticle reference (gray trace), due to the lower work function and d-band center closer to the Fermi energy. The insertion of the Nb dopant modifies the electronic structure of the edge active site and the position of the d-band center, further improving the energy profile of the reaction and facilitating the desorption of CO*.

exhibits the smallest U_L = −0.48 V_{RHE}. At the same time, $MoSe_2$ and Ni-doped c-MoS_2 are, by thermodynamic criteria, more active than Cu for CO_2 reduction to CH_4, as they are characterized by U_L of −0.38 V_{RHE} and −0.28 V_{RHE}, respectively, whereas for Cu, U_L = −0.69 V_{RHE}. Recent DFT investigation suggested that the basal sites of metallic group X transition metal chalcogenides deviate from the energy scaling relations and may be highly active for the CO_2R.[196] Similarly to c-MoS_2 edges, group X basal sites are proposed to be more active than Au for CO production due to the lower binding energy of COOH*, while differently from group VI, they should not suffer from OH poisoning and are less active toward HER, due to the higher H* binding energy.

It is critical to emphasize the major role that ionic liquids (ILs, as 1-ethyl-3-methilimidazolium tetrafluoroborate, EMIM-BF_4) play for the CO_2R activity of group VI transition metal chalcogenides. ILs' presence decreases the H^+ concentration in the electrolyte and improves the solubility of CO_2, thus steering the selectivity toward the CO_2R. In addition, the presence of [EMIM-BF_4] results in the formation of [EMIM-CO_2]* complexes with a decreased energy barrier for the first e^- transfer; i.e., according to Saheli-Khojin and collaborators, $[EMIM]^+$ is bound on the electrocatalyst surface and then forms the highly reactive [EMIM-CO_2]* complex (Figure 5a).[197] Studies from Li et al. underlined the role played by the amine group present in the ionic liquid, through the use of polyethylenimine (PEI) as an additive in their a-MoS_x/reduced graphene oxide electrocatalysts, which also hindered the HER, along with increasing the CO_2R kinetics, through the stabilization of the COOH* intermediate, reaching a CO_2 to CO Faradaic efficiency of 85% at −0.65 V_{RHE}.[198] Indeed, when PEI was removed from the catalytic architecture, a 95% Faradaic efficiency for hydrogen was registered and the CO_2R activity was lost. Overall, modifications of the electrolyte are extremely beneficial for CO_2R on these catalysts. Recently, Asadi et al. investigated the impact of KOH/choline chloride ionic liquid electrolyte on the CO_2R activity of c-MoS_2, which proved superior to the activity in EMIM-BF_4-based electrolyte.[199]

Differently, in aqueous electrolytes, the CO_2 reduction activity of c-MoS_2, along with several other c-TMDs, is strictly related to the competition of HER and CO_2R taking place at the same active sites because of the excellent electrocatalytic activity for the HER of this class of materials. As evidenced by Chan et al.[38] and Landers et al.,[200] for an electrocatalyst to favor the CO_2R versus the HER, a difference of less of 0.5 V should exist between their limiting potentials (the 0.5 V arises from the destabilization of H* species when CO* reach its equilibrium coverage during CO_2R, i.e., ΔG_{H^*} increases by ∼0.5 eV), a difference which is observed for none of the group VI transition metal chalcogenides, with the exception of Ni-doped c-MoS_2. The latter is limited by kinetics and, more

https://doi.org/10.1021/acsmaterialsau.1c00006
ACS Mater. Au 2021, 1, 6−36

specifically, by the proton−electron transfer required for the CO* → CHO* step which, on c-MoS_2, includes a displacement of the reactive molecule from the metallic to the sulfur site. Although this aspect is of little importance for metal electrocatalysts (e.g., Cu, Sn, etc.), it is critical when addressing multisite nanostructures. Due to those limitations (i.e., high activity for the HER, combined to an eventual poisoning of the actives sites by OH*), group VI transition metal chalcogenides were deemed as limited for CO_2R in aqueous electrolyte, but, as mentioned above, recent thermodynamics findings by Ji et al. underlined the potential of group X transition metal chalcogenides for CO_2R.[196]

The combination of the aspects listed above is responsible for the extensive amount of research in ionic liquid-modified electrolyte, which led to promising findings on group VI transition metal chalcogenides, while in aqueous electrolytes the thermodynamic and kinetic predominance of the HER results in very small CO_2R activity and hydrogen FE close to unity. For example, Salehi-Khojin and collaborators[39,201] showed the high CO_2 reduction activity of group VI c-TMDs in ionic liquid EMIM-BF_4 electrolyte, as visualized in Figure 5b. c-TMD nanoflakes with a mean size of ≈100 nm, fabricated with a chemical vapor transport technique, outperformed gold and silver, the more active transition metal catalysts for CO_2 to CO reduction, in terms of current density and product yield. Indeed, the partial current density ascribed to CO (calculated as product between Faradaic efficiency and total current density) evolution on the c-TMDs was roughly 1 order of magnitude larger than that registered for Ag and Au. The better performance than Ag and Au was related to the d-band of the W and Mo metallic edge atoms, whose center is closer to the Fermi energy level than the two noble metals, as illustrated by the DFT-calculated projected density of states (PDOS) of the WSe_2 W-edges in Figure 5c, thus realizing a stronger binding for the first COOH* intermediate. As a result, the initial COOH* formation step is exergonic (while it is endergonic for Ag) requiring a smaller overpotential, and the rate-determining step becomes the final CO* desorption (Figure 5d). The role played by the edges hints toward the design of optimal c-TMDs for CO_2R, i.e., vertically oriented sheets[150,201] or a-MoS_x,[198] as the latter contain a high density of unsaturated sites with electronic properties similar to the edges sites of c-MoS_2. The efficiency of the c-TMD catalysts was related to their work function and charge transfer resistance: the lower the two parameters for the c-TMD, the better the performance. Consequently, the best performing catalyst was c-WSe_2, characterized by a per-site TOF of ≈10 CO s^{-1} at an applied overpotential of ≈550 mV, followed by c-$MoSe_2$, c-WS_2, and c-MoS_2. As a comparison, the per-site TOF for Ag was ≈0.02 CO s^{-1} at the same overpotential. The high catalytic efficiency of c-TMDs was maintained also in other IL electrolytes: indeed, as mentioned above, Asadi et al.[199] showed, for a c-MoS_2 catalyst in a PV-assisted CO_2 electrolysis cell, a CO Faradaic efficiency of ≈93% employing a choline chloride/KOH electrolyte.

The introduction of dopants can further improve the catalytic efficiency by modifying the electronic structure of the edge sites, tailoring the adsorption energies of the key COOH*, CHO*, and CO* intermediates to increase the reducing activity or the selectivity to complex products. Nørskov and collaborators[143] screened a wide variety of metallic dopants and evaluated their influence on the intermediate adsorption energies on a c-MoS_2 catalyst, identifying nickel and cobalt as the most promising nonprecious metallic dopants: both elements facilitate the CO* to CHO* reaction step, decreasing its required energy and the overpotential required by the reaction. Nickel was considered the most promising because it optimized the selectivity for CO_2 against the competing HER and minimized the limiting potential of CO_2 reduction to complex products beyond CO: this improvement arises from the enhanced stabilization of the CO* intermediate on the metal edge sites, endowing Ni-doped c-MoS_2 with a CO_2 to CH_4 reduction activity higher than that of copper. Despite this thermodynamic calculation, as previously mentioned, the kinetic barrier associated with the CO* → CHO* step is energetically unfavorable and further CO reduction is hindered. The activity improvement through the insertion of dopants near the metallic edge sites was confirmed in the case of both metallic[150] and nonmetallic[151,202] elements. Abbasi et al.[150] fabricated by a chemical vapor deposition method of Nb-doped c-MoS_2 vertically aligned nanosheets and evaluated the change in CO_2 reduction activity induced by the dopant with respect to an undoped c-MoS_2 catalyst with the same morphology. By optimizing the percentage of the metal dopant (5% atomic), the Nb-doped c-MoS_2 showed a remarkable activity in EMIM-BF_4 electrolyte, as shown in Figure 5b,d, with a maximum current density of 237 mA cm^{-2} at −0.8 V_{RHE}, a CO Faradaic efficiency up to 82% at the same potential, and a turnover frequency that, at small overpotentials, surpasses that of Ag by 2 orders of magnitude and that of c-MoS_2 by 1 order of magnitude. The activity enhancement with respect to the undoped c-MoS_2 stems from the Nb atoms near the Mo-edges that modify the electronic structure of the active sites, by shifting the Mo d-band center energy and weakening the CO* binding. This modification leads to an easier CO* desorption, the rate-determining step of the reaction, allowing for a smaller overpotential and faster turnover rate. A similar adsorption energy tuning through doping has been achieved by Lv et al.:[151] by doping c-MoS_2 with 8.4% nitrogen and coupling the catalyst to a N-doped carbon support, the electrical conductivity of the material was increased and the adsorption energy of the COOH* intermediate was optimized, leading to a small overpotential of 130 mV for CO formation in EMIM-BF_4 ionic liquid and a maximum CO Faradaic efficiency of 90% at −0.9 V_{RHE}, higher than the 65% FE registered in the same condition by undoped c-MoS_2. Xu and collaborators[202] further pushed this design strategy by evaluating the CO_2 reduction activity enhancement of a ternary TMD alloy, c-MoSeS, fabricated by the solvothermal method, with respect to c-MoS_2 and c-$MoSe_2$ in an ionic liquid. The ternary alloy attains a 45% CO Faradaic efficiency at −1.15 V_{RHE} in EMIM-BF_4 IL, larger than the 17% efficiency of c-MoS_2 and the 31% registered by c-$MoSe_2$, due to the peculiar electronic structure of c-MoSeS: with respect to c-MoS_2 and c-$MoSe_2$, the ternary alloy is characterized by a higher density of states near the conduction edge and a lower work function, resulting in a faster electron transfer to the adsorbates, and by a faster COOH* and CO* formation rate due to the improved electrical conductivity and improved stabilization on two Mo sites of the COOH* intermediate.

Similarly to the HER, the inert basal planes can be activated for the CO_2R by modifying their electronic structure through the creation of chalcogen vacancies or the formation of strains through the chalcogen sheet. Indeed, chalcogen vacancies usually occur during synthesis of c-TMDs like c-MoS_2, with an

https://doi.org/10.1021/acsmaterialsau.1c00006
ACS Mater. Au 2021, 1, 6−36

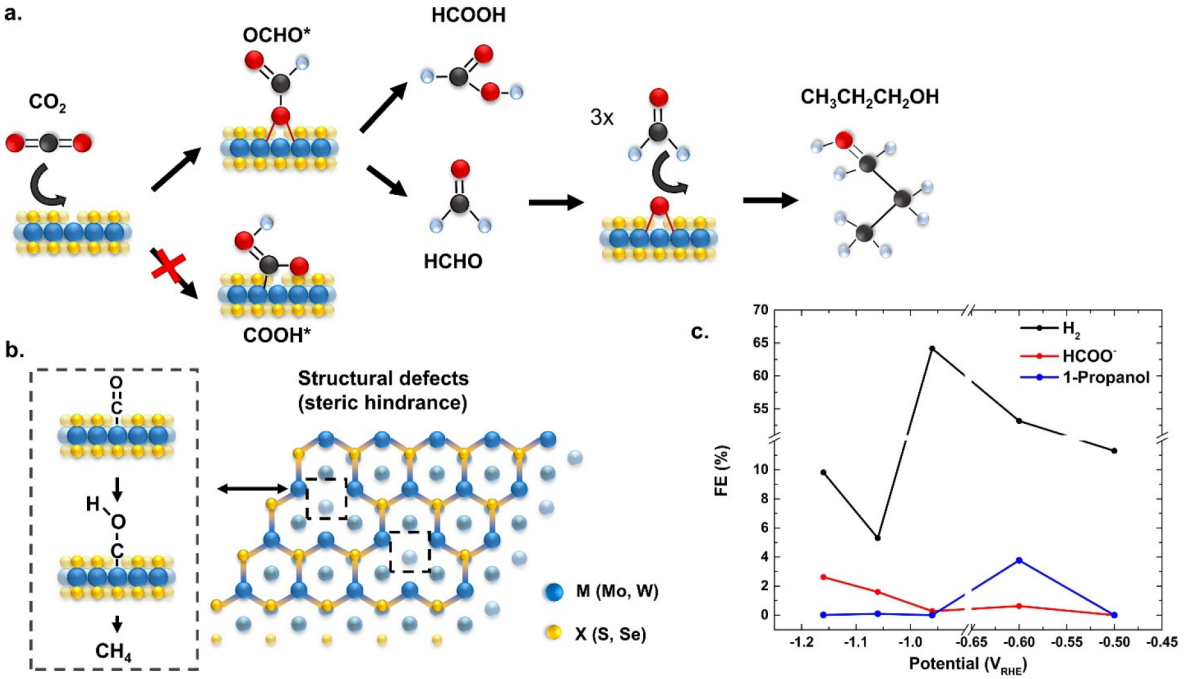

Figure 6. Overview of the CO_2R activity at the basal sites of group VI TMDs in aqueous media. (a) Schematic representation of the proposed reaction pathway for CO_2 reduction to 1-propanol on sulfur vacancy sites at a c-MoS_2 basal plane, according to the reaction pathway proposed in ref 164. The OCHO* intermediate is energetically favored over the COOH* intermediate because the steric hindrance effect at the vacancy site hinders the adsorption of COOH* due to its geometric configuration. (b) Cartoon representation of the steric hindrance effect at the chalcogen vacancy sites in a c-MoS_2 catalyst, as proposed by ref 163. The peculiar geometric conformation of the vacancy sites promotes a binding configuration of CO_2 at the metal atom different than the edge site, thus promoting different reaction pathway for the formation of CH_4. (c) Faradaic efficiency toward formate and 1-propanol for a c-MoS_2 catalyst in aqueous electrolyte, where the defect sites at the basal plane perform CO_2R. The experimental result supports the idea of the different reaction pathway at the defective sites of the basal plane. Adapted from ref 203. Copyright 2018 American Chemical Society.

S-vacancy concentration up to ≈10%.[157] The chalcogen vacancies on the basal planes create a "bowl"-shaped site, forming subgap states that are inherently localized on the vacancy:[164] differently from metals, where electrons are localized on the active site only when a proton is incoming and thus proton/electron transfers are coupled, these localized subgap states allow for a decoupled proton/electron transfer. The first CO_2 protonation forms the OCHO* intermediate instead of the COOH* adsorbate because the bowl shape sterically hinders a two-atom incorporation on the adsorption site, pushing the selectivity of the reaction not toward CO but toward formaldehyde (HCHO), formic acid (HCOOH), or 1-propanol, with a mechanism outlined in Figure 6a.[164] On the vacancy site, more interestingly, the formation of C_n ($n > 2$) can readily occur through a Eley−Rideal mechanism, where the OCHO* intermediate interacts with CO_2 or HCHO molecules dissolved in the electrolyte: this mechanism is unfeasible on Cu catalysts, where C_n products are created through a C−C coupling between CO* adsorbed on adjacent sites[185] but can thermodynamically occur on sulfur vacancy sites where the sp^2 carbon atoms of the OCHO* intermediate are exposed to the electrolyte and can readily react with neighboring dissolved species.[164] Moreover, the "bowl" conformation of the vacancy site favors the production of methane (CH_4) when CO instead of CO_2 is fed to the c-MoS_2 catalyst, as theoretically predicted by Chen et al.[163] and illustrated in Figure 6b. Sulfur vacancies cause a uniaxial elastic strain on the basal plane, favoring the protonation of adsorbed CO* to form COH* as stable intermediate and the consequent formation of CH_4. On these vacancies, the formation of CH_4 can be achieved at an overpotential 210 mV smaller than that on Cu(211) sites. These theoretical works found an experimental correspondence in a study by Francis et al.,[203] where a c-MoS_2 catalyst with low edge site density was able to reduce CO_2 to various C_n products (1-propanol, formate, *t*-butanol, and ethylene glycol) in aqueous $NaHCO_3$ electrolyte, although with a maximum Faradaic efficiency of 3.5% for 1-propanol (Figure 6c). In this operating conditions, i.e., IL-free, aqueous electrolyte, the basal plane was confirmed to be the catalytic site for the CO_2R, as by increasing the density of edge sites the selectivity for the parasitic HER was increased, and a "volcano"-like trend was observed between the 1-propanol FE and applied potential: for potentials smaller than the required CO_2R activation energy ($V > -0.5$ V_{RHE}), the HER is the only reaction, whereas when the potential is swept toward more cathodic values ($V \leftarrow 0.9$ V_{RHE}), the HER is the favored reaction as, due to its faster kinetics at this high applied overpotentials, the active sites are covered by H^+ and CO_2 adsorption is difficult. Interestingly, when gaseous CO was dissolved in the electrolyte, CH_4 was detected as reaction product, in accordance with the theoretical consideration reported in other works.[163]

A similar shift in selectivity can be obtained by employing Chevrel phase transition metal chalcogenide-based catalysts, where CO_2 can be transformed into value-added products like methanol. DFT calculations by Liu et al.[118] showed how this conversion occurs on Mo_6S_8 through a different mechanism than the one occurring at the edge sites of c-TMDs, consisting of successive hydrogenation steps to convert CO_2 to CO and then methanol. This mechanism takes place because of the

https://doi.org/10.1021/acsmaterialsau.1c00006
ACS Mater. Au 2021, 1, 6−36

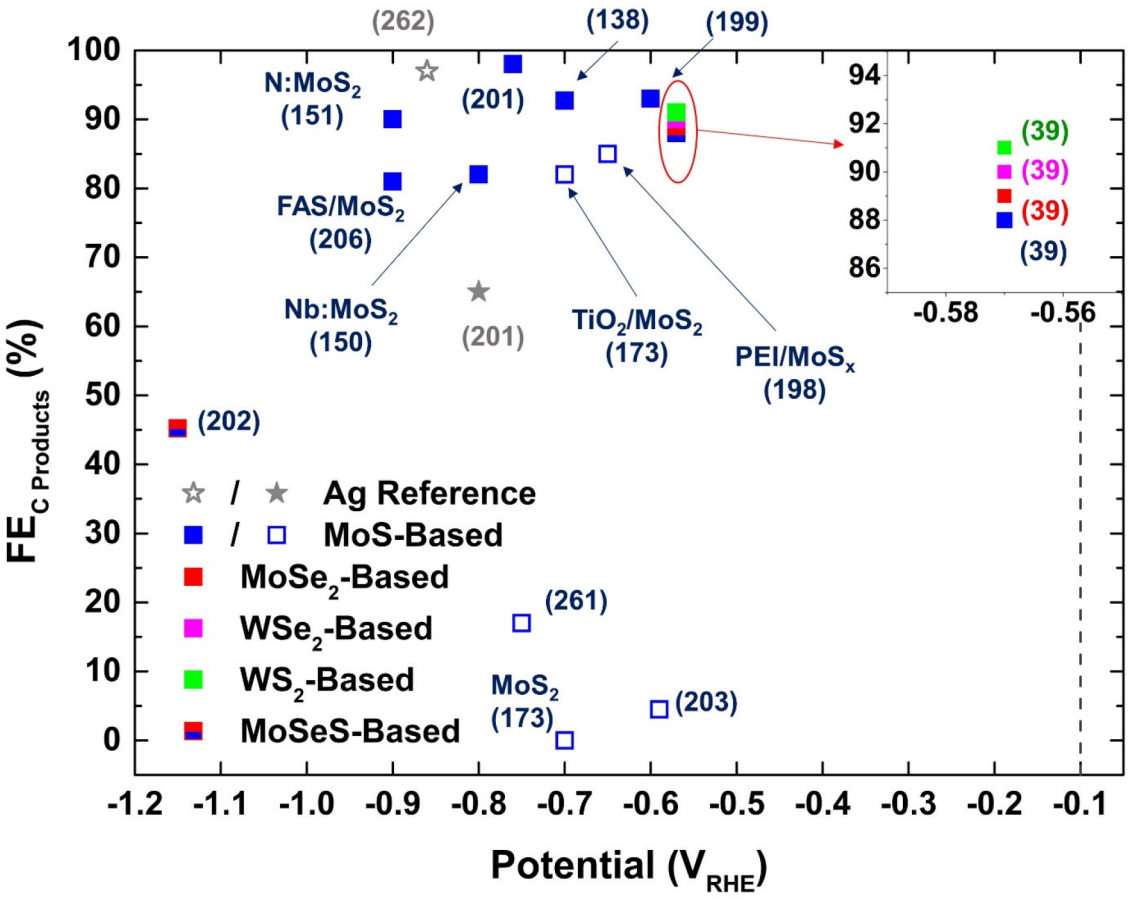

Figure 7. CO_2R performance comparison of representative molybdenum-[39,138,206,261,150,151,173,198,199,201−203] and tungsten-based[39] chalcogenides in terms of total FE for C products and potential of maximum selectivity. The dashed vertical line represents the equilibrium potential of the CO_2 to CO reduction reaction. The filled symbols represent catalysts tested in ionic liquids, whereas the open symbols represent catalysts tested in aqueous electrolytes. The Ag benchmark in aqueous electrolyte is derived from ref 262 and in ionic liquid from ref 201. When the catalyst is tested in its stoichiometrically pure form, only the reference is reported in the brackets, whereas any eventual presence of dopants or cocatalytic additives is reported in the plot before the corresponding reference in the brackets.

peculiar structural and electronic features of Mo_6S_8, where, due to the higher coordination number of Mo, the metallic sites and chalcogen centers are, respectively, more positively charged and less negatively charged than c-MoS_2. The consequent downshift of the Mo d-band center with respect to the Fermi energy level makes the Mo centers less active, so that they weakly bind CO_2 from the O atom and cannot activate the molecule by bending the double C═O bond. At the same time, the S p-band center upshifts toward the Fermi energy level, making the S atoms more active for the reaction. Indeed, they actively contribute to H binding along with Mo atoms and stabilize the reaction intermediates to facilitate the sequential hydrogenations of CO_2 to HOCO*, CO*, and then to CH_3OH. The energy profile of the reaction can be optimized by introducing metal elements in the structure. In particular, the same group observed an improved stabilization of the H_xCO_y* intermediates after the introduction of potassium, due to the formation of K^+ centers which interacted electrostatically with the adsorbates.[204] Reduction of CO_2 to CH_3OH was experimentally confirmed by Velázquez and collaborators,[205] who tested the CO_2R activity of a Cu-containing Mo_6S_8 catalyst in Na_2CO_3 aqueous electrolyte. Despite the predominance of the HER, which accounted for ≈95% FE, reduction of CO_2 to CH_3OH and formate was observed from −0.4 V_{RHE} to −1 V_{RHE}. The reaction rate was limited by the weak adsorption of CO_2 at the Mo sites, while the presence of formate was ascribed to an insufficient stabilization of the HOCO* intermediate against adsorbed $HCOO^-$. When employing a gaseous CO feed, only CH_3OH was observed, confirming that the reaction proceeds through hydrogenation.

In summary, when the HER is suppressed, group VI transition metal chalcogenides exhibit an exceptional CO_2 reduction activity, outperforming silver, the state-of-the-art metallic catalyst for CO_2 reduction to CO in terms of both FE_{CO} and current density due to C product formation, as visualized by the performance comparison reported in Figure 7. Based on these sole parameters, c-TMDs may represent the new benchmark for electrochemical CO synthesis. Nevertheless, as of today, their practical implementation as catalysts in CO_2 electrolyzers is unfeasible because of the predominance of the HER on the active edge sites in aqueous electrolytes, unless an efficient method to suppress the HER is implemented in the catalytic architecture. As presented in earlier sections, several solutions were found to hinder the HER, such as the use of ILs, choline, or PEI. Similar phenomenon could be achieved through the modification of the electrocatalyst composition; i.e., Yu et al.[173] synthesized a 3D TiO_2@c-MoS_2 architecture which achieved an 82% FE_{CO} in aqueous electrolyte due to the strong interaction between

https://doi.org/10.1021/acsmaterialsau.1c00006
ACS Mater. Au 2021, 1, 6−36

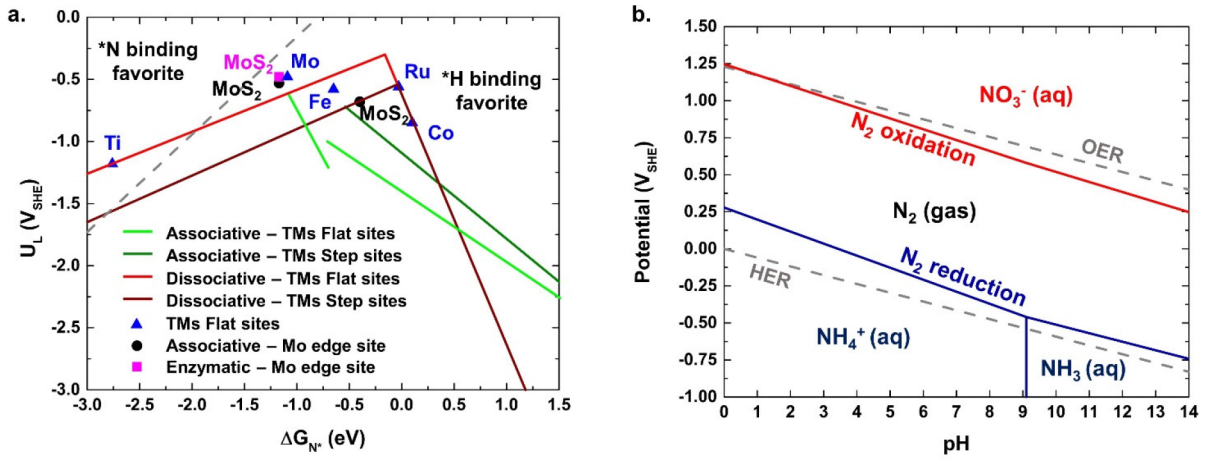

Figure 8. Overview of the NRR energy profile for transition metals catalyst and group VI TMD (represented by c-MoS_2) catalysts. (a) Simplified volcano plot for the NRR, according to the calculations proposed in ref 27. The associative (green traces) and dissociative (red traces) pathways for NRR are shown for transition metal flat sites and step sites. The gray dotted line in the plot delineates the energy region where binding of either N* or H* is favorable on the active site, showing how active catalysts for NRR tend to preferentially adsorb H* and, therefore, are prone to catalyze the HER. The black and magenta dots show the position in the volcano plot of c-MoS_2, according to the DFT-calculated energy profile for an associative reaction pathway (black square)[239,240] or an enzymatic reaction pathway (magenta square)[240] on the Mo-edge sites. The blue triangles show the position of representative transition metal catalysts' flat sites, as calculated by ref 27. (b) Pourbaix diagram for the NH_3/H_2O system,[210] showing how increasing the overpotential for the NRR leads concomitantly to a higher overpotential available for the HER. Considering the faster kinetics of the HER, the suppression of the parasitic hydrogen evolution represents a major factor to be considered when designing NRR catalysts.

the TiO_2 scaffold and c-MoS_2 catalysts. The interaction resulted in the formation of Ti−S bonds, which altered the electronic structure of the Mo sites by favoring CO_2 adsorption versus protons; when the TiO_2 scaffold was removed from the catalyst, CO_2 adsorption became unfavorable against the HER and the CO_2 reduction activity was lost. HER suppression can also be achieved by controlling the mass transport of reactants to the sites or by hindering hydrogen adsorption. Lv et al. effectively hindered HER by decorating a c-MoS_2 catalyst with an hydrophobic fluorosilane coating, which blocked the inflow of water and protons and boosted the selectivity toward CO_2R.[206] In this regard, the different mass transport mechanism and the chemical environment of a flow cell may lead to different CO_2 performances and a different hydrogen selectivity than H cells for transition metal chalcogenide-based electrocatalysts. Therefore, assessing the CO_2 reduction activity in this environment represents an attractive outlook for this family of catalysts: to the best of our knowledge, this strategy was pursued only by Salehi-Khojin and co-workers,[199] who registered only a 4.9% performance loss over 15 h for a CO_2 reduction flow cell and converted gaseous carbon dioxide to CO with a 93% selectivity at an applied cell potential of 2 V, although using a choline-based electrolyte.

5. ELECTROCHEMICAL NITROGEN FIXATION INTO AMMONIA

5.1. Reduction Reaction, Catalysts, and Analytical Problem

Production of ammonia (NH_3) is of great importance to human life and the global economy, from the aspects of food industry[207] and liquid fuel manipulation (production, storage, and transportation).[208] The Haber-Bosch process, invented in the early 1900s, enabled the massive industrial production of ammonia from atmosphere nitrogen gas (N_2) and hydrogen gas (H_2) through the reaction reported in eq 4. Through this process, ≈175 million tons of ammonia are produced annually accounting for a ≈70 billion USD market value. However, given the high triple N≡N bond energy (≈941 kJ mol^{-1}) of the dinitrogen molecule, a high temperature (>400 °C) is required to activate the reaction on iron-based catalysts to achieve a reasonably fast kinetics, and a high pressure (>150 bar) is needed to push the reaction equilibrium to final product.[207,209]

$$N_2 + 3H_2 \rightarrow 2NH_3 \quad (4)$$

$$N_2 + 8H^+ + 16\text{MgATP} + 8e^- \rightarrow 2NH_3 + H_2 + 16\text{MgATP} + 16\text{Pi} \quad (5)$$

$$N_2 + 6H^+ + 6e^- \rightarrow 2NH_3,\ E_0 = 0.092\ V_{NHE} \quad (6)$$

As a result, the Haber-Bosch process is very energy-intensive, consuming roughly 2% of the world's energy production.[207] Additionally, steam reforming of natural gas is coupled to this process to supply the required stoichiometric hydrogen, emitting greenhouse gases in the atmosphere (≈2 tons of CO_2 per tons of NH_3).[210] Moreover, the harsh reaction conditions of the Haber-Bosch process require large-scale and centralized facility, which further increases the capital cost and disables the on-site ammonia production in remote areas. Therefore, more sustainable approaches are needed for future ammonia manufacturing. An alternative method is inspired by a diazotrophic micro-organism, which naturally fixed the dinitrogen molecule into ammonia using an apt family of enzymes—nitrogenases—with metal-based catalytic cofactors (e.g., Fe−Mo, Fe−Fe). The enzymatic pathway is carried out at ambient temperature and pressure, utilizes protons (H^+) as the hydrogen source instead of H_2, and shows a 75% Faradaic efficiency (eq 5).[211] Although the yield of the enzymatic pathway is insufficient to meet the industrial ammonia demand, it indicates that electrochemical nitrogen fixation into ammonia (NRR, eq 6), on the other hand, may represent an alternative to the industrial process, allowing for a decentralized NH_3 production at ambient conditions, employing H^+/water as a carbon-neutral hydrogen source.[9,29]

https://doi.org/10.1021/acsmaterialsau.1c00006
ACS Mater. Au 2021, 1, 6−36

Leveraging the catalytic activity of the metal-based nitrogenase active site, various transition metal surfaces have been theoretically screened. Skúlason et al.[27] utilized DFT calculations to evaluate the NRR activity on different transition metals, assuming two main reaction pathways according to the stage where the triple N≡N bond is broken, namely, the dissociative mechanism wherein the N≡N bond is broken before protonation or associative mechanism otherwise. For the former mechanism, product desorption represents the potential determining step of the reaction; for the latter mechanism, instead, the critical and more energy-intensive reaction step is the initial activation of the adsorbed N_2, in which the triple N≡N bond is weakened and broken by the sequential protonation of the adsorbate. A volcano plot for the two pathways, of which a simplified version is shown in Figure 8a, was constructed to evaluate the performance of transition metals. Despite the high theoretical activity of certain metallic sites, the high overpotential (>0.45 V) required by the reaction—caused by the stable nature of N_2—and the utilization of water as the proton source cause three drawbacks that researchers are addressing:[9] the small ammonia yield, the low catalytic activity, and the predominance of the competing HER in aqueous environments. As shown by the Pourbaix diagram of NRR and HER reaction (Figure 8b), any decent overpotential shift of NRR can enter the HER region. An efficient catalyst for nitrogen fixation, therefore, has to be either extremely active to operate in the NRR/HER gap region or extremely selective toward the NRR with respect to the HER. In fact, the parasitic HER represents a serious problem affecting the performance of many metallic catalysts: hydrogen is preferentially adsorbed on metallic sites; therefore, it hinders N_2 adsorption and blocks NRR, pushing the selectivity toward the HER. This, coupled with the faster HER kinetics[212] than NRR and the high overpotential required by the latter reaction, drastically limits the final Faradaic efficiency toward NH_3. This problem is visualized in the volcano plots in Figure 8a, where the more active NRR catalysts, which lie on top of the volcanoes, are also in an energy region where adsorption of hydrogen is favorable with respect to nitrogen.

Two main research directions to improve the efficiency for NRR metallic catalysts can be outlined. The first aims at performing the electrochemical reaction in aprotic environments. Here, electrochemical setups utilizing a lithium catalytic mediator ("lithium-mediated" approaches) effectively improved the NH_3 Faradaic efficiency and product yield either by exploiting tetrahydrofuran (THF) and ethanol (EtOH) as the solvent and proton source[213−215] or by exploiting the stepwise cycling of electrolysis−nitridation−hydrolysis of Li in molten salt, dinitrogen gas, and water, respectively.[216] Alternatively, electrolytes where proton/water are supplied preferentially to the NRR thus limiting the HER have been employed; e.g., a remarkable NH_3 Faradaic efficiency of 60%[217] was achieved in an ionic liquid electrolyte with a nitrogen solubility higher than that of water. Despite the promising results, ionic liquid electrolytes are characterized by high diffusion resistance and inefficient proton supply, thus requiring further optimization. The second direction is focused instead on catalytic designs that suppress as much as possible the HER in aqueous electrolytes, wherein the proton source is ideal and more sustainable. A recent review by Qiu and collaborators[42] summarized the most pursued strategies to favor NRR by suppressing as much as possible hydrogen evolution, dividing them in "kinetic regulation" strategies where proton/electron accessibility to the active sites is limited[218−220] to slow down the fast kinetics of HER and favor NRR, "thermodynamic regulation", wherein the chemical equilibrium of HER is shifted to inhibit it, and "catalyst design" where the active sites of the catalyst are engineered to worsen the interaction energy with the HER intermediates, e.g., by synthesizing high-index facets of transition and noble metals[221,222] with higher NRR activity or by engineering the electronic structure and nanoscale organization of the catalyst.[223,224]

The low yield and selectivity of NRR catalysts even make ammonia detection a critical procedure from an experimental point of view in the framework of result validation, particularly given the ubiquitous exogenous ammonia contamination, found in a laboratory environment and instrumentation (e.g., glassware, upstream gas feed).[29,225,226] Considering that a shared set of experimental controls is unavailable and many currently reported catalysts (in particular, the ones for protic media) report different analyses and techniques for experimental controls, it is difficult to compare the NH_3 yield achieved by state-of-the-art catalysts.[227] Recent papers[29,226] proposed rigorous experimental controls (e.g., characterization under Ar, open circuit, etc.) for results validation, among which isotopic analysis with purified $^{15}N_2$ gas feed is becoming increasingly important and indispensable.[226] An ideal and convincing NRR data report should include multipoint quantitative isotope analysis[228] supplemented with pristine evaluation data of the gaseous NO_x and NH_3 species before and after purification.[229,230] Simonov and co-workers, in a recent perspective,[230] outlined a series of rigorous experimental methods and minimum performance criteria to be met by NRR studies, which represent an important guide for the development of efficient NRR electrocatalysts. According to the perspective, the reported NRR catalysts in protic media fail the control of the oxidation states of nitrogen species (N_2O, NO, NO_2, etc.) in the labeled $^{15}N_2$ gas for isotopic analysis.

In this research framework, our review discusses the theoretical activity and selectivity of group VI transition metal chalcogenides catalysts toward electrochemical NRR, focusing more on the feasibility of this class of materials as electrocatalysts instead of explicitly evaluate their rigor. Subsequently, we discuss promising design strategies and catalytic mechanisms that leverage on the chalcogenation of transition metal catalysts to improve the NRR activity.

5.2. Transition Metal Chalcogenide-Based Materials as NRR Electrocatalysts

The FeMo-based nitrogenase cluster site (e.g., $MoFe_7S_9N$) has been proposed and discussed, in a biomimetic approach, as a blueprint for the rational design of iron- and molybdenum-based electrocatalysts.[211] Recently, a Mo-doped FeS_2 catalyst was designed and showed a Faraday efficiency of 14.4% at −0.2 V_{RHE}.[231] Similarly, catalysts based on Fe-incorporated MoS_2 nanosheets achieved a good NRR performance, with an 18.8% FE and a normalized ammonia yield of 0.41 μmol cm^{-2} h^{-1} (8.63 μg mg_{cat}^{-1} h^{-1}) at −0.3 V_{RHE}[232] and an NH_3 FE of 31.6% and a normalized yield of 5.42 μmol cm^{-2} h^{-1} (36.1 mol g_{cat}^{-1} h^{-1}) at −0.2 V_{RHE}.[233] Multiphasic 1T/2H c-$MoSe_2$ nanosheets also showed a good NRR performance, with a maximum 6.03% FE at −0.5 V_{RHE} and a maximum ammonia yield of 19.9 μg mg_{cat}^{-1} h^{-1} at −0.6 V_{RHE},[234] while a c-$MoSe_2$ catalyst with a hollow nanosphere morphology exhibited a good ammonia FE of 14.2% at −0.1 V_{RHE} and a maximum

https://doi.org/10.1021/acsmaterialsau.1c00006
ACS Mater. Au 2021, 1, 6−36

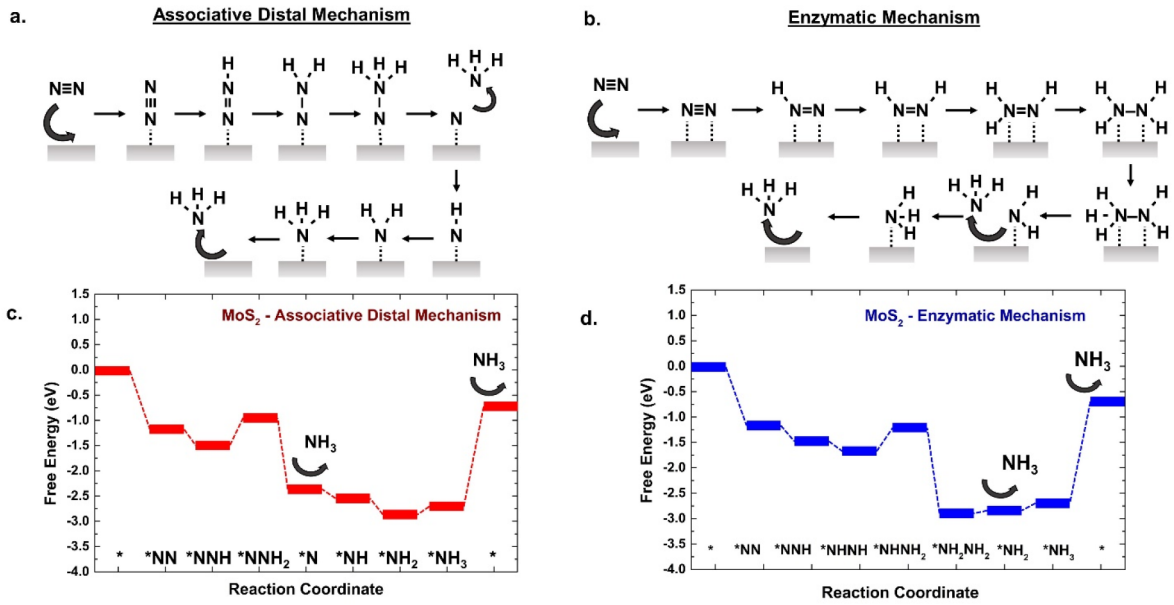

Figure 9. NRR mechanisms proposed to take place on the metallic edge sites of c-MoS_2. (a,b) Associative distal mechanism and enzymatic mechanism, respectively. (c,d) DFT-calculated energy profiles for the associative distal mechanism and enzymatic mechanism, respectively, on the active sites of c-MoS_2.[240] In the plot, the * denotes the adsorption site.

yield of 0.66 μmol cm^{-2} h^{-1} (11.2 μg mg_{cat}^{-1} h^{-1}) at −0.6 V_{RHE}.[235] Additionally, Fe-doped c-$MoTe_2$ was found to be active for NH_3 photoreduction to ammonia.[236]

Based on the similar composition to the metallic active center of nitrogenase enzymes,[237,238] group VI transition metal chalcogenides are expected to be active for the NRR, despite their high HER activity. First-principle calculations based on density functional theory confirmed that the edge sites of pure group VI transition metal sulfides are indeed active for the NRR,[239,240] while the chalcogen basal plane is inert.[239] While a broad generalization of various NRR mechanisms on metal catalysts has been established, the detailed reaction mechanisms by which the adsorbed N_2 is hydrogenated to NH_3 is still debated. For group VI transition metal chalcogenides, the DFT calculations of the free energy diagrams with the different mechanisms lead to varied and sometimes contrasting results[241] even on the same active site,[240,242,243] particularly given the fact that experimental validation data are still lacking.[29] Nevertheless, qualitative comparisons still play an important role in identifying the crucial reaction steps to be overcome through catalytic design and optimization. A schematic overview of the proposed reaction pathways on c-MoS_2 and of the corresponding DFT-calculated energy profiles is illustrated in Figure 9.

On c-TMDs, the nitrogen molecule adsorbs on the metallic edge sites with different possible configurations, while the adsorption on perfect chalcogen edges is unfavorable. Interestingly, the calculated most energetically favorable binding configuration is the bridge mode, where N_2 is coordinated by two metal atoms. Irrespective of the binding, the metal edges are characterized by an accumulation of charges (calculated by Bader charge analysis)[244] that are related to an electron transfer between metallic atoms and nitrogen, resulting in the formation of a N−metal bond that polarizes the N_2 molecule and activates (i.e., weakens) the N≡N bond upon adsorption.[239] The possible activation of the N≡N bond by polarization and charge transfer makes these metallic sites particularly appealing because, in principle, a smaller energetic input would be required for the reaction with respect to other catalysts with singly coordinated nitrogen atoms. After adsorption, the type of metal edge site determines the potential determining step (PDS) of the reaction and its thermodynamic free energy barrier, so that the catalytic activity of different transition metal sulfides can be compared. By this approach, Li et al.[240] showed that c-MoS_2 is more catalytically active than c-WS_2, as the free energy barrier of its PDS was 0.48 eV, whereas the one for the c-WS_2 was ≈0.98 eV, although c-WS_2 was proposed to suffer less from the competing HER. In fact, for c-WS_2, the adsorption of nitrogen is more energetically favorable than hydrogen, suppressing HER with better effectiveness than c-MoS_2, where instead N_2 and H adsorption is characterized by similar free energy and is equally favorable. In accordance with the thermodynamic considerations, the NRR activity of the c-MoS_2 edge sites has been experimentally confirmed by Zhang et al.,[239] who registered for c-MoS_2 nanosheets grown on carbon cloth by an hydrothermal method a Faradaic efficiency of 1.17%, a normalized ammonia yield of 0.291 μmol cm^{-2} h^{-1} at −0.5 V_{RHE}, and a 26 h stability under continuous operation. Such NRR activity even exists in an acidic environment where the impact of HER is supposed to be overwhelming.

In order to facilitate the critical N_2 adsorption/activation step and to limit the competing HER, Liu et al.[245] proposed a concept of tuning the electronic structure of the c-MoS_2 edge sites via an interaction with Li^+ ions from the electrolyte, in a "lithium-assisted" approach, effectively adjusting the adsorption energies of the reaction intermediates of NRR and HER. For the NRR in a 0.1 M Li_2SO_4 aqueous media, Li^+ ions form strong bonds with the chalcogen edges redistributing the charge on the metallic sites, resulting in a net positive charge on the Mo atoms and changing the adsorption energies (ΔG_{ads}) of both N_2* and H* species. The HER is thus limited by an unfavorable H* adsorption on S-edges (0.47 eV) and a too strong adsorption on Mo-edges (−0.72 eV), with respect to the ≈0 eV for both sites calculated without Li interaction. In this case, however, the Mo active sites might be over-saturated

https://doi.org/10.1021/acsmaterialsau.1c00006
ACS Mater. Au 2021, 1, 6−36

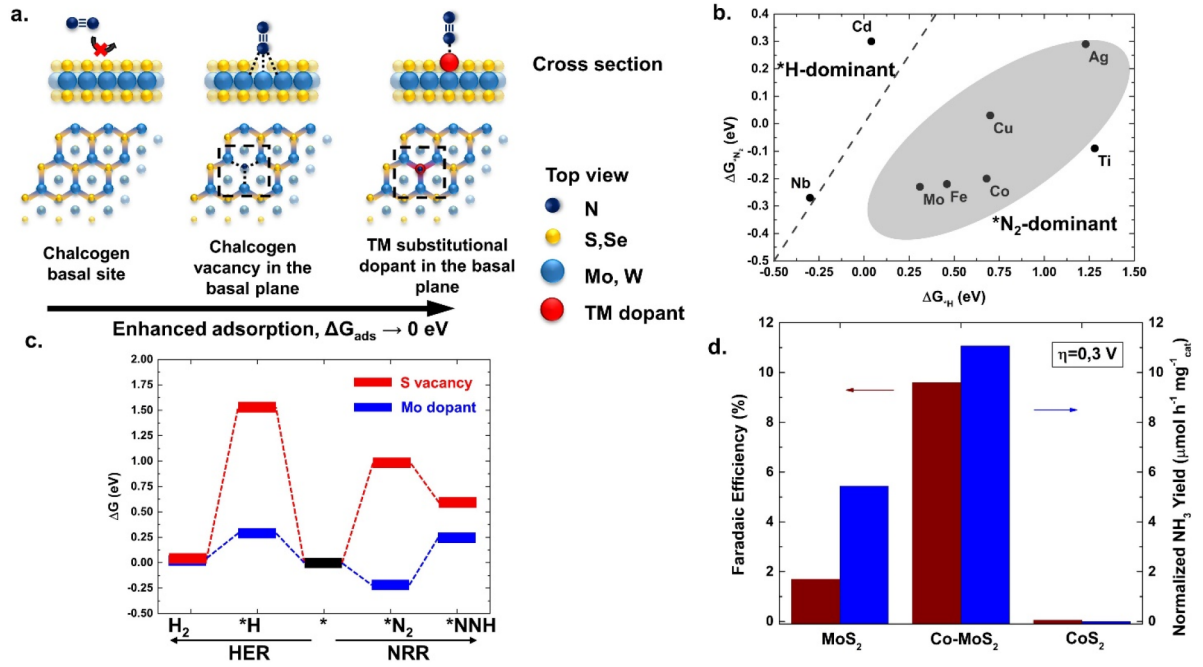

Figure 10. Overview of the NRR activity at the basal sites of group VI TMDs. (a) Schematic representation of the binding of N_2 on the pristine chalcogen basal atoms, on the chalcogen vacancies at the basal plane, and on substitutional transition metal (TM) dopants in the chalcogen vacancies. The N_2 binding mechanism on the basal vacancies, where adsorption occurs on the three exposed metal atoms, was proposed by ref 242 according to DFT calculations. (b) Effect of notable substitutional transition metal dopants in the basal plane of a c-MoS_2 catalyst on the competition between hydrogen and nitrogen adsorption. The majority of TM dopants favor the adsorption of nitrogen on the active site with respect to hydrogen. The gray shaded area represents the energy position, in terms of $\Delta G_{(*N_2)}$ and $\Delta G_{(*H)}$, of the majority of transition metal dopants.[154] (c) Binding energy of key intermediates for HER and NRR on a sulfur vacancy in the basal plane (red trace) and a Mo substitutional dopant in the chalcogen vacancy (blue trace) for the sulfur-containing basal plane of a "Janus" c-MoSeS catalyst.[154] (d) Experimental evidence of the NRR performance enhancement achieved due to the inclusion of a Co substitutional atom in a c-MoS_2 catalyst, showing an increase in both Faradaic efficiency and ammonia yield with respect to the undoped c-MoS_2 and c-CoS_2.[242]

by H* species that will block the adsorption of N_2 molecules, and a kinetic study on such competing adsorption can be helpful to understanding the performance enhancement. The adsorption of nitrogen on Mo-edges is also enhanced in the presence of Li^+ ions, with its ΔG_{ads} changing from −0.32 to −0.70 eV. Consequently, the Li−S interaction hinders adsorption of hydrogen on S-edges, while on Mo-edges, N_2* adsorption is energetically easier than the Mo-edges in the pristine (i.e., without Li−S interaction) c-MoS_2. Additionally, the protonation steps to form the N_xH_y* intermediates are more energetically favorable due to the presence of Li^+. As a result, at −0.2 V_{RHE}, an FE of 9.81% and a normalized yield of 25.483 μmol cm^{-2} h^{-1} (43.4 μg h^{-1} mg^{-1}_{cat}) were obtained, along with a 12 h stability under continuous reductive conditions. Another strategy for facilitating the N_2 adsorption step was shown by Zhang et al., who synthesized c-TMD QDs with a high percentage of 1T phase with high NRR activity.[131] The high density of active sites with unsaturated coordination and the abundance of chalcogen defects granted by the QD structure altered the electronic structure of the active sites, making the N_2 adsorption step spontaneous and exothermic—differently from the 2H polymorph. Additionally, the different electronic structure of the QD structure lowered the energy barriers of the NRR. The best performing catalyst, c-$MoSe_2$, was characterized by a maximum normalized yield of 1.997 μmol cm^{-2} h^{-1} (340 μg h^{-1} mg^{-1}_{cat}) and an 11% FE at −0.4 V_{RHE} in 0.5 M Na_2SO_4 aqueous electrolyte, although no NMR control experiments or NO_x analysis have been performed to rule out the possibility of forming NH_3 from reduction NO_x species during electrolysis.

To further increase the efficiency, one effective strategy is improving the electron transfer in NRR by coupling the catalyst to a conductive support or by doping the material. Wu and collaborators[243] showed the beneficial effect of this approach by employing a reduced graphene oxide (rGO) support for c-MoS_2 nanosheets. The supported catalyst achieved a normalized yield of 0.146 μmol cm^{-2} h^{-1} (24.82 μg h^{-1} mg^{-1}_{cat}) at −0.45 V_{RHE}, with an FE of 4.58% in a 0.1 M $LiClO_4$ aqueous electrolyte. Differently, the performance of the unsupported c-MoS_2 in the same conditions was worse, with an FE of 2.18% and a normalized yield of 0.05 μmol cm^{-2} h^{-1} (8.55 μg h^{-1} mg^{-1}_{cat}). The marked activity improvement was ascribed to the rGO support, which enhances the electron transfer and, by inducing an accumulation of excess electrons at the c-MoS_2 S-edge,[246] grants an easier N_2 adsorption at the active sites of the c-MoS_2 catalyst. Zhang and co-workers,[247] on the other hand, fabricated c-MoS_2 nanodots with a high surface area by a lyophilization/thermal treatment method and achieved a homogeneous catalytic site dispersion on the rGO substrate: the strong catalyst/support coupling was confirmed by the formation of C−S−C bridging bonds at the rGO/c-MoS_2 interface, which drastically increased the reaction kinetics by boosting the electron transfer rate, leading to promising results characterized by a maximum FE of 27.93%, a 10 h stability, and a normalized yield of 0.771 μmol cm^{-2} h^{-1} (16.41 μg h^{-1} mg^{-1}_{cat}) in a 0.1 M Na_2SO_4 aqueous electrolyte. However, no NMR control experiments or NO_x analysis are

https://doi.org/10.1021/acsmaterialsau.1c00006
ACS Mater. Au 2021, 1, 6−36

performed; therefore, it is not possible to rule out the formation of NH_3 from the reduction of NO_x species during electrolysis. By doping c-MoS_2 nanoflowers with N, instead, Chen and co-workers[248] registered a NH_3 normalized yield of 2.887 μmol cm^{-2} h^{-1} (69.82 μg h^{-1} mg^{-1}_{cat}) and an 11-fold increase in Faradaic efficiency with respect to an undoped MoS_2 (9.83% for N:c-MoS_2, 0.83% for undoped c-MoS_2) in a 0.1 M Na_2SO_4 aqueous electrolyte due to the enhanced electron transfer, the facilitated N_2 activation and successive hydrogenations, and the high density of unsaturated S sites granted by the doping process.

The chalcogen planes, inert in their pristine configuration, can be activated through the introduction of defects, such as vacancies that expose the underlying metal plane, or replacement of chalcogen atoms with metal ones. An overview of the NRR activity of the chalcogen sites is reported in Figure 10. The formation of defects in the chalcogen planes is common during the synthesis of c-TMDs, with defect density up to $\approx 10^{13}$ cm^{-2} when using PVD fabrication methods.[249] Jiang and co-workers[162] evaluated the activity of different defects on a c-WS_2 basal plane, namely, missing S atoms (V_S) or tungsten atoms replacing the basal sulfur (W_S). While at the V_S sites the exposed underlying W atoms have weak N_2 adsorption energy and do not activate the molecule, the W_S sites strongly adsorb N_2 and weaken the N≡N bond by orbital hybridization, change the coordination environment for the W atom, and facilitate electron transfer from metal to adsorbate. On these W_S sites, a limiting potential U_L down to −0.24 V_{RHE} is calculated, much smaller than other metallic catalysts, and the selectivity toward NRR is suggested to increase due to a stronger adsorption of N_2* than H*. In addition to c-WS_2, other works showed that the chalcogen vacancies on the c-MoS_2 basal plane efficiently bind N_2 and can catalyze NRR.[139,242,250] According to the DFT calculations by Lou's group,[242] the V_S sites expose three Mo atoms that participate in the binding and activation of N_2 through orbital hybridization and electron transfer to the adsorbate (Figure 10a). However, the strong interaction forces between adsorbate and three Mo markedly modify the intermediates' free energy, up to 1.62 eV required for the potential determining step. Such strong interactions between adsorbate and adsorption sites resulted in a suboptimal activity for the basal planes of synthesized c-MoS_2 with high V_S defect density, only achieving an FE of 1.7% at −0.3 V_{RHE}. To reduce this thermodynamic energetic barrier, they substituted the exposed Mo with Co atoms: the lattice and electronic structure distortion induced by the Co dopant changed the N_2 binding configuration from three Mo atoms to one Mo, diminishing the free energy required by the PDS to 0.59 eV, resulting in an enhanced catalytic activity. Experimentally, a ≈10% FE was obtained at −0.3 V_{RHE}, with a roughly 6-fold increase from the undoped, defective c-MoS_2, as shown in Figure 10d. The functionality of the defective sites was further proved by Sun and collaborators,[139] who synthesized a defect-rich c-MoS_2 nanoflower architecture that reached an FE of 8.3% and a normalized NH_3 yield of 0.688 μmol cm^{-2} h^{-1} (29.98 μg h^{-1} mg^{-1}_{cat}) at −0.4 V_{RHE}, with an approximate 4-fold increase with respect to a defect-free c-MoS_2 catalyst, due to the better stabilization of N_2 on two Mo atoms on the rim of defects and to the strong interaction with the adsorbate of the defective Mo sites. Other DFT calculation also indicates that boron-substituted h-MoS_2 can be a potential NRR catalyst with an optimized energy barrier of 0.46 eV.[241] The basal chalcogen vacancies can also activate the c-MoS_2 surface as a cocatalyst for NRR, as demonstrated by MacFarlane's group:[41] they designed a catalytic architecture where the hydrogenation of N_2 and its intermediates is favored by depositing amorphous Ru nanoparticles on a semiconducting c-MoS_2 basal plane in the presence of S vacancies. The sulfur vacancies were claimed to adsorb H^+ from the electrolyte to provide the six proton-coupled electron transfers for NRR, wherein the as-formed hydrogen H* is transferred to the adsorbed N_2 or intermediates on the adjacent Ru nanoparticles. Based on this catalytic mechanism, it was demonstrated that an FE of 12.2% and an NH_3 yield of 0.241 μmol cm^{-2} h^{-1} at −0.15 V_{RHE} was achieved at room temperature with an enhanced performance at 60 °C.

The activation of the basal plane via defects opens up a wide design space for NRR catalysts based on c-TMDs, where the reaction activity can be optimized by tuning the structure of the transition metal chalcogenide and of the species of substituting metal at the vacancy site (Figure 10b,c). Indeed, several works have screened a variety of metals as substitutional defects on the basal plane of molybdenum sulfide, tungsten sulfide, and of a "Janus" phase c-MoSeS. For c-MoS_2, Guo et al.[251] proposed substitutional Sc, Ti, Zr, and Hf dopants on the basal plane as promising active sites: these metals alter the electronic structure of the basal plane and, due to an accumulation of charges between the substitutional metal and Mo, are able to strongly adsorb N_2 polarizing the triple N≡N bond, resulting in desired energies for the reaction PDS smaller than 0.70 eV. Regarding c-WS_2, Huang and co-workers[252] calculated an enhanced NRR activity for Ni atoms embedded into the basal plane: similarly to the c-MoS_2 case, an electron transfer between N_2 and Ni site facilitates nitrogen adsorption and triple bond activation. This changes the energy profile of the reaction: after the first endergonic hydrogenation step (0.88 eV), the following hydrogenations are exergonic. On the other hand, the desorption of reaction byproducts (e.g., N_2H_4) has high energy barrier and requires the application of an high overpotential. Finally, the case of the "Janus" phase c-MoSeS, where the molybdenum layer is sandwiched between one layer composed of selenium atoms and the other one of sulfur atoms, is considered. Li and collaborators[154] identified Mo as the most promising metal site at the chalcogen vacancies on both c-MoSeS basal planes, as it is the metallic site where the NNH* intermediate—crucial for the successive hydrogenations—is better stabilized. Again, the electronic structure modifications induced by the substitutional metal site, represented by the introduction of defective states near the Fermi level, translate into an enhanced electrical conductivity and a charge transfer between metal and adsorbate. For both basal planes, the NRR is proposed to be more energetically favorable than the HER, due to the N* adsorption being stronger than H* absorption, as visualized in Figure 10c, and the calculated limiting potentials for the Mo atom at the S and Se vacancies are −0.49 and −0.63 V, respectively, showing the theoretical feasibility of this catalytic architecture. A slightly earlier computational work[253] also revealed that a single Mo atom was the best substitution on the S-vacancy-rich c-MoS_2 monolayer, wherein the onset potential was found to be −0.53 V and the hydrogenation of the adsorbed N_2* to N_2H* was the potential-determining step. However, later experimental work[254] found no NRR activity of this catalyst in aqueous media (0.1 M Li_2SO_4 with pH 3) but very limited activity in

https://doi.org/10.1021/acsmaterialsau.1c00006
ACS Mater. Au 2021, 1, 6−36

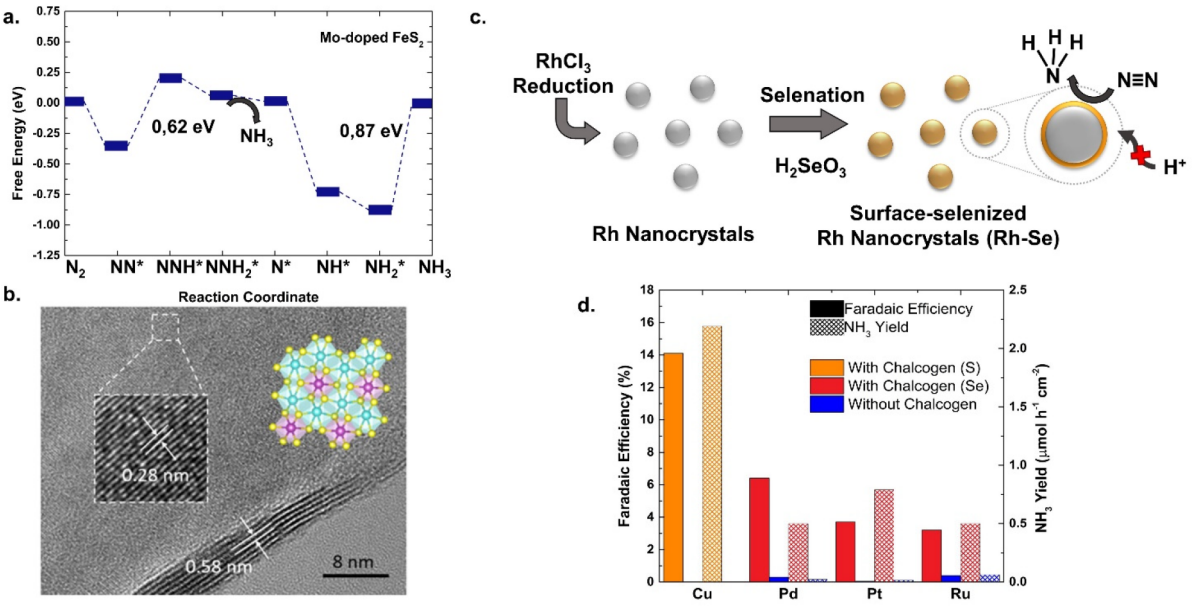

Figure 11. Chalcogenation strategies to improve the activity of NRR electrocatalysts. (a) DFT-calculated NRR energy profile for a Mo-doped FeS_2 catalyst. The incorporation of the Mo dopant favors the adsorption of N_2 and the activation of the adsorbed molecule, whereas the FeS_2 catalyst suppresses the competing HER. The design of the catalyst active site mimics the composition of the FeMo-containing active site of the nitrogenase enzyme.[231] (b) TEM micrograph of Re_2MnS_6 crystal-based NRR electrocatalyst. The inclusion of Mn atoms in the structure creates a dual-metal active site that requires less energy to activate the adsorbed N_2 molecule and protonates the successive reaction intermediates more easily. Reproduced from ref 257. Copyright 2020 American Chemical Society. (c) Schematized surface selenation process for Rh nanocrystals NRR catalysts, proposed in ref 258. The incorporation of surface chalcogen decreases the activation energy for the NRR and at the same time suppresses the competing HER. (d) NRR performance enhancement obtained with transition metal and noble metal catalysts when chalcogen is incorporated on the surface of the catalyst. A surface selenation drastically improves the NRR performance of Pd, Pt, and Ru nanocrystal catalysts,[258] whereas the presence of S on a Cu-based catalyst[119] forms a hydrogen bond between the S atom of the catalyst and the adsorbed N−H, thus stabilizing the reaction intermediate and improving the reaction energy profile.

ionic liquid ([C_4mpyr][eFAP]) with possible strong surface blockage of produced NH_3/NH_4^+.

Another strategy for activating the basal plane has been proposed by Azofra et al.,[255] taking direct inspiration from the FeMo-based nitrogenase cluster site: according to DFT calculations, when dispersed on top of a c-MoS_2 basal plane, Fe atoms efficiently catalyze the NRR while limiting the selectivity for the competing HER and also for the CO_2R. Fe, by strongly binding S and by interacting with the electronic structure of c-MoS_2, acquires a net positive charge and introduces new states near the Fermi level, facilitating the adsorption of negative entities from molecules like N_2 and activating the N≡N bond, decreasing the energetic barrier of this first step. However, the two successive hydrogenations to obtain NNH* and NNH_2* are characterized by high energetic barriers, requiring a high overpotential to overcome. Mu and co-workers[256] experimentally tested the proposed catalytic architecture by synthesizing a Fe nanodot-decorated c-MoS_2, which achieved an FE of 10.8%, a normalized NH_3 yield of 0.774 μmol cm^{-2} h^{-1} (12.5 μg $h^{-1}cm^{-2}$) at −0.1 V_{RHE}, and a 48 h stability after prolonged operation. The remarkable performance stems from the strong electronic interaction between Fe and MoS_2, which through a charge transfer mechanism from Fe to MoS_2 allows for an efficient N_2 adsorption. Recently,[231] a similar Mo-doped FeS_2 catalyst was designed and represented a more closed composition to MoFe cofactors in natural nitrogenase, showing a Faraday efficiency of 14.4% at −0.2 V_{RHE} and a NH_3 yield rate of 26.15 μg h^{-1} mg^{-1}. DFT calculation suggested that Mo^{4+} ions substituting the lattice Fe atom act as the catalytic sites largely improved the adsorption and activation of N_2 molecule, and speeded up the NRR process, as visualized by the reaction energy diagram shown in Figure 11a. Moreover, an atomic-hybridized Re_2MnS_6 ultrathin nanosheet (Figure 11b) was designed to take the advantage of Mn−Re dual-metal sites.[257] The substitution of Mn sites in an ordered pattern resulted in a structural change and introduced nonbonding semimetal states, wherein the energy barrier for rate-determining step was significantly reduced via an optimization of reaction energy landscape. Consequently, the resulting yield and Faradaic efficiency toward NH_3 are ≈0.892 μmol cm^{-2} h^{-1} (3.8 μg h^{-1} mg^{-1}) and ≈17.4%, respectively, showing a 6.6-fold increase as compared to that of ReS_2 counterpart.

More generally, a surface chalcogenation approach, the schematics of which is reported in Figure 11c, was proposed to further expand and demonstrate the functionality of transition metal chalcogenides.[258] The optimized Rh−Se nanocrystals showed an ammonia yield of ≈1.044 μmol cm^{-2} h^{-1} (175.6 mg h^{-1} g^{-1}) and a Faradaic efficiency of ≈13.3% in an 18 h stability test, showing a 16-fold increase comparing to pure Rh nanocrystals. DFT calculation suggested that the reduced valence state of Rh site by selenation accounted for improved p−d coupled electron transfer, which promoted the protonation and bond cleavage of a dinitrogen molecule. In addition, the interface strain effect of such a core@shell structure further boosted catalytic and electronic activities of Rh−Se nanocrystals. Further, the surface chalcogenation modification was applied to Pt, Pd, and Ru, wherein a significant increase was observed for both ammonia yield and Faradaic efficiency (Figure 11d). The critical role of chalcogen atoms was further

https://doi.org/10.1021/acsmaterialsau.1c00006
ACS Mater. Au 2021, 1, 6−36

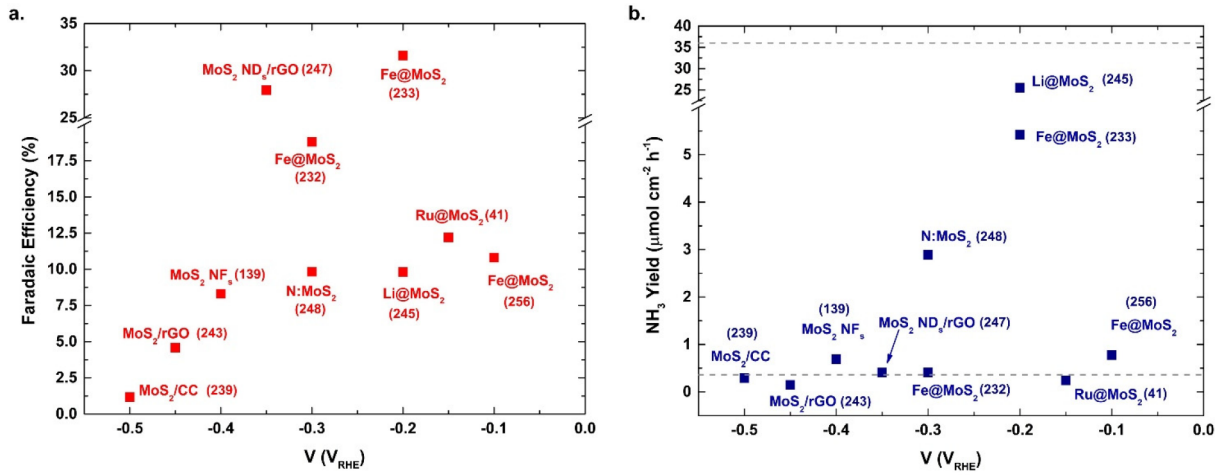

Figure 12. NRR performance and morphological/chemical characteristics of c-MoS_2-based NRR catalysts. (a) Maximum NH_3 Faradaic efficiency and (b) maximum normalized yield as a function of the applied potential, measured in V_{RHE}. The reported catalysts include Fe-decorated MoS_2 on carbon cloth (Fe@MoS_2),[256] Ru-decorated MoS_2 on carbon fiber paper (Ru@MoS_2),[41] lithium-assisted MoS_2 on carbon cloth (Li-MoS_2),[245] MoS_2 with protusion-shaped Fe deposited on the basal plane (Fe@MoS_2),[233] vacancy-rich N-doped MoS_2 (N:MoS_2),[248] MoS_2 nanosheets with atomically dispersed Fe atoms (Fe@MoS_2),[232] MoS_2 nanodots supported on reduced graphene oxide (MoS_2/rGO),[247] defect-rich MoS_2 nanoflower on carbon paper (MoS_2 NF),[139] MoS_2 nanosheets on reduced graphene oxide (MoS_2/rGO),[243] and MoS_2 on carbon cloth (MoS_2/CC).[239] The gray dashed lines in the normalized yield plot represent the NH_3 yield region of sufficient ammonia production for plausible and reliable production detection, indicated by ref 230. The proposed range is between 0.1 and 10 nmol cm^{-2} s^{-1}, i.e., between 0.36 and 36 μmol cm^{-2} h^{-1}.

highlighted by Kim et al. in assessing the NRR performance of copper sulfide catalysts with different Cu/S ratios.[119] The catalyst with the optimized stoichiometry, $Cu_{1.81}S$, achieved a maximum ammonia yield of 2.19 μmol h^{-1} cm^{-2} (37.3 μg h^{-1} mg^{-1}) and an FE of 14.1% at −0.1 V_{RHE}. Here, the chalcogen sites were determined to be critical in improving the energy profile of the reaction by acting as proton donors for the first protonation of N_2 (the potential determining step) and drastically reducing the limiting potential of this step to 1.2 from 2.5 eV on bare Cu, where the protonation is not mediated by the chalcogen atom. Through this reaction mechanism, which resembles that of the nitrogenase enzyme active center, the N_2H* intermediate formed after the first protonation is effectively stabilized to the chalcogen atom through a hydrogen bond. Similarly, a regenerative, N-doped carbon-supported Cu_9S_5 catalyst showed an NRR performance characterized by an ammonia yield of 0.63 μmol cm^{-2} h^{-1} and 35% FE at −0.5 V_{RHE} in a 0.5 M Na_2SO_4 aqueous electrolyte.[259]

The NRR performance of the different c-TMD-based catalysts are grouped according to ammonia selectivity and normalized yield (expressed in μmol h^{-1} cm^{-2}) in Figure 12, along with representative catalytic systems previously discussed, while Table 1 summarizes the control experiments performed to confirm the production of ammonia via N_2 electroreduction for the same catalysts. While the similar structure to nitrogenase enzymes makes c-TMDs a promising class of materials for the development of more efficient NRR catalysts, the competition of the parasitic HER in aqueous electrolytes represents a serious hurdle, exacerbating the selectivity problem that also affects CO_2 reduction catalysis due to the small ammonia yields achieved in low-temperature devices. Considering the high activity of the c-TMD edge sites for the HER, much effort should be focused on the inhibition of proton adsorption on the edges of the material and on the suppression of the HER activity, so that the selectivity of these materials can be effectively pushed toward the synthesis of ammonia. In the future, well-designed gas diffusion electrode is an indispensable strategy to kinetically boost the N_2 adsorption on c-TMD catalyst surface for a more reliable analytic quantification of ammonia yield.

Table 1. Overview of the Control Experiments Performed on the MoS_2-Based NRR Electrocatalysts Shown in Figure 12 to Assess the Effective Production of NH_3 from the Gaseous Nitrogen Feed Along with the Ammonia Yield Indicated

catalyst	NH_3 yield (nmol cm^{-2} s^{-1})	^{15}N-labeled N_2	NO_x control in gas	ref
Ru@MoS_2	0.07	yes	no	41
Fe@MoS_2	0.11	yes	no	232
Fe@MoS_2	1.51	yes	no	233
MoS_2/CC	0.08	no	no	239
MoS_2/rGO	0.04	yes	no	243
Li-MoS_2	7.08	yes	no	245
MoS_2/rGO	0.11	no	no	247
N:MoS_2	0.80	no	no	248
MoS_2 NF	0.19	yes	no	139
Fe@MoS_2	0.22	yes	no	256

6. CONCLUSIONS AND OUTLOOK

Group VI transition metal chalcogenides have been the focus of increasing research interest due to their high electrocatalytic activity for different reduction reactions aimed at the synthesis of value-added chemicals beyond H_2, like hydrocarbons and ammonia, with the future goal of economic competitiveness with currently employed energy-intensive processes. In this review, the morphological and electrochemical properties of these materials have been discussed and the relationship between structure and electrocatalytic characteristics has been underlined, evaluating how it is possible to tailor the composition, the active site nature and architecture of the catalyst to the desired application like CO_2R or NRR. For the

https://doi.org/10.1021/acsmaterialsau.1c00006
ACS Mater. Au 2021, 1, 6−36

electrochemical reactions that we discussed, recent efforts in the identification and description of the catalytic active sites have been reported, along with recent experimental work that, by leveraging on the characteristics of the active sites, showed the remarkable activity of this class of materials.

The experience acquired by the scientific community through the application of group VI transition metal chalcogenides -based materials for HER electrocatalysis and the design rules that have been developed for this technology are an incredibly useful tool to guide the synthesis of efficient catalysts of the same family for other, more complex reductions, such as CO_2R or NRR. Indeed, due to the flexible nature of the active sites which can coordinate different reactants with an optimal energy, the same strategies employed to optimize the interaction with hydrogen can be translated for the interaction with CO_2 and N_2, with similar enhancement effects. Nevertheless, the dichotomy between activity and selectivity is the major hurdle that needs to be addressed, in the framework of a widespread implementation of group VI transition metal chalcogenides for other reduction reactions: the energy profile and the kinetics of HER are more favorite than CO_2R and NRR and hindering (or limiting) the adsorption of protons is critical to steer the selectivity toward the desired reaction.

As an outlook, future research on the electrocatalytic application of group VI transition metal chalcogenides should focus on distinct aspects according to the reaction to be catalyzed, i.e., the CO_2R or the NRR. For the former, the design of well-engineered c-TMD materials holds promise for the high-efficiency electrolysis of CO_2 to CO, as long as the competing HER is limited by hindering proton adsorption. Indeed, we have described how, when the HER is suppressed with appropriate additives (e.g., ionic liquid electrolytes) or by acting on the mass transfer of hydrogen (e.g., by employing hydrophobic coatings or a gaseous CO_2 feed in a flow cell), c-TMDs showed an impressive performance in reducing CO_2 to CO with higher activity than silver and gold, the state-of-the-art catalyst for this reaction pathway, whereas synthesis of more complex reduction products is hindered by kinetic limitations affecting the CO adsorbate. In aqueous electrolytes, instead, the facile kinetics of the HER completely switches the selectivity toward hydrogen production, hindering the CO_2 reduction. In this framework, more attention should focus on testing TMD-based catalysts in a flow cell environment, where the gaseous CO_2 flow, the different electrochemical environment than an H-cell, and the different mass transfer to the cathode may lead to a higher selectivity for C products than what registered in aqueous electrolytes. Regarding the latter reaction, the electrochemical nitrogen reduction to ammonia, group VI transition metal chalcogenides suffer (along with the other studied catalysts) from the sluggish kinetics of the NRR and the competing HER in aqueous electrolytes. Despite this limitation, the similarity between this class of materials and the active sites of nitrogenase enzymes paves the way for a nature-mimicking approach for catalyst design that resulted in good selectivity for the NRR and moderate product yields and holds promise for an enhanced catalytic performance. Indeed, recent works suggested how the nature-mimicking structure of the catalyst may at the same time limit proton adsorption and favor the interaction with nitrogen. Thanks to their peculiar structural characteristics and the flexibility of their active sites, group VI transition metal chalcogenides can be a powerful platform both for understanding the basic reaction mechanisms for the synthesis of value-added chemicals and for designing nonprecious catalysts that may find application in future commercial devices.

AUTHOR INFORMATION

Corresponding Author

Fabio Di Fonzo − *Center for Nano Science and Technology, Istituto Italiano di Tecnologia (IIT@Polimi), 20133 Milano, Italy*; orcid.org/0000-0001-5581-7948; Email: fabio.difonzo@iit.it

Authors

Giorgio Giuffredi − *Center for Nano Science and Technology, Istituto Italiano di Tecnologia (IIT@Polimi), 20133 Milano, Italy; Department of Energy, Politecnico di Milano, 20156 Milano, Italy*; orcid.org/0000-0002-7342-8548

Tristan Asset − *Department of Chemical & Biomolecular Engineering and National Fuel Cell Research Center, University of California, Irvine, California 92697-2580, United States*

Yuanchao Liu − *Department of Chemical & Biomolecular Engineering and National Fuel Cell Research Center, University of California, Irvine, California 92697-2580, United States*; orcid.org/0000-0002-3669-8071

Plamen Atanassov − *Department of Chemical & Biomolecular Engineering and National Fuel Cell Research Center, University of California, Irvine, California 92697-2580, United States*; orcid.org/0000-0003-2996-472X

Complete contact information is available at: https://pubs.acs.org/10.1021/acsmaterialsau.1c00006

Author Contributions

The manuscript was written through contributions of all authors.

Notes

The authors declare no competing financial interest.

ACKNOWLEDGMENTS

The component of this work performed at UCI was supported by a subaward from Sandia National Laboratories from a U.S. DOE award (DE-LC-000L059): "Synthesis, Modeling and Kinetics of Rationally Designed Defects and Substitutions in 2D Materials" (Dr. S. Chou, PI).

VOCABULARY

scaling relations: mathematical linear relations that relate the binding energy of the first three CO_2 reduction intermediates, i.e., COOH*, CO*, CHO*; according to these relations, any variation in binding energy of one of the intermediates linearly affect the binding energy of the other two intermediates; **defective sites**: active sites in the material that are derived from the presence of localized, point-defects such as vacancies, heteroatoms, in the otherwise periodic structure of the (crystalline) material; **multiscale design**: a design process for electrocatalysts that aims at tackling both the nanoscale structural and electronic properties, as well as the mesoscale morphological/compositional features, with the aim of maximizing the catalytic activity for the desired reaction; **flexible active sites**: active sites in an electrocatalytic system that can efficiently catalyze different reactions and that can be controlled and tuned by the designer toward a specific

https://doi.org/10.1021/acsmaterialsau.1c00006
ACS Mater. Au 2021, 1, 6−36

application; **energy vectors**: chemicals (usually liquids or gases) that, being synthesized exploiting an electrical energy input, can store this electrical energy in their chemical bonds; in this way, they enable the transfer of energy in time and space, so that it can be used far from—and at a later moment—its point of generation

REFERENCES

(1) European Commission. *Strategic Energy Technology Plan*, 2017; DOI: 10.2777/48982.

(2) Cambridge Core. *Climate Change 2014: Mitigation of Climate Change*, 2014; DOI: 10.1017/CBO9781107415416.

(3) Ortiz Cebolla, R.; Navas, C. Supporting Hydrogen Technologies Deployment in EU Regions and Member States: The Smart Specialisation Platform on Energy (S3PEnergy). *Int. J. Hydrogen Energy* **2019**, *44*, 19067−19079.

(4) de Levie, R. The Electrolysis of Water. *J. Electroanal. Chem.* **1999**, *476* (1), 92−93.

(5) Peterson, A. A.; Abild-Pedersen, F.; Studt, F.; Rossmeisl, J.; Nørskov, J. K. How Copper Catalyzes the Electroreduction of Carbon Dioxide into Hydrocarbon Fuels. *Energy Environ. Sci.* **2010**, *3* (9), 1311.

(6) Hernández, S.; Amin Farkhondehfal, M.; Sastre, F.; Makkee, M.; Saracco, G.; Russo, N. Syngas Production from Electrochemical Reduction of CO2: Current Status and Prospective Implementation. *Green Chem.* **2017**, *19* (10), 2326−2346.

(7) Agarwal, A. S.; Zhai, Y.; Hill, D.; Sridhar, N. The Electrochemical Reduction of Carbon Dioxide to Formate/Formic Acid: Engineering and Economic Feasibility. *ChemSusChem* **2011**, *4* (9), 1301−1310.

(8) Verma, S.; Kim, B.; Jhong, H. R. M.; Ma, S.; Kenis, P. J. A. A Gross-Margin Model for Defining Technoeconomic Benchmarks in the Electroreduction of CO2. *ChemSusChem* **2016**, *9* (15), 1972−1979.

(9) Deng, J.; Iñiguez, J. A.; Liu, C. Electrocatalytic Nitrogen Reduction at Low Temperature. *Joule* **2018**, *2* (5), 846−856.

(10) Carmo, M.; Fritz, D. L.; Mergel, J.; Stolten, D. A Comprehensive Review on PEM Water Electrolysis. *Int. J. Hydrogen Energy* **2013**, *38* (12), 4901−4934.

(11) Vesborg, P. C. K.; Seger, B.; Chorkendorff, I. Recent Development in Hydrogen Evolution Reaction Catalysts and Their Practical Implementation. *J. Phys. Chem. Lett.* **2015**, *6* (6), 951−957.

(12) Du, P.; Eisenberg, R. Catalysts Made of Earth-Abundant Elements (Co, Ni, Fe) for Water Splitting: Recent Progress and Future Challenges. *Energy Environ. Sci.* **2012**, *5* (3), 6012−6021.

(13) Roger, I.; Shipman, M. A.; Symes, M. D. Earth-Abundant Catalysts for Electrochemical and Photoelectrochemical Water Splitting. *Nat. Rev. Chem.* **2017**, *1*, 0003.

(14) Zhong, Y.; Xia, X. H.; Shi, F.; Zhan, J. Y.; Tu, J. P.; Fan, H. J. Transition Metal Carbides and Nitrides in Energy Storage and Conversion. *Adv. Sci.* **2016**, *3* (5), 1500286.

(15) Yin, J.; Fan, Q.; Li, Y.; Cheng, F.; Zhou, P.; Xi, P.; Sun, S. Ni-C-N Nanosheets as Catalyst for Hydrogen Evolution Reaction. *J. Am. Chem. Soc.* **2016**, *138* (44), 14546−14549.

(16) Handoko, A. D.; Fredrickson, K. D.; Anasori, B.; Convey, K. W.; Johnson, L. R.; Gogotsi, Y.; Vojvodic, A.; Seh, Z. W. Tuning the Basal Plane Functionalization of Two-Dimensional Metal Carbides (MXenes) to Control Hydrogen Evolution Activity. *ACS Appl. Energy Mater.* **2018**, *1* (1), 173−180.

(17) Gao, Q.; Zhang, W.; Shi, Z.; Yang, L.; Tang, Y. Structural Design and Electronic Modulation of Transition-Metal-Carbide Electrocatalysts toward Efficient Hydrogen Evolution. *Adv. Mater.* **2019**, *31* (2), 1802880.

(18) Du, H.; Kong, R. M.; Guo, X.; Qu, F.; Li, J. Recent Progress in Transition Metal Phosphides with Enhanced Electrocatalysis for Hydrogen Evolution. *Nanoscale* **2018**, *10* (46), 21617−21624.

(19) Liu, K. H.; Zhong, H. X.; Li, S. J.; Duan, Y. X.; Shi, M. M.; Zhang, X. B.; Yan, J. M.; Jiang, Q. Advanced Catalysts for Sustainable Hydrogen Generation and Storage via Hydrogen Evolution and Carbon Dioxide/Nitrogen Reduction Reactions. *Prog. Mater. Sci.* **2018**, *92*, 64−111.

(20) Duan, X.; Xu, J.; Wei, Z.; Ma, J.; Guo, S.; Liu, H.; Dou, S. Atomically Thin Transition-Metal Dichalcogenides for Electrocatalysis and Energy Storage. *Small Methods* **2017**, *1* (11), 1700156.

(21) Zhou, W.; Jia, J.; Lu, J.; Yang, L.; Hou, D.; Li, G.; Chen, S. Recent Developments of Carbon-Based Electrocatalysts for Hydrogen Evolution Reaction. *Nano Energy* **2016**, *28*, 29−43.

(22) Zhang, L.; Xiao, J.; Wang, H.; Shao, M. Carbon-Based Electrocatalysts for Hydrogen and Oxygen Evolution Reactions. *ACS Catal.* **2017**, *7* (11), 7855−7865.

(23) Higgins, D.; Hahn, C.; Xiang, C.; Jaramillo, T. F.; Weber, A. Z. Gas-Diffusion Electrodes for Carbon Dioxide Reduction: A New Paradigm. *ACS Energy Lett.* **2019**, *4* (1), 317−324.

(24) Kibria, M. G.; Dinh, C.-T.; Seifitokaldani, A.; De Luna, P.; Burdyny, T.; Quintero-Bermudez, R.; Ross, M. B.; Bushuyev, O. S.; García de Arquer, F. P.; Yang, P.; Sinton, D.; Sargent, E. H. A Surface Reconstruction Route to High Productivity and Selectivity in CO2 Electroreduction toward C2+ Hydrocarbons. *Adv. Mater.* **2018**, *30*, 1804867.

(25) Zhuang, T.-T.; Pang, Y.; Liang, Z.-Q.; Wang, Z.; Li, Y.; Tan, C.-S.; Li, J.; Dinh, C. T.; De Luna, P.; Hsieh, P.-L.; Burdyny, T.; Li, H.-H.; Liu, M.; Wang, Y.; Li, F.; Proppe, A.; Johnston, A.; Nam, D.-H.; Wu, Z.-Y.; Zheng, Y.-R.; Ip, A. H.; Tan, H.; Chen, L.-J.; Yu, S.-H.; Kelley, S. O.; Sinton, D.; Sargent, E. H. Copper Nanocavities Confine Intermediates for Efficient Electrosynthesis of C3 Alcohol Fuels from Carbon Monoxide. *Nat. Catal.* **2018**, *1*, 946.

(26) Pander, J. E.; Ren, D.; Huang, Y.; Loo, N. W. X.; Hong, S. H. L.; Yeo, B. S. Understanding the Heterogeneous Electrocatalytic Reduction of Carbon Dioxide on Oxide-Derived Catalysts. *ChemElectroChem* **2018**, *5* (2), 219−237.

(27) Skúlason, E.; Bligaard, T.; Gudmundsdóttir, S.; Studt, F.; Rossmeisl, J.; Abild-Pedersen, F.; Vegge, T.; Jónsson, H.; Nørskov, J. K. A Theoretical Evaluation of Possible Transition Metal Electro-Catalysts for N2 Reduction. *Phys. Chem. Chem. Phys.* **2012**, *14* (3), 1235−1245.

(28) Rostamikia, G.; Maheshwari, S.; Janik, M. J. Elementary Kinetics of Nitrogen Electroreduction to Ammonia on Late Transition Metals. *Catal. Sci. Technol.* **2019**, *9* (1), 174−181.

(29) Suryanto, B. H. R.; Du, H. L.; Wang, D.; Chen, J.; Simonov, A. N.; MacFarlane, D. R. Challenges and Prospects in the Catalysis of Electroreduction of Nitrogen to Ammonia. *Nat. Catal.* **2019**, *2* (4), 290−296.

(30) Laursen, A. B.; Kegnæs, S.; Dahl, S.; Chorkendorff, I. Molybdenum Sulfides —Efficient and Viable Materials for Electro - and Photoelectrocatalytic Hydrogen Evolution. *Energy Environ. Sci.* **2012**, *5* (2), 5577−5591.

(31) Chhowalla, M.; Shin, H. S.; Eda, G.; Li, L. J.; Loh, K. P.; Zhang, H. The Chemistry of Two-Dimensional Layered Transition Metal Dichalcogenide Nanosheets. *Nat. Chem.* **2013**, *5* (4), 263−275.

(32) Hinnemann, B.; Moses, P. G.; Bonde, J.; Jørgensen, K. P.; Nielsen, J. H.; Horch, S.; Chorkendorff, I.; Nørskov, J. K. Biomimetic Hydrogen Evolution: MoS 2 Nanoparticles as Catalyst for Hydrogen Evolution. *J. Am. Chem. Soc.* **2005**, *127* (15), 5308−5309.

(33) Zhang, K.; Li, Y.; Deng, S.; Shen, S.; Zhang, Y.; Pan, G.; Xiong, Q.; Liu, Q.; Xia, X.; Wang, X.; Tu, J. Molybdenum Selenide Electrocatalysts for Electrochemical Hydrogen Evolution Reaction. *ChemElectroChem* **2019**, *6*, 3530−3548.

(34) Cai, Z.; Liu, B.; Zou, X.; Cheng, H. M. Chemical Vapor Deposition Growth and Applications of Two-Dimensional Materials and Their Heterostructures. *Chem. Rev.* **2018**, *118* (13), 6091−6133.

(35) Voiry, D.; Shin, H. S.; Loh, K. P.; Chhowalla, M. Low-Dimensional Catalysts for Hydrogen Evolution and CO2 Reduction. *Nat. Rev. Chem.* **2018**, *2*, 0105.

(36) Chia, X.; Pumera, M. Characteristics and Performance of Two-Dimensional Materials for Electrocatalysis. *Nat. Catal.* **2018**, *1* (12), 909−921.

https://doi.org/10.1021/acsmaterialsau.1c00006
ACS Mater. Au 2021, 1, 6−36

(37) Khan, K.; Tareen, A. K.; Aslam, M.; Zhang, Y.; Wang, R.; Ouyang, Z.; Gou, Z.; Zhang, H. Recent Advances in Two-Dimensional Materials and Their Nanocomposites in Sustainable Energy Conversion Applications. *Nanoscale* **2019**, *11* (45), 21622−21678.
(38) Chan, K.; Tsai, C.; Hansen, H. A.; Nørskov, J. K. Molybdenum Sulfides and Selenides as Possible Electrocatalysts for CO2 Reduction. *ChemCatChem* **2014**, *6* (7), 1899−1905.
(39) Asadi, M.; Kim, K.; Liu, C.; Addepalli, A. V.; Abbasi, P.; Yasaei, P.; Phillips, P.; Behranginia, A.; Cerrato, J. M.; Haasch, R.; Zapol, P.; Kumar, B.; Klie, R. F.; Abiade, J.; Curtiss, L. A.; Salehi-Khojin, A. Nanostructured Transition Metal Dichalcogenide Electrocatalysts for CO2 Reduction in Ionic Liquid. *Science (Washington, DC, U. S.)* **2016**, *353* (6298), 467−470.
(40) Liu, J.; Guo, C.; Vasileff, A.; Qiao, S. Nanostructured 2D Materials: Prospective Catalysts for Electrochemical CO2 Reduction. *Small Methods* **2017**, *1* (1−2), 1600006.
(41) Suryanto, B. H. R.; Wang, D.; Azofra, L. M.; Harb, M.; Cavallo, L.; Jalili, R.; Mitchell, D. R. G.; Chatti, M.; MacFarlane, D. R. MoS2 Polymorphic Engineering Enhances Selectivity in the Electrochemical Reduction of Nitrogen to Ammonia. *ACS Energy Lett.* **2019**, *4* (2), 430−435.
(42) Ren, Y.; Yu, C.; Tan, X.; Huang, H.; Wei, Q.; Qiu, J. Strategies to Suppress Hydrogen Evolution for Highly Selective Electrocatalytic Nitrogen Reduction: Challenges and Perspectives. *Energy Environ. Sci.* **2021**, *14* (3), 1176−1193.
(43) Xu, M.; Liang, T.; Shi, M.; Chen, H. Graphene-like Two-Dimensional Materials. *Chem. Rev.* **2013**, *113* (5), 3766−3798.
(44) Chia, X.; Eng, A. Y. S.; Ambrosi, A.; Tan, S. M.; Pumera, M. Electrochemistry of Nanostructured Layered Transition-Metal Dichalcogenides. *Chem. Rev.* **2015**, *115* (21), 11941−11966.
(45) Wilson, J. A.; Yoffe, A. D. The Transition Metal Dichalcogenides Discussion and Interpretation of the Observed Optical, Electrical and Structural Properties. *Adv. Phys.* **1969**, *18* (73), 193−335.
(46) Voiry, D.; Salehi, M.; Silva, R.; Fujita, T.; Chen, M.; Asefa, T.; Shenoy, V. B.; Eda, G.; Chhowalla, M. Conducting MoS2 Nanosheets as Catalysts for Hydrogen Evolution Reaction. *Nano Lett.* **2013**, *13* (12), 6222−6227.
(47) Lin, L.; Miao, N.; Wen, Y.; Zhang, S.; Ghosez, P.; Sun, Z.; Allwood, D. A. Sulfur-Depleted Monolayered Molybdenum Disulfide Nanocrystals for Superelectrochemical Hydrogen Evolution Reaction. *ACS Nano* **2016**, *10* (9), 8929−8937.
(48) Cai, L.; Cheng, W.; Yao, T.; Huang, Y.; Tang, F.; Liu, Q.; Liu, W.; Sun, Z.; Hu, F.; Jiang, Y.; Yan, W.; Wei, S. High-Content Metallic 1T Phase in MoS 2 -Based Electrocatalyst for Efficient Hydrogen Evolution. *J. Phys. Chem. C* **2017**, *121* (28), 15071−15077.
(49) Tributsch, H. Layer-Type Transition Metal Dichalcogenides - a New Class of Electrodes for Electrochemical Solar Cells. *Berichte der Bunsengesellschaft für Phys. Chemie* **1977**, *81* (4), 361−369.
(50) Sangwan, V. K.; Hersam, M. C. Electronic Transport in Two-Dimensional Materials. *Annu. Rev. Phys. Chem.* **2018**, *69* (1), 299−325.
(51) Wang, Q. H.; Kalantar-Zadeh, K.; Kis, A.; Coleman, J. N.; Strano, M. S. Electronics and Optoelectronics of Two-Dimensional Transition Metal Dichalcogenides. *Nat. Nanotechnol.* **2012**, *7* (11), 699−712.
(52) Wei, W.; Dai, Y.; Niu, C.; Huang, B. Controlling the Electronic Structures and Properties of In-Plane Transition-Metal Dichalcogenides Quantum Wells. *Sci. Rep.* **2015**, *5*, 17578.
(53) Wei, W.; Dai, Y.; Sun, Q.; Yin, N.; Han, S.; Huang, B.; Jacob, T. Electronic Structures of In-Plane Two-Dimensional Transition-Metal Dichalcogenide Heterostructures. *Phys. Chem. Chem. Phys.* **2015**, *17* (43), 29380−29386.
(54) Yu, Y.; Huang, S. Y.; Li, Y.; Steinmann, S. N.; Yang, W.; Cao, L. Layer-Dependent Electrocatalysis of MoS2 for Hydrogen Evolution. *Nano Lett.* **2014**, *14* (2), 553−558.
(55) Tsai, C.; Chan, K.; Nørskov, J. K.; Abild-Pedersen, F. Theoretical Insights into the Hydrogen Evolution Activity of Layered Transition Metal Dichalcogenides. *Surf. Sci.* **2015**, *640*, 133−140.
(56) Conway, B. E.; Bockris, J. O. Electrolytic Hydrogen Evolution Kinetics and Its Relation to the Electronic and Adsorptive Properties of the Metal. *J. Chem. Phys.* **1957**, *26* (3), 532−541.
(57) Nilsson, A.; Pettersson, L. G. M.; Hammer, B.; Bligaard, T.; Christensen, C. H.; Nørskov, J. K. The Electronic Structure Effect in Heterogeneous Catalysis. *Catal. Lett.* **2005**, *100* (3−4), 111−114.
(58) Nørskov, J. K.; Bligaard, T.; Rossmeisl, J.; Christensen, C. H. Towards the Computational Design of Solid Catalysts. *Nat. Chem.* **2009**, *1* (1), 37−46.
(59) Rothenberg, G. *Catalysis: Concepts and Green Applications*, 1st ed.; John Wiley and Sons, 2008; pp 1−279.
(60) Mak, K. F.; Lee, C.; Hone, J.; Shan, J.; Heinz, T. F. Atomically Thin MoS2: A New Direct-Gap Semiconductor. *Phys. Rev. Lett.* **2010**, *105* (13), 2−5.
(61) Splendiani, A.; Sun, L.; Zhang, Y.; Li, T.; Kim, J.; Chim, C. Y.; Galli, G.; Wang, F. Emerging Photoluminescence in Monolayer MoS 2. *Nano Lett.* **2010**, *10* (4), 1271−1275.
(62) Kwon, S. M.; Won, J. K.; Jo, J. W.; Kim, J.; Kim, H. J.; Kwon, H. I.; Kim, J.; Ahn, S.; Kim, Y. H.; Lee, M. J.; Lee, H. I.; Marks, T. J.; Kim, M. G.; Park, S. K. High-Performance and Scalable Metal-Chalcogenide Semiconductors and Devices via Chalco-Gel Routes. *Sci. Adv.* **2018**, *4* (4), eaap9104.
(63) Zeng, Q.; Liu, Z. Novel Optoelectronic Devices: Transition-Metal-Dichalcogenide-Based 2D Heterostructures. *Adv. Electron. Mater.* **2018**, *4* (2), 1700335.
(64) Morales-Guio, C. G.; Hu, X. Amorphous Molybdenum Sulfides as Hydrogen Evolution Catalysts. *Acc. Chem. Res.* **2014**, *47* (8), 2671−2681.
(65) Domínguez-Meister, S.; Conte, M.; Igartua, A.; Rojas, T. C.; Sánchez-López, J. C. Self-Lubricity of WSex Nanocomposite Coatings. *ACS Appl. Mater. Interfaces* **2015**, *7* (15), 7979−7986.
(66) Fominski, V. Y.; Grigoriev, S. N.; Romanov, R. I.; Volosova, M. A.; Grunin, A. I.; Teterina, G. D. The Formation of a Hybrid Structure from Tungsten Selenide and Oxide Plates for a Hydrogen-Evolution Electrocatalyst. *Tech. Phys. Lett.* **2016**, *42* (6), 555−558.
(67) Nguyen, Q. T.; Nguyen, P. D.; Nguyen, D.; Truong, Q. D.; Kim Chi, T. T.; Ung, T. T. D.; Honma, I.; Liem, N. Q.; Tran, P. D. Novel Amorphous Molybdenum Selenide as an Efficient Catalyst for Hydrogen Evolution Reaction. *ACS Appl. Mater. Interfaces* **2018**, *10* (10), 8659−8665.
(68) Nguyen, C. T.; Duong, T. M.; Nguyen, M.; Nguyen, Q. T.; Nguyen, A. D.; Dieu Thuy, U. T.; Truong, Q. D.; Nguyen, T. T.; Nguyen, Q. L.; Tran, P. D. Structure and Electrochemical Property of Amorphous Molybdenum Selenide H2-Evolving Catalysts Prepared by a Solvothermal Synthesis. *Int. J. Hydrogen Energy* **2019**, *44* (26), 13273−13283.
(69) Vrubel, H.; Merki, D.; Hu, X. Hydrogen Evolution Catalyzed by MoS3 and MoS2 Particles. *Energy Environ. Sci.* **2012**, *5* (3), 6136−6144.
(70) Merki, D.; Fierro, S.; Vrubel, H.; Hu, X. Amorphous Molybdenum Sulfide Films as Catalysts for Electrochemical Hydrogen Production in Water. *Chem. Sci.* **2011**, *2*, 1262−1267.
(71) Mabayoje, O.; Liu, Y.; Wang, M.; Shoola, A.; Ebrahim, A. M.; Frenkel, A. I.; Mullins, C. B. Electrodeposition of MoSx Hydrogen Evolution Catalysts from Sulfur-Rich Precursors. *ACS Appl. Mater. Interfaces* **2019**, *11* (36), 32879−32886.
(72) Hibble, S. J.; Rice, D. A.; Pickup, D. M.; Beer, M. P. Mo K-Edge EXAFS and S K-Edge Absorption Studies of the Amorphous Molybdenum Sulfides MoS4.7, MoS3, and MoS3·nH2O (n ∼ 2). *Inorg. Chem.* **1995**, *34* (21), 5109−5113.
(73) Hibble, S. J.; Rice, D. A.; Pickup, D. M.; Beer, M. P. Extended X-Ray Absorption Fine Structure Studies of the Amorphous Tungsten Sulfides and Selenides, WS5, WSe5 and WS3. *J. Chem. Soc., Faraday Trans.* **1996**, *92* (12), 2131−2136.
(74) Artemkina, S. B.; Enyashin, A. N.; Poltarak, A. A.; Fedorenko, A. D.; Makarova, A. A.; Poltarak, P. A.; Shin, E. J.; Hwang, S. J.; Kim,

S. J.; Grayfer, E. D.; Fedorov, V. E. Revealing the Flexible 1D Primary and Globular Secondary Structures of Sulfur-Rich Amorphous Transition Metal Polysulfides. *ChemNanoMat* **2019**, *5* (12), 1488−1497.
(75) Vrubel, H.; Hu, X. Growth and Activation of an Amorphous Molybdenum Sulfide Hydrogen Evolving Catalyst. *ACS Catal.* **2013**, *3* (9), 2002−2011.
(76) Tran, P. D.; Tran, T. V.; Orio, M.; Torelli, S.; Truong, Q. D.; Nayuki, K.; Sasaki, Y.; Chiam, S. Y.; Yi, R.; Honma, I.; Barber, J.; Artero, V. Coordination Polymer Structure and Revisited Hydrogen Evolution Catalytic Mechanism for Amorphous Molybdenum Sulfide. *Nat. Mater.* **2016**, *15*, 640.
(77) Kibsgaard, J.; Jaramillo, T. F.; Besenbacher, F. Building an Appropriate Active-Site Motif into a Hydrogen-Evolution Catalyst with Thiomolybdate [Mo3S13]2- Clusters. *Nat. Chem.* **2014**, *6* (3), 248−253.
(78) Benck, J. D.; Chen, Z.; Kuritzky, L. Y.; Forman, A. J.; Jaramillo, T. F. Amorphous Molybdenum Sulfide Catalysts for Electrochemical Hydrogen Production: Insights into the Origin of Their Catalytic Activity. *ACS Catal.* **2012**, *2*, 1916−1923.
(79) Escalera-López, D.; Lou, Z.; Rees, N. V. Benchmarking the Activity, Stability, and Inherent Electrochemistry of Amorphous Molybdenum Sulfide for Hydrogen Production. *Adv. Energy Mater.* **2019**, *9*, 1802614.
(80) Lee, S. C.; Benck, J. D.; Tsai, C.; Park, J.; Koh, A. L.; Abild-Pedersen, F.; Jaramillo, T. F.; Sinclair, R. Chemical and Phase Evolution of Amorphous Molybdenum Sulfide Catalysts for Electrochemical Hydrogen Production. *ACS Nano* **2016**, *10* (1), 624−632.
(81) Cao, P.; Peng, J.; Liu, S.; Cui, Y.; Hu, Y.; Chen, B.; Li, J.; Zhai, M. Tuning the Composition and Structure of Amorphous Molybdenum Sulfide/Carbon Black Nanocomposites by Radiation Technique for Highly Efficient Hydrogen Evolution. *Sci. Rep.* **2017**, *7* (1), 1−11.
(82) Wu, L.; Longo, A.; Dzade, N. Y.; Sharma, A.; Hendrix, M. M. R. M.; Bol, A. A.; de Leeuw, N. H.; Hensen, E. J. M.; Hofmann, J. P. The Origin of High Activity of Amorphous MoS2 in the Hydrogen Evolution Reaction. *ChemSusChem* **2019**, *12* (19), 4383−4389.
(83) Toh, R. J.; Sofer, Z.; Pumera, M. Catalytic Properties of Group 4 Transition Metal Dichalcogenides (MX2; M = Ti, Zr, Hf; X = S, Se, Te). *J. Mater. Chem. A* **2016**, *4* (47), 18322−18334.
(84) Chia, X.; Pumera, M. Layered Transition Metal Dichalcogenide Electrochemistry: Journey across the Periodic Table. *Chem. Soc. Rev.* **2018**, *47* (15), 5602−5613.
(85) Chia, X.; Ambrosi, A.; Lazar, P.; Sofer, Z.; Pumera, M. Electrocatalysis of Layered Group 5 Metallic Transition Metal Dichalcogenides (MX2, M = V, Nb, and Ta; X = S, Se, and Te). *J. Mater. Chem. A* **2016**, *4* (37), 14241−14253.
(86) Liu, Y.; Wu, J.; Hackenberg, K. P.; Zhang, J.; Wang, Y. M.; Yang, Y.; Keyshar, K.; Gu, J.; Ogitsu, T.; Vajtai, R.; Lou, J.; Ajayan, P. M.; Wood, B. C.; Yakobson, B. I. Self-Optimizing, Highly Surface-Active Layered Metal Dichalcogenide Catalysts for Hydrogen Evolution. *Nat. Energy* **2017**, *2* (July), 1−7.
(87) Najafi, L.; Bellani, S.; Oropesa-Nuñez, R.; Martín-García, B.; Prato, M.; Pasquale, L.; Panda, J. K.; Marvan, P.; Sofer, Z.; Bonaccorso, F. TaS2, TaSe2, and Their Heterogeneous Films as Catalysts for the Hydrogen Evolution Reaction. *ACS Catal.* **2020**, *10* (5), 3313−3325.
(88) Martín-García, B.; Spirito, D.; Bellani, S.; Prato, M.; Romano, V.; Polovitsyn, A.; Brescia, R.; Oropesa-Nuñez, R.; Najafi, L.; Ansaldo, A.; D'Angelo, G.; Pellegrini, V.; Krahne, R.; Moreels, I.; Bonaccorso, F. Extending the Colloidal Transition Metal Dichalcogenide Library to ReS2 Nanosheets for Application in Gas Sensing and Electrocatalysis. *Small* **2019**, *15* (52), 1904670.
(89) Zhu, C.; Gao, D.; Ding, J.; Chao, D.; Wang, J. TMD-Based Highly Efficient Electrocatalysts Developed by Combined Computational and Experimental Approaches. *Chem. Soc. Rev.* **2018**, *47* (12), 4332−4356.
(90) Shi, J.; Wang, X.; Zhang, S.; Xiao, L.; Huan, Y.; Gong, Y.; Zhang, Z.; Li, Y.; Zhou, X.; Hong, M.; Fang, Q.; Zhang, Q.; Liu, X.; Gu, L.; Liu, Z.; Zhang, Y. Two-Dimensional Metallic Tantalum Disulfide as a Hydrogen Evolution Catalyst. *Nat. Commun.* **2017**, *8* (1), 1−9.
(91) Yuan, J.; Wu, J.; Hardy, W. J.; Loya, P.; Lou, M.; Yang, Y.; Najmaei, S.; Jiang, M.; Qin, F.; Keyshar, K.; Ji, H.; Gao, W.; Bao, J.; Kono, J.; Natelson, D.; Ajayan, P. M.; Lou, J. Facile Synthesis of Single Crystal Vanadium Disulfide Nanosheets by Chemical Vapor Deposition for Efficient Hydrogen Evolution Reaction. *Adv. Mater.* **2015**, *27* (37), 5605−5609.
(92) Kim, J. H.; Kim, H.; Kim, J.; Lee, H. J.; Jang, J. H.; Ahn, S. H. Electrodeposited Molybdenum Sulfide as a Cathode for Proton Exchange Membrane Water Electrolyzer. *J. Power Sources* **2018**, *392*, 69−78.
(93) Morozan, A.; Johnson, H.; Roiron, C.; Genay, G.; Aldakov, D.; Ghedjatti, A.; Nguyen, C. T.; Tran, P. D.; Kinge, S.; Artero, V. Nonprecious Bimetallic Iron−Molybdenum Sulfide Electrocatalysts for the Hydrogen Evolution Reaction in Proton Exchange Membrane Electrolyzers. *ACS Catal.* **2020**, *10*, 14336−14348.
(94) Holzapfel, P. K. R.; Bühler, M.; Escalera-López, D.; Bierling, M.; Speck, F. D.; Mayrhofer, K. J. J.; Cherevko, S.; Pham, C. V.; Thiele, S. Fabrication of a Robust PEM Water Electrolyzer Based on Non-Noble Metal Cathode Catalyst: [Mo3S13]2− Clusters Anchored to N-Doped Carbon Nanotubes. *Small* **2020**, *16* (37), 2003161.
(95) McCrory, C. C. L.; Jung, S.; Ferrer, I. M.; Chatman, S. M.; Peters, J. C.; Jaramillo, T. F. Benchmarking Hydrogen Evolving Reaction and Oxygen Evolving Reaction Electrocatalysts for Solar Water Splitting Devices. *J. Am. Chem. Soc.* **2015**, *137* (13), 4347−4357.
(96) Fu, Q.; Han, J.; Wang, X.; Xu, P.; Yao, T.; Zhong, J.; Zhong, W.; Liu, S.; Gao, T.; Zhang, Z.; Xu, L.; Song, B. 2D Transition Metal Dichalcogenides: Design, Modulation, and Challenges in Electrocatalysis. *Adv. Mater.* **2021**, *33* (6), 1907818.
(97) Wei, C.; Rao, R. R.; Peng, J.; Huang, B.; Stephens, I. E. L.; Risch, M.; Xu, Z. J.; Shao-Horn, Y. Recommended Practices and Benchmark Activity for Hydrogen and Oxygen Electrocatalysis in Water Splitting and Fuel Cells. *Adv. Mater.* **2019**, *31* (31), 1806296.
(98) Tsai, C.; Chan, K.; Abild-Pedersen, F.; Nørskov, J. K. Active Edge Sites in MoSe2 and WSe2 Catalysts for the Hydrogen Evolution Reaction: A Density Functional Study. *Phys. Chem. Chem. Phys.* **2014**, *16* (26), 13156−13164.
(99) Jaramillo, T. F.; Jorgensen, K. P.; Bonde, J.; Nielsen, J. H.; Horch, S.; Chorkendorff, I. Identification of Active Edge Sites for Electrochemical H2 Evolution from MoS2 Nanocatalysts. *Science (Washington, DC, U. S.)* **2007**, *317* (5834), 100−102.
(100) Mitterreiter, E.; Liang, Y.; Golibrzuch, M.; McLaughlin, D.; Csoklich, C.; Bartl, J. D.; Holleitner, A.; Wurstbauer, U.; Bandarenka, A. S. In-Situ Visualization of Hydrogen Evolution Sites on Helium Ion Treated Molybdenum Dichalcogenides under Reaction Conditions. *npj 2D Mater. Appl.* **2019**, *3* (1), 1−9.
(101) Lassalle-Kaiser, B.; Merki, D.; Vrubel, H.; Gul, S.; Yachandra, V. K.; Hu, X.; Yano, J. Evidence from in Situ X-Ray Absorption Spectroscopy for the Involvement of Terminal Disulfide in the Reduction of Protons by an Amorphous Molybdenum Sulfide Electrocatalyst. *J. Am. Chem. Soc.* **2015**, *137* (1), 314−321.
(102) Deng, Y.; Ting, L. R. L.; Neo, P. H. L.; Zhang, Y. J.; Peterson, A. A.; Yeo, B. S. Operando Raman Spectroscopy of Amorphous Molybdenum Sulfide (MoSx) during the Electrochemical Hydrogen Evolution Reaction: Identification of Sulfur Atoms as Catalytically Active Sites for H+ Reduction. *ACS Catal.* **2016**, *6* (11), 7790−7798.
(103) Ting, L. R. L.; Deng, Y.; Ma, L.; Zhang, Y. J.; Peterson, A. A.; Yeo, B. S. Catalytic Activities of Sulfur Atoms in Amorphous Molybdenum Sulfide for the Electrochemical Hydrogen Evolution Reaction. *ACS Catal.* **2016**, *6* (2), 861−867.
(104) Geng, X.; Sun, W.; Wu, W.; Chen, B.; Al-hilo, A.; Benamara, M.; Zhu, H.; Watanabe, F.; Cui, J.; Chen, T. Pure and Stable Metallic Phase Molybdenum Disulfide Nanosheets for Hydrogen Evolution Reaction. *Nat. Commun.* **2016**, *7*, 1−7.

https://doi.org/10.1021/acsmaterialsau.1c00006
ACS Mater. Au 2021, 1, 6−36

(105) Li, H.; Jia, X.; Zhang, Q.; Wang, X. Metallic Transition-Metal Dichalcogenide Nanocatalysts for Energy Conversion. *Chem.* **2018**, *4* (7), 1510−1537.
(106) Duerloo, K. A. N.; Li, Y.; Reed, E. J. Structural Phase Transitions in Two-Dimensional Mo-and W-Dichalcogenide Monolayers. *Nat. Commun.* **2014**, *5*, 4214.
(107) Voiry, D.; Mohite, A.; Chhowalla, M. Phase Engineering of Transition Metal Dichalcogenides. *Chem. Soc. Rev.* **2015**, *44* (9), 2702−2712.
(108) Zheng, L.; Gong, Y.; Han, S.; Goh, M. H.; Zhang, H.; Gu, L.; Chaturvedi, A.; Qi, X.; Wang, J.; Kloc, C.; Zhang, X.; Luo, Z.; Wu, X.-J.; Tan, C.; Cai, Y.; Du, Y.; Huang, Y.; Lai, Z. Preparation of High-Percentage 1T-Phase Transition Metal Dichalcogenide Nanodots for Electrochemical Hydrogen Evolution. *Adv. Mater.* **2018**, *30* (9), 1705509.
(109) Luo, Z.; Ouyang, Y.; Zhang, H.; Xiao, M.; Ge, J.; Jiang, Z.; Wang, J.; Tang, D.; Cao, X.; Liu, C.; Xing, W. Chemically Activating MoS2 via Spontaneous Atomic Palladium Interfacial Doping towards Efficient Hydrogen Evolution. *Nat. Commun.* **2018**, *9* (1), 1−8.
(110) Yu, Y.; Nam, G. H.; He, Q.; Wu, X. J.; Zhang, K.; Yang, Z.; Chen, J.; Ma, Q.; Zhao, M.; Liu, Z.; Ran, F. R.; Wang, X.; Li, H.; Huang, X.; Li, B.; Xiong, Q.; Zhang, Q.; Liu, Z.; Gu, L.; Du, Y.; Huang, W.; Zhang, H. High Phase-Purity 1T′-MoS2- and 1T′-MoSe2-Layered Crystals. *Nat. Chem.* **2018**, *10* (6), 638−643.
(111) Tan, C.; Luo, Z.; Chaturvedi, A.; Cai, Y.; Du, Y.; Gong, Y.; Huang, Y.; Lai, Z.; Zhang, X.; Zheng, L.; Qi, X.; Goh, M. H.; Wang, J.; Han, S.; Wu, X. J.; Gu, L.; Kloc, C.; Zhang, H. Preparation of High-Percentage 1T-Phase Transition Metal Dichalcogenide Nanodots for Electrochemical Hydrogen Evolution. *Adv. Mater.* **2018**, *30* (9), 1705509.
(112) Vante, N. A.; Jaegermann, W.; Tributsch, H.; Hönle, W.; Yvon, K. Electrocatalysis of Oxygen Reduction by Chalcogenides Containing Mixed Transition Metal Clusters. *J. Am. Chem. Soc.* **1987**, *109* (11), 3251−3257.
(113) Ortiz-Rodríguez, J. C.; Singstock, N. R.; Perryman, J. T.; Hyler, F. P.; Jones, S. J.; Holder, A. M.; Musgrave, C. B.; Velázquez, J. M. Stabilizing Hydrogen Adsorption through Theory-Guided Chalcogen Substitution in Chevrel-Phase Mo6 × 8(X = S, Se, Te) Electrocatalysts. *ACS Appl. Mater. Interfaces* **2020**, *12* (32), 35995−36003.
(114) Naik, K. M.; Sampath, S. Cubic Mo6S8-Efficient Electrocatalyst Towards Hydrogen Evolution Over Wide PH Range. *Electrochim. Acta* **2017**, *252*, 408−415.
(115) Strachan, J.; Masters, A. F.; Maschmeyer, T. Chevrel Phase Nanoparticles as Electrocatalysts for Hydrogen Evolution. *ACS Appl. Nano Mater.* **2021**, *4* (2), 2030−2036.
(116) Jiang, J.; Gao, M.; Sheng, W.; Yan, Y. Hollow Chevrel-Phase NiMo3S4for Hydrogen Evolution in Alkaline Electrolytes. *Angew. Chem., Int. Ed.* **2016**, *55* (49), 15240−15245.
(117) Bae, C.; Ho, T. A.; Kim, H.; Lee, S.; Lim, S.; Kim, M.; Yoo, H.; Montero-Moreno, J. M.; Park, J. H.; Shin, H. Bulk Layered Heterojunction as an Efficient Electrocatalyst for Hydrogen Evolution. *Sci. Adv.* **2017**, *3* (3), e1602215.
(118) Liu, P.; Choi, Y.; Yang, Y.; White, M. G. Methanol Synthesis from H2 and CO2 on a Mo6S8 Cluster: A Density Functional Study. *J. Phys. Chem. A* **2010**, *114* (11), 3888−3895.
(119) Kim, M.-C.; Nam, H.; Choi, J.; Kim, H. S.; Lee, H. W.; Kim, D.; Kong, J.; Han, S. S.; Lee, S. Y.; Park, H. S. Hydrogen Bonding-Mediated Enhancement of Bioinspired Electrochemical Nitrogen Reduction on Cu2-XS Catalysts. *ACS Catal.* **2020**, *10* (18), 10577−10584.
(120) Deng, D.; Novoselov, K. S.; Fu, Q.; Zheng, N.; Tian, Z.; Bao, X. Catalysis with Two-Dimensional Materials and Their Heterostructures. *Nat. Nanotechnol.* **2016**, *11* (3), 218−230.
(121) Voiry, D.; Yang, J.; Chhowalla, M. Recent Strategies for Improving the Catalytic Activity of 2D TMD Nanosheets Toward the Hydrogen Evolution Reaction. *Adv. Mater.* **2016**, *28* (29), 6197−6206.
(122) Seh, Z. W.; Kibsgaard, J.; Dickens, C. F.; Chorkendorff, I.; Nørskov, J. K.; Jaramillo, T. F. Combining Theory and Experiment in Electrocatalysis: Insights into Materials Design. *Science (Washington, DC, U. S.)* **2017**, *355* (6321), eaad4998.
(123) Guo, Y.; Park, T.; Yi, J. W.; Henzie, J.; Kim, J.; Wang, Z.; Jiang, B.; Bando, Y.; Sugahara, Y.; Tang, J.; Yamauchi, Y. Nanoarchitectonics for Transition-Metal-Sulfide-Based Electrocatalysts for Water Splitting. *Adv. Mater.* **2019**, *31* (17), 1807134.
(124) Wang, Q.; Lei, Y.; Wang, Y.; Liu, Y.; Song, C.; Zeng, J.; Song, Y.; Duan, X.; Wang, D.; Li, Y. Atomic-Scale Engineering of Chemical-Vapor-Deposition-Grown 2D Transition Metal Dichalcogenides for Electrocatalysis. *Energy Environ. Sci.* **2020**, *13*, 1593−1616.
(125) Carvalho, A.; Ribeiro, R. M.; Castro Neto, A. H. Band Nesting and the Optical Response of Two-Dimensional Semiconducting Transition Metal Dichalcogenides. *Phys. Rev. B: Condens. Matter Mater. Phys.* **2013**, *88* (11), 1−6.
(126) Kobayashi, K.; Yamauchi, J. Electronic Structure and Scanning-Tunneling-Microscopy Image of Molybdenum Dichalcogenide Surfaces. *Phys. Rev. B: Condens. Matter Mater. Phys.* **1995**, *51* (23), 17085−17095.
(127) Zeng, Z.; Yin, Z.; Huang, X.; Li, H.; He, Q.; Lu, G.; Boey, F.; Zhang, H. Single-Layer Semiconducting Nanosheets: High-Yield Preparation and Device Fabrication. *Angew. Chem., Int. Ed.* **2011**, *50* (47), 11093−11097.
(128) Liu, K.; Zhang, L.; Cao, T.; Jin, C.; Qiu, D.; Zhou, Q.; Zettl, A.; Yang, P.; Louie, S. G.; Wang, F. Evolution of Interlayer Coupling in Twisted Molybdenum Disulfide Bilayers. *Nat. Commun.* **2014**, *5*, 1−6.
(129) Seo, B.; Jung, G. Y.; Sa, Y. J.; Jeong, H. Y.; Cheon, J. Y.; Lee, J. H.; Kim, H. Y.; Kim, J. C.; Shin, H. S.; Kwak, S. K.; Joo, S. H. Monolayer-Precision Synthesis of Molybdenum Sulfide Nanoparticles and Their Nanoscale Size Effects in the Hydrogen Evolution Reaction. *ACS Nano* **2015**, *9* (4), 3728−3739.
(130) Manikandan, A.; Chen, Y. Z.; Shen, C. C.; Sher, C. W.; Kuo, H. C.; Chueh, Y. L. A Critical Review on Two-Dimensional Quantum Dots (2D QDs): From Synthesis toward Applications in Energy and Optoelectronics. *Prog. Quantum Electron.* **2019**, *68*, 100226.
(131) Zhang, J.; Ling, C.; Zang, W.; Li, X.; Huang, S.; Li, X. L.; Yan, D.; Kou, Z.; Liu, L.; Wang, J.; Yang, H. Y. Boosted Electrochemical Ammonia Synthesis by High-Percentage Metallic Transition Metal Dichalcogenide Quantum Dots. *Nanoscale* **2020**, *12* (20), 10964−10971.
(132) Zhao, X.; Ma, X.; Sun, J.; Li, D.; Yang, X. Enhanced Catalytic Activities of Surfactant-Assisted Exfoliated WS2 Nanodots for Hydrogen Evolution. *ACS Nano* **2016**, *10* (2), 2159−2166.
(133) Chen, W.; Gu, J.; Liu, Q.; Luo, R.; Yao, L.; Sun, B.; Zhang, W.; Su, H.; Chen, B.; Liu, P.; Zhang, D. Quantum Dots of 1T Phase Transitional Metal Dichalcogenides Generated via Electrochemical Li Intercalation. *ACS Nano* **2018**, *12* (1), 308−316.
(134) Mabayoje, O.; Wygant, B. R.; Wang, M.; Liu, Y.; Mullins, C. B. Sulfur-Rich MoS6 as an Electrocatalyst for the Hydrogen Evolution Reaction. *ACS Appl. Energy Mater.* **2018**, *1* (9), 4453−4458.
(135) Li, B.; Jiang, L.; Li, X.; Cheng, Z.; Ran, P.; Zuo, P.; Qu, L.; Zhang, J.; Lu, Y. Controllable Synthesis of Nanosized Amorphous MoSx Using Temporally Shaped Femtosecond Laser for Highly Efficient Electrochemical Hydrogen Production. *Adv. Funct. Mater.* **2019**, *29* (1), 1806229.
(136) Lee, C. H.; Lee, S.; Kang, G. S.; Lee, Y. K.; Park, G. G.; Lee, D. C.; Joh, H. I. Insight into the Superior Activity of Bridging Sulfur-Rich Amorphous Molybdenum Sulfide for Electrochemical Hydrogen Evolution Reaction. *Appl. Catal., B* **2019**, *258* (April), 117995.
(137) Lee, C. H.; Lee, S.; Lee, Y. K.; Jung, Y. C.; Ko, Y. Il; Lee, D. C.; Joh, H. I. Understanding the Origin of Formation and Active Sites for Thiomolybdate [Mo3S13]2- Clusters as Hydrogen Evolution Catalyst through the Selective Control of Sulfur Atoms. *ACS Catal.* **2018**, *8* (6), 5221−5227.
(138) Li, H.; Liu, X.; Chen, S.; Yang, D.; Zhang, Q.; Song, L.; Xiao, H.; Zhang, Q.; Gu, L.; Wang, X. Edge-Exposed Molybdenum Disulfide with N-Doped Carbon Hybridization: A Hierarchical

Hollow Electrocatalyst for Carbon Dioxide Reduction. *Adv. Energy Mater.* **2019**, *9* (18), 1900072.
(139) Li, X.; Li, T.; Ma, Y.; Wei, Q.; Qiu, W.; Guo, H.; Shi, X.; Zhang, P.; Asiri, A. M.; Chen, L.; Tang, B.; Sun, X. Boosted Electrocatalytic N2 Reduction to NH3 by Defect-Rich MoS2 Nanoflower. *Adv. Energy Mater.* **2018**, *8* (30), 1801357.
(140) Deng, J.; Li, H.; Xiao, J.; Tu, Y.; Deng, D.; Yang, H.; Tian, H.; Li, J.; Ren, P.; Bao, X. Triggering the Electrocatalytic Hydrogen Evolution Activity of the Inert Two-Dimensional MoS2 Surface via Single-Atom Metal Doping. *Energy Environ. Sci.* **2015**, *8* (5), 1594−1601.
(141) Li, H.; Wang, L.; Dai, Y.; Pu, Z.; Lao, Z.; Chen, Y.; Wang, M.; Zheng, X.; Zhu, J.; Zhang, W.; Si, R.; Ma, C.; Zeng, J. Synergetic Interaction between Neighbouring Platinum Monomers in CO2 Hydrogenation. *Nat. Nanotechnol.* **2018**, *13* (5), 411−417.
(142) Tedstone, A. A.; Lewis, D. J.; O'Brien, P. Synthesis, Properties, and Applications of Transition Metal-Doped Layered Transition Metal Dichalcogenides. *Chem. Mater.* **2016**, *28* (7), 1965−1974.
(143) Hong, X.; Chan, K.; Tsai, C.; Nørskov, J. K. How Doped MoS2 Breaks Transition-Metal Scaling Relations for CO2 Electrochemical Reduction. *ACS Catal.* **2016**, *6* (7), 4428−4437.
(144) Zang, Y.; Niu, S.; Wu, Y.; Zheng, X.; Cai, J.; Ye, J.; Xie, Y.; Liu, Y.; Zhou, J.; Zhu, J.; Liu, X.; Wang, G.; Qian, Y. Tuning Orbital Orientation Endows Molybdenum Disulfide with Exceptional Alkaline Hydrogen Evolution Capability. *Nat. Commun.* **2019**, *10* (1), 1−8.
(145) Huang, Y.; Sun, Y.; Zheng, X.; Aoki, T.; Pattengale, B.; Huang, J.; He, X.; Bian, W.; Younan, S.; Williams, N.; Hu, J.; Ge, J.; Pu, N.; Yan, X.; Pan, X.; Zhang, L.; Wei, Y.; Gu, J. Atomically Engineering Activation Sites onto Metallic 1T-MoS 2 Catalysts for Enhanced Electrochemical Hydrogen Evolution. *Nat. Commun.* **2019**, *10* (1), 1−11.
(146) Shin, S.; Jin, Z.; Ham, S. Y.; Lee, S.; Shin, D. S.; Min, Y. S. Effect of Oxygen Incorporation in Amorphous Molybdenum Sulfide on Electrochemical Hydrogen Evolution. *Appl. Surf. Sci.* **2019**, *487* (April), 981−989.
(147) Giuffredi, G.; Mezzetti, A.; Perego, A.; Mazzolini, P.; Prato, M.; Fumagalli, F.; Lin, Y.-C.; Liu, C.; Ivanov, I. N.; Belianinov, A.; Colombo, M.; Divitini, G.; Ducati, C.; Duscher, G.; Puretzky, A. A.; Geohegan, D. B.; Di Fonzo, F. Non-Equilibrium Synthesis of Highly Active Nanostructured, Oxygen-Incorporated Amorphous Molybdenum Sulfide HER Electrocatalyst. *Small* **2020**, *16*, 2004047.
(148) Ding, R.; Wang, M.; Wang, X.; Wang, H.; Wang, L.; Mu, Y.; Lv, B. N-Doped Amorphous MoSx for the Hydrogen Evolution Reaction. *Nanoscale* **2019**, *11* (23), 11217−11226.
(149) Zheng, Z.; Su, T.; Shi, J.; Tong, R.; Xiao, H.; Zhang, Q.; Zhang, Y.; Wang, Z.; Li, Q.; Wang, X. Boosting the Electrocatalytic Activity of Amorphous Molybdenum Sulfide Nanoflakes via Nickel Sulfide Decoration. *Nanoscale* **2019**, *11* (47), 22971−22979.
(150) Abbasi, P.; Asadi, M.; Liu, C.; Sharifi-Asl, S.; Sayahpour, B.; Behranginia, A.; Zapol, P.; Shahbazian-Yassar, R.; Curtiss, L. A.; Salehi-Khojin, A. Tailoring the Edge Structure of Molybdenum Disulfide toward Electrocatalytic Reduction of Carbon Dioxide. *ACS Nano* **2017**, *11* (1), 453−460.
(151) Lv, K.; Suo, W.; Shao, M.; Zhu, Y.; Wang, X.; Feng, J.; Fang, M.; Zhu, Y. Nitrogen Doped MoS2 and Nitrogen Doped Carbon Dots Composite Catalyst for Electroreduction CO2 to CO with High Faradaic Efficiency. *Nano Energy* **2019**, *63* (May), 103834.
(152) Gao, G.; Sun, Q.; Du, A. Activating Catalytic Inert Basal Plane of Molybdenum Disulfide to Optimize Hydrogen Evolution Activity via Defect Doping and Strain Engineering. *J. Phys. Chem. C* **2016**, *120* (30), 16761−16766.
(153) Yang, Q.; Wang, Z.; Dong, L.; Zhao, W.; Jin, Y.; Fang, L.; Hu, B.; Dong, M. Activating MoS2 with Super-High Nitrogen-Doping Concentration as Efficient Catalyst for Hydrogen Evolution Reaction. *J. Phys. Chem. C* **2019**, *123* (17), 10917−10925.
(154) Li, L.; Li, B.; Guo, Q.; Li, B. Theoretical Screening of Single-Atom-Embedded MoSSe Nanosheets for Electrocatalytic N2 Fixation. *J. Phys. Chem. C* **2019**, *123* (23), 14501−14507.
(155) Li, H.; Tsai, C.; Koh, A. L.; Cai, L.; Contryman, A. W.; Fragapane, A. H.; Zhao, J.; Han, H. S.; Manoharan, H. C.; Abild-Pedersen, F.; Nørskov, J. K.; Zheng, X. Activating and Optimizing MoS2 Basal Planes for Hydrogen Evolution through the Formation of Strained Sulphur Vacancies. *Nat. Mater.* **2016**, *15* (1), 48−53.
(156) Lin, S. H.; Kuo, J. L. Activating and Tuning Basal Planes of MoO2, MoS2, and MoSe2 for Hydrogen Evolution Reaction. *Phys. Chem. Chem. Phys.* **2015**, *17* (43), 29305−29310.
(157) Li, G.; Zhang, D.; Qiao, Q.; Yu, Y.; Peterson, D.; Zafar, A.; Kumar, R.; Curtarolo, S.; Hunte, F.; Shannon, S.; Zhu, Y.; Yang, W.; Cao, L. All the Catalytic Active Sites of MoS2 for Hydrogen Evolution. *J. Am. Chem. Soc.* **2016**, *138* (51), 16632−16638.
(158) Dong, L.; Guo, S.; Wang, Y.; Zhang, Q.; Gu, L.; Pan, C.; Zhang, J. Activating MoS2 Basal Planes for Hydrogen Evolution through Direct CVD Morphology Control. *J. Mater. Chem. A* **2019**, *7* (48), 27603−27611.
(159) Wei, C.; Wu, W.; Li, H.; Lin, X.; Wu, T.; Zhang, Y.; Xu, Q.; Zhang, L.; Zhu, Y.; Yang, X.; Liu, Z.; Xu, Q. Atomic Plane-Vacancy Engineering of Transition-Metal Dichalcogenides with Enhanced Hydrogen Evolution Capability. *ACS Appl. Mater. Interfaces* **2019**, *11* (28), 25264−25270.
(160) Li, L.; Qin, Z.; Ries, L.; Hong, S.; Michel, T.; Yang, J.; Salameh, C.; Bechelany, M.; Miele, P.; Kaplan, D.; Chhowalla, M.; Voiry, D. Role of Sulfur Vacancies and Undercoordinated Mo Regions in MoS2 Nanosheets toward the Evolution of Hydrogen. *ACS Nano* **2019**, *13* (6), 6824−6834.
(161) Voiry, D.; Yamaguchi, H.; Li, J.; Silva, R.; Alves, D. C. B.; Fujita, T.; Chen, M.; Asefa, T.; Shenoy, V. B.; Eda, G.; Chhowalla, M. Enhanced Catalytic Activity in Strained Chemically Exfoliated WS2nanosheets for Hydrogen Evolution. *Nat. Mater.* **2013**, *12* (9), 850−855.
(162) Yao, X.; Chen, Z.; Wang, Y.; Lang, X.; Gao, W.; Zhu, Y.; Jiang, Q. Activated Basal Planes of WS2 by Intrinsic Defects as Catalysts for the Electrocatalytic Nitrogen Reduction Reaction. *J. Mater. Chem. A* **2019**, *7* (45), 25961−25968.
(163) Chen, Z. W.; Gao, W.; Zheng, W. T.; Jiang, Q. Steric Hindrance in Sulfur Vacancy of Monolayer MoS2 Boosts Electrochemical Reduction of Carbon Monoxide to Methane. *ChemSusChem* **2018**, *11* (9), 1455−1459.
(164) Kang, S.; Han, S.; Kang, Y. Unveiling Electrochemical Reaction Pathways of CO2 Reduction to CN Species at S-Vacancies of MoS2. *ChemSusChem* **2019**, *12*, 2671−2678.
(165) Khezri, B.; Fisher, A. C.; Pumera, M. CO2 Reduction: The Quest for Electrocatalytic Materials. *J. Mater. Chem. A* **2017**, *5* (18), 8230−8246.
(166) Geng, P.; Zheng, S.; Tang, H.; Zhu, R.; Zhang, L.; Cao, S.; Xue, H.; Pang, H. Transition Metal Sulfides Based on Graphene for Electrochemical Energy Storage. *Adv. Energy Mater.* **2018**, *8* (15), 1703259.
(167) Yun, Q.; Lu, Q.; Zhang, X.; Tan, C.; Zhang, H. Three-Dimensional Architectures Constructed from Transition-Metal Dichalcogenide Nanomaterials for Electrochemical Energy Storage and Conversion. *Angew. Chem., Int. Ed.* **2018**, *57* (3), 626−646.
(168) Hasani, A.; Tekalgne, M.; Le, Q. V.; Jang, H. W.; Kim, S. Y. Two-Dimensional Materials as Catalysts for Solar Fuels: Hydrogen Evolution Reaction and CO 2 Reduction. *J. Mater. Chem. A* **2019**, *7* (2), 430−454.
(169) Ye, Z.; Yang, J.; Li, B.; Shi, L.; Ji, H.; Song, L.; Xu, H. Amorphous Molybdenum Sulfide/Carbon Nanotubes Hybrid Nanospheres Prepared by Ultrasonic Spray Pyrolysis for Electrocatalytic Hydrogen Evolution. *Small* **2017**, *13* (21), 1700111.
(170) Wu, Q.; Jiang, T.; Li, H.; Li, M. Anchoring Acetylene Black on Graphene for Growing of Molybdenum Disulfide as High Performance Electrocatalysts in Hydrogen Evolution Reaction. *Electrochim. Acta* **2020**, *338*, 135888.
(171) Lu, S.; Wang, W.; Yang, S.; Chen, W.; Zhuang, Z.; Tang, W.; He, C.; Qian, J.; Ma, D.; Yang, Y.; Huang, S. Amorphous MoS2 Confined in Nitrogen-Doped Porous Carbon for Improved Electro-

https://doi.org/10.1021/acsmaterialsau.1c00006
ACS Mater. Au 2021, 1, 6−36

catalytic Stability toward Hydrogen Evolution Reaction. *Nano Res.* **2019**, *12* (12), 3116−3122.
(172) Wang, R.; Sun, P.; Wang, H.; Wang, X. Pulsed Laser Deposition of Amorphous Molybdenum Disulfide Films for Efficient Hydrogen Evolution Reaction. *Electrochim. Acta* **2017**, *258*, 876−882.
(173) Yu, L.; Xie, Y.; Zhou, J.; Li, Y.; Yu, Y.; Ren, Z. Robust and Selective Electrochemical Reduction of CO2: The Case of Integrated 3D TiO2@MoS2 Architectures and Ti-S Bonding Effects. *J. Mater. Chem. A* **2018**, *6* (11), 4706−4713.
(174) Kuhl, K. P.; Cave, E. R.; Abram, D. N.; Jaramillo, T. F. New Insights into the Electrochemical Reduction of Carbon Dioxide on Metallic Copper Surfaces. *Energy Environ. Sci.* **2012**, *5* (5), 7050−7059.
(175) Clark, E. L.; Resasco, J.; Landers, A.; Lin, J.; Chung, L. T.; Walton, A.; Hahn, C.; Jaramillo, T. F.; Bell, A. T. Standards and Protocols for Data Acquisition and Reporting for Studies of the Electrochemical Reduction of Carbon Dioxide. *ACS Catal.* **2018**, *8* (7), 6560−6570.
(176) Liu, M.; Pang, Y.; Zhang, B.; De Luna, P.; Voznyy, O.; Xu, J.; Zheng, X.; Dinh, C. T.; Fan, F.; Cao, C.; de Arquer, F. P. G.; Safaei, T. S.; Mepham, A.; Klinkova, A.; Kumacheva, E.; Filleter, T.; Sinton, D.; Kelley, S. O.; Sargent, E. H. Enhanced Electrocatalytic CO2 Reduction via Field-Induced Reagent Concentration. *Nature* **2016**, *537* (7620), 382−386.
(177) Dinh, C.-T.; Garcia de Arquer, F. P.; Sinton, D.; Sargent, E. H. High Rate, Selective and Stable Electroreduction of CO2 to CO in Basic and Neutral Media. *ACS Energy Lett.* **2018**, *3*, 2835.
(178) Hori, Y. Electrochemical CO 2 Reduction on Metal Electrodes. *Modern Aspects of Electrochemistry; Springer: New York* **2008**, *42*, 89−189.
(179) Chen, Y.; Kanan, M. W. Tin Oxide Dependence of the CO2 Reduction Efficiency on Tin Electrodes and Enhanced Activity for Tin/Tin Oxide Thin-Film Catalysts. *J. Am. Chem. Soc.* **2012**, *134* (4), 1986−1989.
(180) Zhou, Y.; Che, F.; Liu, M.; Zou, C.; Liang, Z.; De Luna, P.; Yuan, H.; Li, J.; Wang, Z.; Xie, H.; Li, H.; Chen, P.; Bladt, E.; Quintero-Bermudez, R.; Sham, T. K.; Bals, S.; Hofkens, J.; Sinton, D.; Chen, G.; Sargent, E. H. Dopant-Induced Electron Localization Drives CO2 Reduction to C2 Hydrocarbons. *Nat. Chem.* **2018**, *10* (9), 974−980.
(181) Hahn, C.; Hatsukade, T.; Kim, Y.-G.; Vailionis, A.; Baricuatro, J. H.; Higgins, D. C.; Nitopi, S. A.; Soriaga, M. P.; Jaramillo, T. F. Engineering Cu Surfaces for the Electrocatalytic Conversion of CO2: Controlling Selectivity toward Oxygenates and Hydrocarbons. *Proc. Natl. Acad. Sci. U. S. A.* **2017**, *114* (23), 5918−5923.
(182) Bagger, A.; Ju, W.; Varela, A. S.; Strasser, P.; Rossmeisl, J. Electrochemical CO2 Reduction: A Classification Problem. *ChemPhysChem* **2017**, *18* (22), 3266−3273.
(183) Kortlever, R.; Shen, J.; Schouten, K. J. P.; Calle-vallejo, F.; Koper, M. T. M. Catalysts and Reaction Pathways for the Electrochemical Reduction of Carbon Dioxide. *J. Phys. Chem. Lett.* **2015**, *6*, 4073−4082.
(184) Lum, Y.; Ager, J. W. Stability of Residual Oxides in Oxide-Derived Copper Catalysts for Electrochemical CO2Reduction Investigated With18O Labeling. *Angew. Chem., Int. Ed.* **2018**, *57* (2), 551−554.
(185) Schreier, M.; Yoon, Y.; Jackson, M. N.; Surendranath, Y. Competition between H and CO for Active Sites Governs Copper-Mediated Electrosynthesis of Hydrocarbon Fuels. *Angew. Chem., Int. Ed.* **2018**, *57* (32), 10221−10225.
(186) Birdja, Y. Y.; Pérez-Gallent, E.; Figueiredo, M. C.; Göttle, A. J.; Calle-Vallejo, F.; Koper, M. T. M. Advances and Challenges in Understanding the Electrocatalytic Conversion of Carbon Dioxide to Fuels. *Nat. Energy* **2019**, *4* (9), 732−745.
(187) Peterson, A. A.; Nørskov, J. K. Activity Descriptors for CO 2 Electroreduction to Methane on Transition-Metal Catalysts. *J. Phys. Chem. Lett.* **2012**, *3* (2), 251−258.
(188) Shi, C.; Hansen, H. A.; Lausche, A. C.; Nørskov, J. K. Trends in Electrochemical CO2 Reduction Activity for Open and Close-Packed Metal Surfaces. *Phys. Chem. Chem. Phys.* **2014**, *16* (10), 4720−4727.
(189) Varley, J. B.; Hansen, H. A.; Ammitzbøll, N. L.; Grabow, L. C.; Peterson, A. A.; Rossmeisl, J.; Nørskov, J. K. Ni-Fe-S Cubanes in CO2 Reduction Electrocatalysis: A DFT Study. *ACS Catal.* **2013**, *3* (11), 2640−2643.
(190) Piontek, S.; Junge Puring, K.; Siegmund, D.; Smialkowski, M.; Sinev, I.; Tetzlaff, D.; Roldan Cuenya, B.; Apfel, U. P. Bio-Inspired Design: Bulk Iron-Nickel Sulfide Allows for Efficient Solvent-Dependent CO2 Reduction. *Chem. Sci.* **2019**, *10* (4), 1075−1081.
(191) Zhao, S.; Guo, S.; Zhu, C.; Gao, J.; Li, H.; Huang, H.; Liu, Y.; Kang, Z. Achieving Electroreduction of CO2 to CH3OH with High Selectivity Using a Pyrite-Nickel Sulfide Nanocomposite. *RSC Adv.* **2017**, *7* (3), 1376−1381.
(192) Shinagawa, T.; Larrazábal, G. O.; Martín, A. J.; Krumeich, F.; Pérez-Ramírez, J. Sulfur-Modified Copper Catalysts for the Electrochemical Reduction of Carbon Dioxide to Formate. *ACS Catal.* **2018**, *8* (2), 837−844.
(193) Yang, D.; Zhu, Q.; Chen, C.; Liu, H.; Liu, Z.; Zhao, Z.; Zhang, X.; Liu, S.; Han, B. Selective Electroreduction of Carbon Dioxide to Methanol on Copper Selenide Nanocatalysts. *Nat. Commun.* **2019**, *10* (1), 1−9.
(194) Deng, Y.; Huang, Y.; Ren, D.; Handoko, A. D.; Seh, Z. W.; Hirunsit, P.; Yeo, B. S. On the Role of Sulfur for the Selective Electrochemical Reduction of CO2 to Formate on CuSx Catalysts. *ACS Appl. Mater. Interfaces* **2018**, *10* (34), 28572−28581.
(195) Aljabour, A.; Coskun, H.; Zheng, X.; Kibria, M. G.; Strobel, M.; Hild, S.; Kehrer, M.; Stifter, D.; Sargent, E. H.; Stadler, P. Active Sulfur Sites in Semimetallic Titanium Disulfide Enable Co2 Electroreduction. *ACS Catal.* **2020**, *10* (1), 66−72.
(196) Ji, Y.; Nørskov, J. K.; Chan, K. Scaling Relations on Basal Plane Vacancies of Transition Metal Dichalcogenides for CO2 Reduction. *J. Phys. Chem. C* **2019**, *123* (7), 4256−4261.
(197) Rosen, B. A.; Haan, J. L.; Mukherjee, P.; Braunschweig, B.; Zhu, W.; Salehi-Khojin, A.; Dlott, D. D.; Masel, R. I. In Situ Spectroscopic Examination of a Low Overpotential Pathway for Carbon Dioxide Conversion to Carbon Monoxide. *J. Phys. Chem. C* **2012**, *116* (29), 15307−15312.
(198) Li, F.; Zhao, S. F.; Chen, L.; Khan, A.; MacFarlane, D. R.; Zhang, J. Polyethylenimine Promoted Electrocatalytic Reduction of CO2 to CO in Aqueous Medium by Graphene-Supported Amorphous Molybdenum Sulphide. *Energy Environ. Sci.* **2016**, *9* (1), 216−223.
(199) Asadi, M.; Motevaselian, M. H.; Moradzadeh, A.; Majidi, L.; Esmaeilirad, M.; Sun, T. V.; Liu, C.; Bose, R.; Abbasi, P.; Zapol, P.; Khodadoust, A. P.; Curtiss, L. A.; Aluru, N. R.; Salehi-Khojin, A. Highly Efficient Solar-Driven Carbon Dioxide Reduction on Molybdenum Disulfide Catalyst Using Choline Chloride-Based Electrolyte. *Adv. Energy Mater.* **2019**, *9* (9), 1803536.
(200) Landers, A. T.; Fields, M.; Torelli, D. A.; Xiao, J.; Hellstern, T. R.; Francis, S. A.; Tsai, C.; Kibsgaard, J.; Lewis, N. S.; Chan, K.; Hahn, C.; Jaramillo, T. F. The Predominance of Hydrogen Evolution on Transition Metal Sulfides and Phosphides under CO2 Reduction Conditions: An Experimental and Theoretical Study. *ACS Energy Lett.* **2018**, *3* (6), 1450−1457.
(201) Asadi, M.; Kumar, B.; Behranginia, A.; Rosen, B. a; Baskin, A.; Repnin, N.; Pisasale, D.; Phillips, P.; Zhu, W.; Haasch, R.; Klie, R. F.; Král, P.; Abiade, J.; Salehi-Khojin, A. Robust Carbon Dioxide Reduction on Molybdenum Disulphide Edges. *Nat. Commun.* **2014**, *5*, 4470.
(202) Xu, J.; Li, X.; Liu, W.; Sun, Y.; Ju, Z.; Yao, T.; Wang, C.; Ju, H.; Zhu, J.; Wei, S.; Xie, Y. Carbon Dioxide Electroreduction into Syngas Boosted by a Partially Delocalized Charge in Molybdenum Sulfide Selenide Alloy Monolayers. *Angew. Chem., Int. Ed.* **2017**, *56* (31), 9121−9125.
(203) Francis, S. A.; Velazquez, J. M.; Ferrer, I. M.; Torelli, D. A.; Guevarra, D.; McDowell, M. T.; Sun, K.; Zhou, X.; Saadi, F. H.; John, J.; Richter, M. H.; Hyler, F. P.; Papadantonakis, K. M.; Brunschwig, B.

S.; Lewis, N. S. Reduction of Aqueous CO 2 to 1-Propanol at MoS 2 Electrodes. *Chem. Mater.* **2018**, *30* (15), 4902−4908.
(204) Liu, C.; Liu, P. Mechanistic Study of Methanol Synthesis from CO2 and H2 on a Modified Model Mo6S8 Cluster. *ACS Catal.* **2015**, *5* (2), 1004−1012.
(205) Perryman, J. T.; Ortiz-Rodríguez, J. C.; Jude, J. W.; Hyler, F. P.; Davis, R. C.; Mehta, A.; Kulkarni, A. R.; Patridge, C. J.; Velázquez, J. M. Metal-Promoted Mo6S8 Clusters: A Platform for Probing Ensemble Effects on the Electrochemical Conversion of CO 2 and CO to Methanol. *Mater. Horiz.* **2020**, *7*, 193−202.
(206) Lv, K.; Teng, C.; Shi, M.; Yuan, Y.; Zhu, Y.; Wang, J.; Kong, Z.; Lu, X.; Zhu, Y. Hydrophobic and Electronic Properties of the E-MoS2 Nanosheets Induced by FAS for the CO2 Electroreduction to Syngas with a Wide Range of CO/H2 Ratios. *Adv. Funct. Mater.* **2018**, *28* (49), 1802339.
(207) Nielsen, A., Ed. *Ammonia: Catalysis and Manufacture*, 1st ed.; Springer-Verlag: Berlin, 1995; pp 1−346.
(208) Zhao, Y.; Setzler, B. P.; Wang, J.; Nash, J.; Wang, T.; Xu, B.; Yan, Y. An Efficient Direct Ammonia Fuel Cell for Affordable Carbon-Neutral Transportation. *Joule* **2019**, *3* (10), 2472−2484.
(209) Qian, J.; An, Q.; Fortunelli, A.; Nielsen, R. J.; Goddard, W. A. Reaction Mechanism and Kinetics for Ammonia Synthesis on the Fe(111) Surface. *J. Am. Chem. Soc.* **2018**, *140* (20), 6288−6297.
(210) Chen, J. G.; Crooks, R. M.; Seefeldt, L. C.; Bren, K. L.; Bullock, R. M.; Darensbourg, M. Y.; Holland, P. L.; Hoffman, B.; Janik, M. J.; Jones, A. K.; Kanatzidis, M. G.; King, P.; Lancaster, K. M.; Lymar, S. V.; Pfromm, P.; Schneider, W. F.; Schrock, R. R. Beyond Fossil Fuel−Driven Nitrogen Transformations. *Science (Washington, DC, U. S.)* **2018**, *360* (6391), eaar6611.
(211) Foster, S. L.; Bakovic, S. I. P.; Duda, R. D.; Maheshwari, S.; Milton, R. D.; Minteer, S. D.; Janik, M. J.; Renner, J. N.; Greenlee, L. F. Catalysts for Nitrogen Reduction to Ammonia. *Nat. Catal.* **2018**, *1* (7), 490−500.
(212) Greeley, J.; Jaramillo, T. F.; Bonde, J.; Chorkendorff, I.; Nørskov, J. K. Computational High-Throughput Screening of Electrocatalytic Materials for Hydrogen Evolution. *Nat. Mater.* **2006**, *5* (11), 909−913.
(213) Lazouski, N.; Schiffer, Z. J.; Williams, K.; Manthiram, K. Understanding Continuous Lithium-Mediated Electrochemical Nitrogen Reduction. *Joule* **2019**, *3* (4), 1127−1139.
(214) Lazouski, N.; Chung, M.; Williams, K.; Gala, M. L.; Manthiram, K. Non-Aqueous Gas Diffusion Electrodes for Rapid Ammonia Synthesis from Nitrogen and Water-Splitting-Derived Hydrogen. *Nat. Catal.* **2020**, *3* (5), 463−469.
(215) Andersen, S. Z.; Statt, M. J.; Bukas, V. J.; Shapel, S. G.; Pedersen, J. B.; Krempl, K.; Saccoccio, M.; Chakraborty, D.; Kibsgaard, J.; Vesborg, P. C. K.; Nørskov, J.; Chorkendorff, I. Increasing Stability, Efficiency, and Fundamental Understanding of Lithium-Mediated Electrochemical Nitrogen Reduction. *Energy Environ. Sci.* **2020**, *13* (11), 4291−4300.
(216) McEnaney, J. M.; Singh, A. R.; Schwalbe, J. A.; Kibsgaard, J.; Lin, J. C.; Cargnello, M.; Jaramillo, T. F.; Nørskov, J. K. Ammonia Synthesis from N2 and H2O Using a Lithium Cycling Electrification Strategy at Atmospheric Pressure. *Energy Environ. Sci.* **2017**, *10* (7), 1621−1630.
(217) Zhou, F.; Azofra, L. M.; Ali, M.; Kar, M.; Simonov, A. N.; McDonnell-Worth, C.; Sun, C.; Zhang, X.; Macfarlane, D. R. Electro-Synthesis of Ammonia from Nitrogen at Ambient Temperature and Pressure in Ionic Liquids. *Energy Environ. Sci.* **2017**, *10* (12), 2516−2520.
(218) Lee, H. K.; Koh, C. S. L.; Lee, Y. H.; Liu, C.; Phang, I. Y.; Han, X.; Tsung, C. K.; Ling, X. Y. Favoring the Unfavored: Selective Electrochemical Nitrogen Fixation Using a Reticular Chemistry Approach. *Sci. Adv.* **2018**, *4* (3), eaar3208.
(219) Zou, H.; Rong, W.; Wei, S.; Ji, Y.; Duan, L. Regulating Kinetics and Thermodynamics of Electrochemical Nitrogen Reduction with Metal Single-Atom Catalysts in a Pressurized Electrolyser. *Proc. Natl. Acad. Sci. U. S. A.* **2020**, *117* (47), 29462−29468.
(220) Liu, S.; Qian, T.; Wang, M.; Ji, H.; Shen, X.; Wang, C.; Yan, C. Proton-Filtering Covalent Organic Frameworks with Superior Nitrogen Penetration Flux Promote Ambient Ammonia Synthesis. *Nat. Catal.* **2021**, *4*, 322−331.
(221) Bao, D.; Zhang, Q.; Meng, F. L.; Zhong, H. X.; Shi, M. M.; Zhang, Y.; Yan, J. M.; Jiang, Q.; Zhang, X. B. Electrochemical Reduction of N2 under Ambient Conditions for Artificial N2 Fixation and Renewable Energy Storage Using N2/NH3 Cycle. *Adv. Mater.* **2017**, *29* (3), 1604799.
(222) Li, S. J.; Bao, D.; Shi, M. M.; Wulan, B. R.; Yan, J. M.; Jiang, Q. Amorphizing of Au Nanoparticles by CeOx−RGO Hybrid Support towards Highly Efficient Electrocatalyst for N2 Reduction under Ambient Conditions. *Adv. Mater.* **2017**, *29* (33), 1700001.
(223) Li, L.; Tang, C.; Xia, B.; Jin, H.; Zheng, Y.; Qiao, S. Z. Two-Dimensional Mosaic Bismuth Nanosheets for Highly Selective Ambient Electrocatalytic Nitrogen Reduction. *ACS Catal.* **2019**, *9* (4), 2902−2908.
(224) Choi, J.; Du, H.-L.; Nguyen, C. K.; Suryanto, B. H. R.; Simonov, A. N.; MacFarlane, D. R. Electroreduction of Nitrates, Nitrites, and Gaseous Nitrogen Oxides: A Potential Source of Ammonia in Dinitrogen Reduction Studies. *ACS Energy Lett.* **2020**, *5* (6), 2095−2097.
(225) Greenlee, L. F.; Renner, J. N.; Foster, S. L. The Use of Controls for Consistent and Accurate Measurements of Electrocatalytic Ammonia Synthesis from Dinitrogen. *ACS Catal.* **2018**, *8* (9), 7820−7827.
(226) Andersen, S. Z.; Čolić, V.; Yang, S.; Schwalbe, J. A.; Nielander, A. C.; McEnaney, J. M.; Enemark-Rasmussen, K.; Baker, J. G.; Singh, A. R.; Rohr, B. A.; Statt, M. J.; Blair, S. J.; Mezzavilla, S.; Kibsgaard, J.; Vesborg, P. C. K.; Cargnello, M.; Bent, S. F.; Jaramillo, T. F.; Stephens, I. E. L.; Nørskov, J. K.; Chorkendorff, I. A Rigorous Electrochemical Ammonia Synthesis Protocol with Quantitative Isotope Measurements. *Nature* **2019**, *570*, 504.
(227) MacFarlane, D. R.; Cherepanov, P. V.; Choi, J.; Suryanto, B. H. R.; Hodgetts, R. Y.; Bakker, J. M.; Ferrero Vallana, F. M.; Simonov, A. N. A Roadmap to the Ammonia Economy. *Joule* **2020**, *4* (6), 1186−1205.
(228) Kibsgaard, J.; Nørskov, J. K.; Chorkendorff, I. The Difficulty of Proving Electrochemical Ammonia Synthesis. *ACS Energy Lett.* **2019**, *4* (12), 2986−2988.
(229) Dabundo, R.; Lehmann, M. F.; Treibergs, L.; Tobias, C. R.; Altabet, M. A.; Moisander, P. H.; Granger, J. The Contamination of Commercial $^{15}N_2$ Gas Stocks With ^{15}N-Labeled Nitrate and Ammonium and Consequences for Nitrogen Fixation Measurements. *PLoS One* **2014**, *9* (10), e110335.
(230) Choi, J.; Suryanto, B. H. R.; Wang, D.; Du, H. L.; Hodgetts, R. Y.; Ferrero Vallana, F. M.; MacFarlane, D. R.; Simonov, A. N. Identification and Elimination of False Positives in Electrochemical Nitrogen Reduction Studies. *Nat. Commun.* **2020**, *11* (1), 1−10.
(231) Wang, H.-B.; Wang, J.-Q.; Zhang, R.; Cheng, C.-Q.; Qiu, K.-W.; Yang, Y.-j.; Mao, J.; Liu, H.; Du, M.; Dong, C.-K.; Du, X.-W. Bionic Design of a Mo(IV)-Doped FeS2 Catalyst for Electroreduction of Dinitrogen to Ammonia. *ACS Catal.* **2020**, *10* (9), 4914−4921.
(232) Su, H.; Chen, L.; Chen, Y.; Si, R.; Wu, Y.; Wu, X.; Geng, Z.; Zhang, W.; Zeng, J. Single Atoms of Iron on MoS2 Nanosheets for N2 Electroreduction into Ammonia. *Angew. Chem., Int. Ed.* **2020**, *59* (46), 20411−20416.
(233) Li, J.; Chen, S.; Quan, F.; Zhan, G.; Jia, F.; Ai, Z.; Zhang, L. Accelerated Dinitrogen Electroreduction to Ammonia via Interfacial Polarization Triggered by Single-Atom Protrusions. *Chem.* **2020**, *6* (4), 885−901.
(234) Wu, Z.; Zhang, R.; Fei, H.; Liu, R.; Wang, D.; Liu, X. Multiphasic 1T@2H MoSe2 as a Highly Efficient Catalyst for the N2 Reduction to NH3. *Appl. Surf. Sci.* **2020**, *532*, 147372.
(235) Yang, L.; Wang, H.; Wang, X.; Luo, W.; Wu, C.; Wang, C. A.; Xu, C. Flower-like Hollow MoSe2 Nanospheres as Efficient Earth-Abundant Electrocatalysts for Nitrogen Reduction Reaction under Ambient Conditions. *Inorg. Chem.* **2020**, *59* (17), 12941−12946.

https://doi.org/10.1021/acsmaterialsau.1c00006
ACS Mater. Au 2021, 1, 6−36

(236) Li, H.; Gu, S.; Sun, Z.; Guo, F.; Xie, Y.; Tao, B.; He, X.; Zhang, W.; Chang, H. The In-Built Bionic "MoFe Cofactor" in Fe-Doped Two-Dimensional MoTe2 Nanosheets for Boosting the Photocatalytic Nitrogen Reduction Performance. *J. Mater. Chem. A* **2020**, *8* (26), 13038−13048.
(237) Murakami, J.; Yamaguchi, W. Reduction of N 2 by Supported Tungsten Clusters Gives a Model of the Process by Nitrogenase. *Sci. Rep.* **2012**, *2*, 1−6.
(238) Hoffman, B. M.; Lukoyanov, D.; Yang, Z. Y.; Dean, D. R.; Seefeldt, L. C. Mechanism of Nitrogen Fixation by Nitrogenase: The next Stage. *Chem. Rev.* **2014**, *114* (8), 4041−4062.
(239) Zhang, L.; Ji, X.; Ren, X.; Ma, Y.; Shi, X.; Tian, Z.; Asiri, A. M.; Chen, L.; Tang, B.; Sun, X. Electrochemical Ammonia Synthesis via Nitrogen Reduction Reaction on a MoS2 Catalyst: Theoretical and Experimental Studies. *Adv. Mater.* **2018**, *30* (28), 1800191.
(240) Li, F.; Chen, L.; Liu, H.; Wang, D.; Shi, C.; Pan, H. Enhanced N2-Fixation by Engineering the Edges of Two-Dimensional Transition-Metal Disulfides. *J. Phys. Chem. C* **2019**, *123* (36), 22221−22227.
(241) Liu, C.; Li, Q.; Wu, C.; Zhang, J.; Jin, Y.; Macfarlane, D. R.; Sun, C. Single-Boron Catalysts for Nitrogen Reduction Reaction. *J. Am. Chem. Soc.* **2019**, *141* (7), 2884−2888.
(242) Zhang, J.; Tian, X.; Liu, M.; Guo, H.; Zhou, J.; Fang, Q.; Liu, Z.; Wu, Q.; Lou, J. Cobalt-Modulated Molybdenum−Dinitrogen Interaction in MoS2 for Catalyzing Ammonia Synthesis. *J. Am. Chem. Soc.* **2019**, *141* (49), 19269−19275.
(243) Li, X.; Ren, X.; Liu, X.; Zhao, J.; Sun, X.; Zhang, Y.; Kuang, X.; Yan, T.; Wei, Q.; Wu, D. A MoS 2 Nanosheet-Reduced Graphene Oxide Hybrid: An Efficient Electrocatalyst for Electrocatalytic N 2 Reduction to NH 3 under Ambient Conditions. *J. Mater. Chem. A* **2019**, *7* (6), 2524−2528.
(244) Tang, W.; Sanville, E.; Henkelman, G. A Grid-Based Bader Analysis Algorithm without Lattice Bias. *J. Phys.: Condens. Matter* **2009**, *21* (8), 084204.
(245) Liu, Y.; Han, M.; Xiong, Q.; Zhang, S.; Zhao, C.; Gong, W.; Wang, G.; Zhang, H.; Zhao, H. Dramatically Enhanced Ambient Ammonia Electrosynthesis Performance by In-Operando Created Li−S Interactions on MoS 2 Electrocatalyst. *Adv. Energy Mater.* **2019**, *9* (14), 1803935.
(246) Guo, M.; Yang, Y.; Leng, Y.; Wang, L.; Dong, H.; Liu, H.; Li, W. Edge Dominated Electronic Properties of MoS2/Graphene Hybrid 2D Materials: Edge State, Electron Coupling and Work Function. *J. Mater. Chem. C* **2017**, *5* (20), 4845−4851.
(247) Liu, Y.; Wang, W.; Zhang, S.; Li, W.; Wang, G.; Zhang, Y.; Han, M.; Zhang, H. MoS2 Nanodots Anchored on Reduced Graphene Oxide for Efficient N2 Fixation to NH3. *ACS Sustainable Chem. Eng.* **2020**, *8*, 2320.
(248) Zeng, L.; Chen, S.; Van Der Zalm, J.; Li, X.; Chen, A. Sulfur Vacancy-Rich N-Doped MoS2 Nanoflowers for Highly Boosting Electrocatalytic N2 Fixation to NH3 under Ambient Conditions. *Chem. Commun.* **2019**, *55* (51), 7386−7389.
(249) Hong, J.; Hu, Z.; Probert, M.; Li, K.; Lv, D.; Yang, X.; Gu, L.; Mao, N.; Feng, Q.; Xie, L.; Zhang, J.; Wu, D.; Zhang, Z.; Jin, C.; Ji, W.; Zhang, X.; Yuan, J.; Zhang, Z. Exploring Atomic Defects in Molybdenum Disulphide Monolayers. *Nat. Commun.* **2015**, *6*, 1−8.
(250) Matanovic, I.; Leung, K.; Percival, S. J.; Park, J. E.; Lu, P.; Atanassov, P.; Chou, S. S. Towards Defect Engineering in Hexagonal MoS2 Nanosheets for Tuning Hydrogen Evolution and Nitrogen Reduction Reactions. *Appl. Mater. Today* **2020**, *21*, 100812.
(251) Guo, H.; Li, L.; Wang, X.; Yao, G.; Yu, H.; Tian, Z.; Li, B.; Chen, L. Theoretical Investigation on the Single Transition-Metal Atom-Decorated Defective MoS2 for Electrocatalytic Ammonia Synthesis. *ACS Appl. Mater. Interfaces* **2019**, *11* (40), 36506−36514.
(252) Ma, X.; Hu, J.; Zheng, M.; Li, D.; Lv, H.; He, H.; Huang, C. N2 Reduction Using Single Transition-Metal Atom Supported on Defective WS2Monolayer as Promising Catalysts: A DFT Study. *Appl. Surf. Sci.* **2019**, *489* (April), 684−692.
(253) Zhao, J.; Zhao, J.; Cai, Q. Single Transition Metal Atom Embedded into a MoS2 Nanosheet as a Promising Catalyst for Electrochemical Ammonia Synthesis. *Phys. Chem. Chem. Phys.* **2018**, *20* (14), 9248−9255.
(254) Du, H.-L.; Hodgetts, R. Y.; Chatti, M.; Nguyen, C. K.; Macfarlane, D. R.; Simonov, A. N. Is Molybdenum Disulfide Modified with Molybdenum Metal Catalytically Active for the Nitrogen Reduction Reaction? *J. Electrochem. Soc.* **2020**, *167* (14), 146507.
(255) Azofra, L. M.; Sun, C.; Cavallo, L.; MacFarlane, D. R. Feasibility of N2 Binding and Reduction to Ammonia on Fe-Deposited MoS2 2D Sheets: A DFT Study. *Chem. - Eur. J.* **2017**, *23* (34), 8275−8279.
(256) Zhao, X.; Zhang, X.; Xue, Z.; Chen, W.; Zhou, Z.; Mu, T. Fe Nanodot-Decorated MoS2 Nanosheets on Carbon Cloth: An Efficient and Flexible Electrode for Ambient Ammonia Synthesis. *J. Mater. Chem. A* **2019**, *7* (48), 27417−27422.
(257) Fu, Y.; Li, T.; Zhou, G.; Guo, J.; Ao, Y.; Hu, Y.; Shen, J.; Liu, L.; Wu, X. Dual-Metal-Driven Selective Pathway of Nitrogen Reduction in Orderly Atomic-Hybridized Re2MnS6 Ultrathin Nanosheets. *Nano Lett.* **2020**, *20* (7), 4960−4967.
(258) Yang, C.; Huang, B.; Bai, S.; Feng, Y.; Shao, Q.; Huang, X. A Generalized Surface Chalcogenation Strategy for Boosting the Electrochemical N2 Fixation of Metal Nanocrystals. *Adv. Mater.* **2020**, *32* (24), 2001267.
(259) Kim, H. S.; Choi, J.; Kong, J.; Kim, H.; Yoo, S. J.; Park, H. S. Regenerative Electrocatalytic Redox Cycle of Copper Sulfide for Sustainable NH3 Production under Ambient Conditions. *ACS Catal.* **2021**, *11* (1), 435−445.
(260) Fan, X. L.; Yang, Y.; Xiao, P.; Lau, W. M. Site-Specific Catalytic Activity in Exfoliated MoS2 Single-Layer Polytypes for Hydrogen Evolution: Basal Plane and Edges. *J. Mater. Chem. A* **2014**, *2* (48), 20545−20551.
(261) Shi, G.; Yu, L.; Ba, X.; Zhang, X.; Zhou, J.; Yu, Y. Copper Nanoparticle Interspersed MoS2 Nanoflowers with Enhanced Efficiency for CO2 Electrochemical Reduction to Fuel. *Dalt. Trans.* **2017**, *46* (32), 10569−10577.
(262) Liu, S.; Tao, H.; Zeng, L.; Liu, Q.; Xu, Z.; Liu, Q.; Luo, J. L. Shape-Dependent Electrocatalytic Reduction of CO2 to CO on Triangular Silver Nanoplates. *J. Am. Chem. Soc.* **2017**, *139* (6), 2160−2163.

https://doi.org/10.1021/acsmaterialsau.1c00006
ACS Mater. Au 2021, 1, 6−36